ION CAPTURE IN HELIUM DROPLETS: FORMATION OF COLD ION-NEUTRAL CLUSTERS

Travis M. Falconer

A dissertation submitted to the faculty of the University of North Carolina at Chapel Hill in partial fulfillment of the requirements for the degree of Doctor of Philosophy in the Department of Chemistry.

Chapel Hill
2008

Approved by:

Gary L. Glish

Royce W. Murray

Mark H. Schoenfisch

Christopher J. Fecko

Jeffrey S. Johnson

ABSTRACT

TRAVIS M. FALCONER: Ion Capture in Helium Droplets: Formation of Cold Ion-Neutral Clusters
(Under the direction of Roger E. Miller and Gary L. Glish)

Superfluid helium nanodroplets are used to cool ions and form ion-neutral clusters at a temperature of 0.37 K. A desolvation technique was developed that allowed for the study of captured ions by mass spectrometry. From the mass spectrometry results it was determined that helium droplets may successfully capture sodium cations with kinetic energy of ~200 eV. Clusters of the neutral molecules H_2O, N_2, and HCN with Na^+ were observed. Based on binding strength considerations, it is argued that the desolvation process imparts little energy into the ion-neutral clusters, avoiding dissociation. This result leads to the conclusion that ion-neutral clusters are formed within the droplet prior to desolvation, indicating that the helium "snowball" that is assumed to form around Na^+ does not prevent ion-neutral cluster formation. This conclusion is supported by ab initio calculations, the results of which indicate the presence of barrierless pathways for neutral molecule insertion into the helium snowball surrounding Na^+.

The process of ion capture by helium droplets was studied by comparison of measured ion-doped droplet size distributions to known pre-ion capture droplet size distributions. The measured ion-doped droplet size distributions were affected by nozzle temperature, ion kinetic energy, and ion mass. These factors primarily affect two

parameters of the ion-doped droplet size distribution, the minimum droplet size threshold, N_{thr}, and the droplet size at maximum signal intensity, N_{max}. The effects of the studied factors on the measured distributions cannot be explained in terms of currently accepted droplet cooling mechanisms.

Analysis of the results suggests that droplet doping efficiency can be improved in several ways, including a higher flux of lower-energy ions. An apparatus for the production and focusing of alkali cations at high fluxes and low energies is described. This apparatus was able to produce higher ion currents at lower kinetic energies than previous ion sources.

ACKNOWLEDGEMENTS

There are many people that deserve my thanks for helping me reach this point. First is my original advisor here at UNC, the late Professor Roger E. Miller. Although his time as my advisor was cut short, I still carry with me the lessons that I learned from him and refer to them frequently. I am deeply saddened and profoundly honored to be the last student to participate in his innovative helium droplet research.

Of course, I would not have reached this point without the intervention of Professor Gary L. Glish, who invited me to join his group after Professor Miller's passing. Professor Glish's willingness to take on the task of advising a student whose work was only tangential to his own and to accommodate the hulking instrumentation that accompanied it was beyond generous. From this arrangement I was not only able to complete my degree at UNC, but I also gained a mentor and friend.

The work discussed in this dissertation was additionally guided by Dr. Raymond J. Bemish. Ray has made substantial contributions to this work, including the interpretation of results and editing of papers. He has helped me grow as a scientist while treating me as an equal. His support during tumultuous times is greatly appreciated.

My time at UNC was enriched by the people with whom I worked. Regarding my colleagues in the Miller lab, I am certain that I could not have joined a better group, either scientifically or personally. Specifically, I would like to thank Drs. Myong-Yong Choi, Gary Douberly, C. Michael Lindsay, William Lewis, Jeremy Merritt, and Paul

Stiles. In particular, much of the work in this dissertation was performed in cooperation with Will, whose contributions have been invaluable. The writing of this dissertation has also greatly benefited from many conversations with Gary.

My transition from the Miller lab to the Glish lab was very positive thanks to the students in the group. My gratitude is extended to Dr. Philip Remes, Karen Wendling, Jared Bushey, Brittany Butler, Mark Ridgeway, and Asher Newsome. Special thanks go to Alessandra Ferzoco, who also migrated to the Glish lab from the Miller lab and has sacrificed considerable free time to help me refine the contents of this dissertation.

Much of the work discussed here involved custom hardware that was fabricated by the gifted hands of Don Brewer, James Perotti, and Freddy Pinero in the departmental instrument shop. The move from Kenan Labs to Caudill Labs would not have been a success without the help of Bruce Clifton, the only electrician willing to tackle the task of installing all of the necessary hardware to get the helium droplet instrument running.

Life in Chapel Hill was made very enjoyable by the many wonderful friends I had during my graduate career, all of whom helped shape who I am today. Particular thanks go to “Dobs,” Frank, Cory, Justin, Andy, Ben, Matt, and Pete.

I would also like to acknowledge the support of my family. Thanks to my parents, Mac and Rita, and my siblings, Sean and Trisha, who have always made me feel more intelligent than I really am and encouraged me to pursue the most difficult challenges. And many thanks to my fiancée, Stephanie Urbin, whose warm smile has never faded while patiently tolerating many late nights in lab.

This work was supported by funding from Pfizer, Inc.

TABLE OF CONTENTS

LIST OF TABLES

TABLE

LIST OF FIGURES

FIGURE

LIST OF ABBREVIATIONS AND SYMBOLS

a	slope
a_0	speed of sound
a.u.	arbitrary units
A	slope
A	vapor pressure constant
Å	angstroms
B	y-intercept
β	expected number of molecules encountered by helium droplet
cm	centimeters
cm^{-1}	wavenumbers
C	Celsius
d_0	nozzle aperture diameter
dc	direct current
D	Debye
Da	Daltons
eV	electron volts
exp	exponential function
EI	electron ionization
F	flux of helium droplets
FWHM	full-width at half the maximum
g_+	statistical weight of ionic states
g_0	statistical weight of neutral states

h	Planck constant, 6.626×10^{-34} J s
IR	infrared
IRMPD	infrared multiphoton photodissociation
J	Joules
k	Boltzmann constant, 1.381×10^{-23} J/K
k	number of molecules picked-up by helium droplet
kcal	kilocalories
keV	kilo-electron volts
K	Kelvin
K_1	kinetic parameter in Regime I droplet size scaling law
K_2	thermodynamic parameter in Regime I droplet size scaling law
l	angular momentum quantum number
L	length
L	liters
ln	natural logarithm
m	mass of helium atom
m	angular momentum quantum number
m	number of HCN molecules in ion-neutral cluster
m	meters
meV	milli-electron volts
mm	millimeters
mol	moles
mV	millivolts

m/z	ratio of mass to charge
n	number of H_2O molecules in ion-neutral cluster
n_0	number density of helium atoms
n_r	number of radial nodes
nA	nanoamps
η	number density
N	droplet size in helium atoms
$\overline{N}$	mean droplet size
N_{max}	ion-doped droplet size of maximum abundance in size distribution
N_{min}	minimum ion-doped droplet size able to reach mass spectrometer
N_{thr}	minimum ion-doped droplet size
$\Delta N_{1/2}$	half-width of the distribution of $P_N(N)$
o.d.	outer diameter
OPO	optical parametric oscillator
p_0	stagnation pressure
p_{H2O}	pressure of water vapor
ρ	density
Pa	Pascals
$P(k,N)$	probability of capturing k molecules in a droplet of size N
$P_N(N)$	probability of producing a droplet of size N
$P_{occ}(k,N)$	probability a droplet of size N is produced and captures k molecules
q	empirically determined parameter in Regime I droplet size scaling law
r	droplet radius

R^2	quality of fit parameter, $0<R^2\leq 1$
s	seconds
S	standard deviation of the distribution of $P_N(N)$
T	temperature
T_0	nozzle temperature
T_c	critical temperature of ^{4}He
T_{ref}	reference temperature
TPM	triphenylmethanol
μ	mean of the distribution of ln N
μm	micrometers
v	volume per helium atom
v	velocity
ν	frequency
V	volume
V	volts
V_{cyl}	volume of cylinder traversed by heliulm droplet
ω_m	energy of discrete droplet excitation
W	watts
γ	surface tension
Γ	dimensionless parameter involved in determination of $\overline{N}$
λ-line	border of superfluid region in ^{4}He phase diagram
π	3.14159265359
π	pi electrons

σ	standard deviation of the distribution of ln N
σ	cross-sectional area
φ	work function
Φ	ionization potential
ψ_+	rate of cation emission
ψ_0	rate of neutral emission
2-D	two-dimensional
°	degrees

CHAPTER 1

INTRODUCTION

1.1 Influence of Ions

Ions play a crucial role in many processes, from the largest to smallest scales. They are central to the chemistry that occurs in interstellar space, the atmospheres of planets, and throughout biology. For example, in interstellar space, ions exert control over the formation of stars.[1] Ions are also present in the atmosphere of the planets and moons of the solar system. These highly reactive ions can produce or destroy neutral molecules to affect the composition of the atmosphere of a planet.[2] In Earth's lower atmosphere the number density of ions, $\sim 10^3/cm^3$, is much lower than that of neutral molecules, $\sim 10^{19}/cm^3$, but the role of ions in atmospheric chemistry is important due to the enhanced rates at which many ion-promoted reactions proceed relative to neutral-neutral reactions.[2] Similarly, ions are important in biology and medicine due to the physiological roles that they play, such as maintaining osmotic equilibrium and exciting nerves and muscles. Many of the biological functions of ions are determined by competitive solvation processes. Due to the importance of these processes, they have been thoroughly investigated and constitute an area of expanding interest in ion chemistry.

1.2 Ion Solvation

Although ion solvation has been studied extensively, it continues to receive attention as the methods for studying such processes improve and the importance of these fundamental interactions is realized. Systems as simple as the solvated proton are the focus of intense research.[3,4] Of course, H^+ is not the only ion of interest. Alkali cations have been the subject of many solvation studies. The closed-shell nature of alkali cations restrains the reactants to the ground electronic state.[5] Thus, the primary interaction between the ion and the solvent is electrostatic, which allows for detailed examination of the relationship between ion-solvent and solvent-solvent interactions. Such studies have revealed size-dependent solvation characteristics. For example, the relationship between cation-π interactions and hydrogen-bonding of the solvent has been studied by binding of Na^+ and K^+.[6,7] In this elegant work, it was found that water molecules bound to K^+ could be displaced by benzene molecules, whereas water molecules bound to Na^+ could not. These findings have led to the proposal of molecular recognition methods based on size-dependent ion binding.

Size-dependent ion recognition based on cation-π binding is thought to be the means by which some selective ion channels operate.[8] In such a channel, H_2O molecules bound to K^+ would be displaced by the interaction of the ion with the π electrons of the aromatic side chain of a pore protein residue and the K^+ could pass through the channel. H_2O molecules bound to Na^+ would not be displaced and in this way the channel would not allow passage of the smaller Na^+.

1.3 Gas Phase Ion Structure

The importance of ions in biological systems stems from the ability of a bound ion to alter the structure of a molecule, which, in turn, can alter the reactivity of that molecule.[9,10] The binding of ions has been established as equally important as other noncovalent forces, such as hydrogen bonds and salt bridges, in determining the structure of peptides and proteins.[9,10] It has been found that protein geometry is stabilized by interactions of cations with the aromatic side chains of particular amino acids.[9,11] Detailed evaluation of these interactions is difficult. To access the specific interaction in question, the large, complicated problem must be broken down into its constituent parts. To study cation-π interactions, the binding of a cation to a single amino acid is analyzed. This is simlar to the approach taken to study ion solvation, in which the binding of an ion to a single solvent molecule is analyzed. Studying clusters with additional solvent molecules allows the examination of the relationship between ion-solvent and solvent-solvent interactions. The desire to isolate ion-molecule clusters makes the use of gas phase techniques the preferred approach.

The ability to isolate the ion cluster of interest based on the mass-to-charge ratio has made mass spectrometry a popular method for studying such species. High-pressure mass spectrometry was used to determine the enthalpy and entropy of solvation of alkali cations as a function of the number of solvent molecules.[12,13] Advances in mass spectrometric instrumentation led to the development of many techniques for studying the chemistry of ions, such as collision-induced dissociation, photoelectron-photonion coincidence, and others.[14] However, the nature of the information provided from these methods is primarily thermodynamic. The role of ions in molecular recognition

processes, particularly in biological systems, has resulted in the need to push beyond thermodynamic studies into structural determination. Although very useful in determining the sequence of large peptides and proteins, mass spectrometers alone are limited in their ability to provide detailed structural information of small molecules, such as differences between stereoisomers. Information of this variety can be obtained using infrared (IR) spectroscopy.[5]

Infrared spectroscopy of ions is inherently more difficult than that of neutral molecules. An IR spectrum of a neutral molecule is typically obtained by measuring the difference in intensity between radiation from a light source and radiation passed through a sample. A decrease in intensity of radiation passed through the sample is indicative of absorption. Observation of decreased optical intensity requires a large number of absorbing molecules. Unfortunately, the electric charge of ions results in Coulombic repulsion, which places an upper limit on ion density of ~$10^6/cm^3$.[15] Over the pathlength of typical mass spectrometers, this number density is a factor of $10^4/cm^3$ lower than the minimum necessary for detection of direct absorption. Therefore, a highly discriminating detection scheme is necessary for the IR spectroscopy of ions. A scheme often employed is action spectroscopy, in which the absorption of photon(s) by a gas phase ion results in an observable change, such as the change in mass that accompanies dissociation.

1.4 Multiphoton Techniques

The most common form of action spectroscopy used to study ions is infrared multiphoton photodissociation (IRMPD). In IRMPD, the absorption of infrared photons causes dissociation of the ion. Plotting the wavelength-dependent decrease of parent ion

abundance, or increase of product ion abundance, results in an IR spectrum. This form of spectroscopy has been used with success, but there are still significant challenges associated with the spectroscopy of ions, many of which are due to the absorption of multiple photons. Although many van der Waals complexes are bound weakly enough to require absorption of only a single photon to effect dissociation, many require the absorption of multiple photons. Such systems include alkali-cationized biomolecules[16-18] and tightly bound ion-solvent systems.[5]

The absorption of multiple photons by a limited density of ions requires tunable IR sources with extremely high fluences.[19] A high fluence of tunable IR radiation is achievable at dedicated facilities such as the free electron laser for infrared experiments at the FOM-Institute for Plasma Physics Rijnhuizen[20] or through the use of two lasers. In a two-laser experiment, one laser is a tunable IR laser with low fluence and the other is a non-tunable laser with high fluence. The frequency of the low-power laser is scanned and if a photon is absorbed the high-power laser can cause dissociation of the vibrationally-excited ion.[21] Advances in optical parametric oscillator (OPO) technology have recently allowed for the implementation of single lasers, although this has largely been limited to pulsed OPOs.[22]

The IR spectra that result from the absorption of multiple photons may be difficult to interpret, as they can vary significantly from theoretical predictions. The ab initio calculations used to assign vibrational bands yield linear absorption spectra whereas the absorption of multiple photons resulting in dissociation is not linear, making the comparison of predicted and experimental intensities difficult.[4,15] Furthermore, absorption at different wavelengths leads to differing internal energy population

distributions; as the internal energy increases so does the extent of red-shifting of the absorption frequency. These differences in internal energies mean that dissociation pathways with higher dissociation thresholds are red-shifted to a greater extent, further complicating spectral interpretation.

The internal energy of the ions being studied is not only important for comparison to theory, but also for the resolution of the IR spectrum obtained. High internal energies, or temperatures, lead to the population of multiple isomers, which in turn lead to broad and featureless bands.[23] This effect is particularly important for the *in-vacuo* formation of ion-neutral clusters, in which the nascent cluster ion has considerable internal energy that is dissipated by the evaporation of solvent molecules. In such an evaporative ensemble the internal energy decreases as a function of time.[5] The amount of internal energy also varies with size of the cluster. An example of this is the $M^+(H_2O)_n$ system, where M^+ is an alkali metal cation. The large binding energies of H_2O to alkali cations lead to effective temperatures of 700-1000 K for $M^+(H_2O)$.[23] Larger clusters, $M^+(H_2O)_n$, have effective temperatures from ~500 K for $n = 2$ to ~280 K for $n \geq 6$. It was observed that spectral linewidth decreases with increasing cluster size, or decreasing temperature.[5]

1.5 Messenger Techniques

A specific type of action spectroscopy, referred to as messenger molecule, or messenger atom, spectroscopy has served to overcome some of the difficulties associated with multiple photon dissociation and high-temperature ions. In this method, a weakly interacting messenger species is bound to the cluster ion. Due to the inherent nature of the evaporative ensemble, the internal energy of the cluster ion depends on the

composition of the cluster.[23] Thus, a weakly interacting messenger species leads to lower ion temperatures. Additionally, the low binding strength of the messenger to the cluster ion permits the absorption of a single photon to cause the messenger species to dissociate, which is readily observable:

$$[A^+ \cdot B] \cdot Z + h\nu \rightarrow [A^+ \cdot B] + Z, \qquad (1.1)$$

where $[A^+ \cdot B]$ represents a cluster ion and Z represents the messenger. The messenger molecule initially used in this method was H_2.[24] However, it was realized that the binding energy of argon atoms to most ions is less than 5 kcal/mol, which permits evaporative cooling to even lower temperatures and minimally perturbs the structure of the ion being studied.[23,25,26] The method of attaching argon atoms to ion clusters is referred to as either argon-tagging or rare gas nanomatrix spectroscopy. The cooling capabilities of the argon-tagging technique have been demonstrated with alkali cation-water clusters. As stated above, the temperatures of $M^+(H_2O)$ clusters formed *in-vacuo* were observed to be >700 K. However, the temperatures of $Na^+(H_2O)Ar$ and $K^+(H_2O)Ar$ were observed to be only 175 K and 130 K, respectively. An experimental arrangement in which argon-tagging occurs by collisional cooling instead of evaporative cooling routinely results in ion cluster temperatures of about 30 K.[27] The argon-tagging technique has been used to gain an improved understanding of many ionic systems, including the solvation of a proton[3,4] and differentiation of carbocation isomers.[28]

1.6 Ions in Helium Droplets

Although the temperatures achieved by cooling with argon atoms are substantially lower than those of the nascent ions, lower temperatures are desirable. Recently, superfluid helium nanodroplets have been shown to be very effective vessels for cooling

embedded species.[29-31] Helium droplets exhibit many desirable properties: they are a very weakly interacting medium in which molecules rotate freely and they have an internal temperature of only 0.37 K. This temperature is nearly a factor of 10^2 lower than the lowest temperatures achievable by argon-tagging.[27] Such a decrease in temperature of ions would result in improved IR spectroscopy. Indeed, it has been demonstrated that IR spectroscopy of neutral molecules in helium droplets results in sharper peaks than the corresponding spectra obtained in either Ar or H_2 clusters.[32-34] Therefore, the goal of this work was to embed ions in superfluid helium nanodroplets and form ion-neutral clusters cooled to 0.37 K.

A description of helium droplets, their relevant properties, and previous application to the study of ions will be discussed in Chapter 2. In Chapter 3, the apparatus and experimental considerations for the production of droplets and ions to be doped into the droplets are discussed. The capture of sodium cations and formation of Na^+-neutral clusters in helium droplets is demonstrated in Chapter 4. The process of alkali cation capture by helium droplets is examined in Chapter 5. The design of an alternative alkali cation source is described in Chapter 6. Finally, the outlook for research in this field is discussed in Chapter 7.

CHAPTER 2

SUPERFLUID HELIUM NANODROPLETS FOR THE COOLING OF IONS

2.1 Properties of Helium Droplets

Helium[1] is a unique element in that it is the only substance, at ambient pressure, expected to remain liquid at absolute zero. This phenomenon, which is shown graphically in the phase diagram of helium (Fig. 2.1), is due to the high zero point energy and weakly interacting nature of helium.[35] These properties lead to the existence of He-II, a superfluid that forms when the temperature is decreased below the λ-line. The term superfluid describes any fluid that flows without viscosity.[36] Similarly, and more relevant to the work discussed here, objects are able to move through a superfluid without friction, up to a velocity referred to as the Landau critical velocity.

The low temperatures and superfluid nature of He-II make it an appealing spectroscopic matrix. Although superfluid, helium droplets are not the same as bulk liquid He-II. The droplets have an internal temperature of 0.37 K, which was predicted by theory[37] and later confirmed by spectra of SF_6 embedded in droplets.[38,39] Unfortunately, other thermodynamic quantities, which have been measured for the

[1] The discussion of helium throughout this dissertation pertains specifically to ^{4}He; no consideration will be given to ^{3}He.

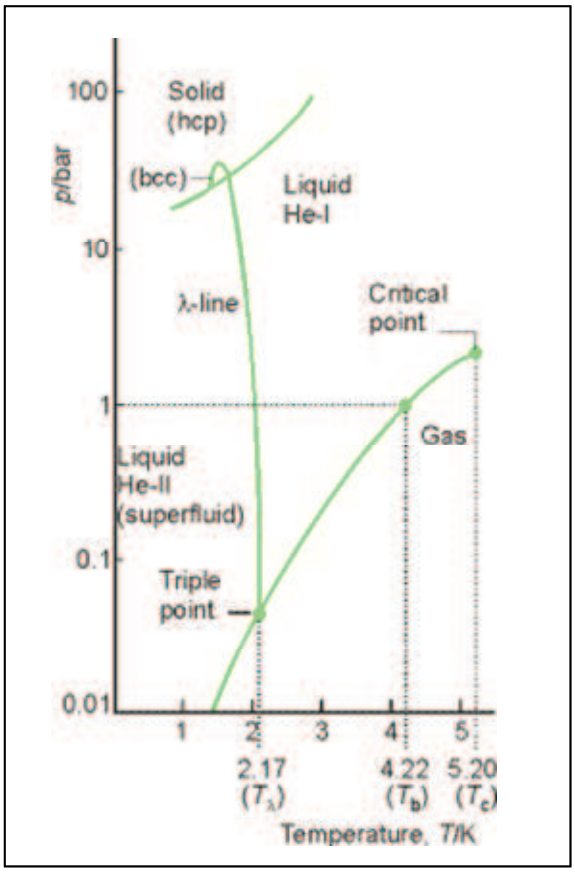

Figure 2.1 Phase diagram of ^{4}He. Taken from ref. [35].

bulk superfluid, are not well-defined for droplets.[40] Bulk superfluid helium exhibits a continuum of excitations, which are assigned to phonon and roton excitations.[41] However, droplets have a finite radius, which results in discrete collective modes corresponding to "bulk" and surface oscillations,[42] where the quotations indicate modes that are analogous to those of the bulk superfluid. The lowest-energy discrete "bulk" excitation was calculated to be $\omega_m = 26N^{-1/3}$ K, where N is the droplet size in number of helium atoms.[37] This equation yields a value of ~1.5 K for a droplet of 5000 He atoms. Thus, for a droplet with $N = 5000$, there are no thermally populated "bulk" excitations at the temperature of the droplet. For such excitations to be thermally

populated, the droplet size must be ~3.47 × 10^5 He atoms. This value is noteworthy because droplets of this size are utilized in the work presented. However, the contributions of such "bulk" excitations to the results discussed are not known.

The discrete states of finite size droplets are classified according to the number of radial nodes, n_r, and the angular momentum quanta, l and m, for a spherical system.[42] For the case of $n_r = 1$ and $l = m = 0$, a compressional oscillation occurs. As the radius of the droplet increases these states resemble the phonon and roton branches of the bulk liquid excitation spectrum and propagate radially to the surface of the droplet and are reflected. When $n_r = 0$ and $l \geq 2$, the oscillations created are surface excitations. At large droplet radii, the surface excitations resemble the ripplons observed at the bulk liquid-vapor interface. These surface modes are populated at the temperature of the droplet and are responsible for the rapid cooling of embedded molecules.[37] It should be noted that, despite being cooled by surface excitations, dopant molecules are located near the center of the droplet due to a favorable potential,[43] which is attributed to the decrease in free energy for a molecule solvated by the helium droplet versus remaining isolated in vacuum. The coupling of rotational and vibrational degrees of freedom of a molecule to the modes of the droplet results in very efficient cooling via the evaporation of helium atoms from the surface of the droplet.[2] The rate of evaporation is calculated to be ~10^9 He atoms/s, with each atom removing ~5 cm^{-1} of energy.[37] This rate of evaporation results in a rapid cooling rate, nearly 10^{10} K/s.

The weak interactions of helium are also responsible for the ability to tailor cluster formation within a droplet. Interactions of dopant molecules with each other are

[2] Cooling of dopants by the evaporation of helium atoms from the surface of the droplet will be referred to as the thermal cooling mechanism in subsequent sections.

stronger than they are with the surrounding helium atoms. Thus, when multiple molecules are doped into a droplet, a cluster of dopant molecules is formed. The combination of tailored cluster formation, extremely rapid cooling rate, and low temperature has enabled the formation and study of many interesting species using the helium droplet technique. These properties allow for the "freezing-out" of molecules and clusters into the first minimum sampled on the potential energy surface (Fig. 2.2). An example of this phenomenon can be found in the formation of water clusters in helium droplets, for which the cyclic structure of $(H_2O)_6$ was observed despite the fact that it is not the lowest-energy arrangement of six water molecules.[44]

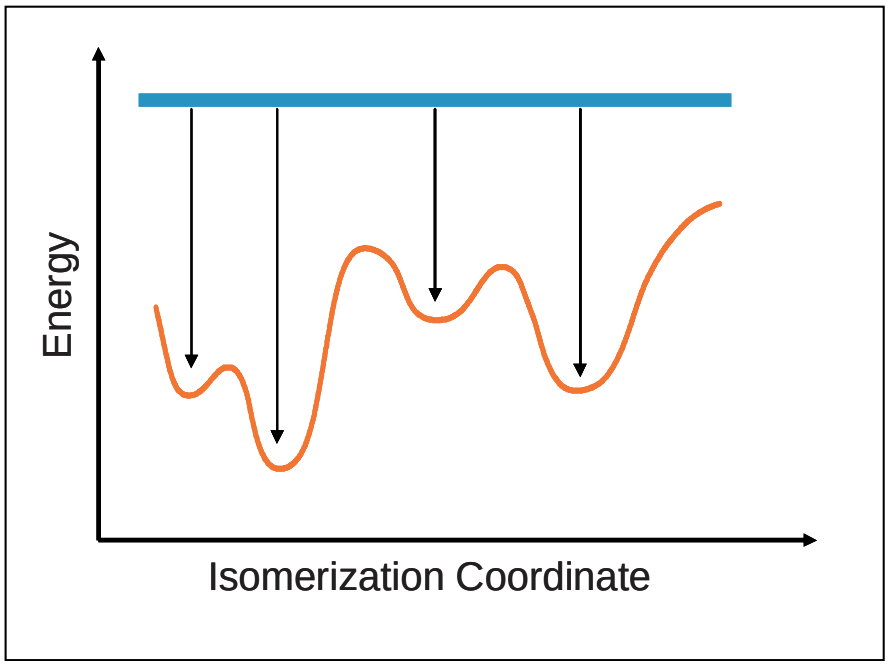

Figure 2.2 Potential energy surface of a molecule (red). Rapid cooling of molecules from thermal energy (blue bar) to 0.37 K results in sampling of local minima structures.

2.2 Ions in Helium Droplets

2.2.1 Ionization in Helium Droplets

As described in Section 1.6, helium droplets are being used to cool ions and form cold ion-neutral clusters. Initial efforts to study ions in helium droplets involved the ionization of pure droplets. Electron ionization (EI) or photoionization of a helium droplet results in the formation of He^+. The charge can resonantly transfer to neighboring atoms in a process referred to as charge-hopping.[45] Each hop occurs on the femtosecond time scale.[46] In a pure droplet, after several hops, the exothermic formation of He_N^+ occurs.[47] The amount of energy released in forming these ion clusters, 2.35 eV for He_2^+, for example, results in desolvation of the ion from the droplet. In the corresponding mass spectrum, ion cluster abundance decreases exponentially with increasing *N*, as shown in Figure 2.3. It should be noted that, for droplets of more than 10^5 He atoms, the positive charge can remain solvated by the droplet.[48]

The peak at *m/z* 28 in the spectrum in Figure 2.3 is indicated as having intensity contributed by $N_2^{+\cdot}$. It is interesting to consider whether $N_2^{+\cdot}$ arises from ionization of ambient N_2 or from N_2 picked-up by a helium droplet. The answer depends on the detection scheme implemented, as discussed in Chapter 3. However, it was discovered that the charge-hopping process that ends in the formation of He_N^+ in pure droplets can also result in the ionization of dopant molecules.[49] This process of charge-transfer ionization is possible due to the difference in ionization potentials between helium and the dopant species. Helium has the highest ionization potential of any substance, 24.6 eV.[50] Most atoms and molecules have ionization potentials less than 13 eV, making

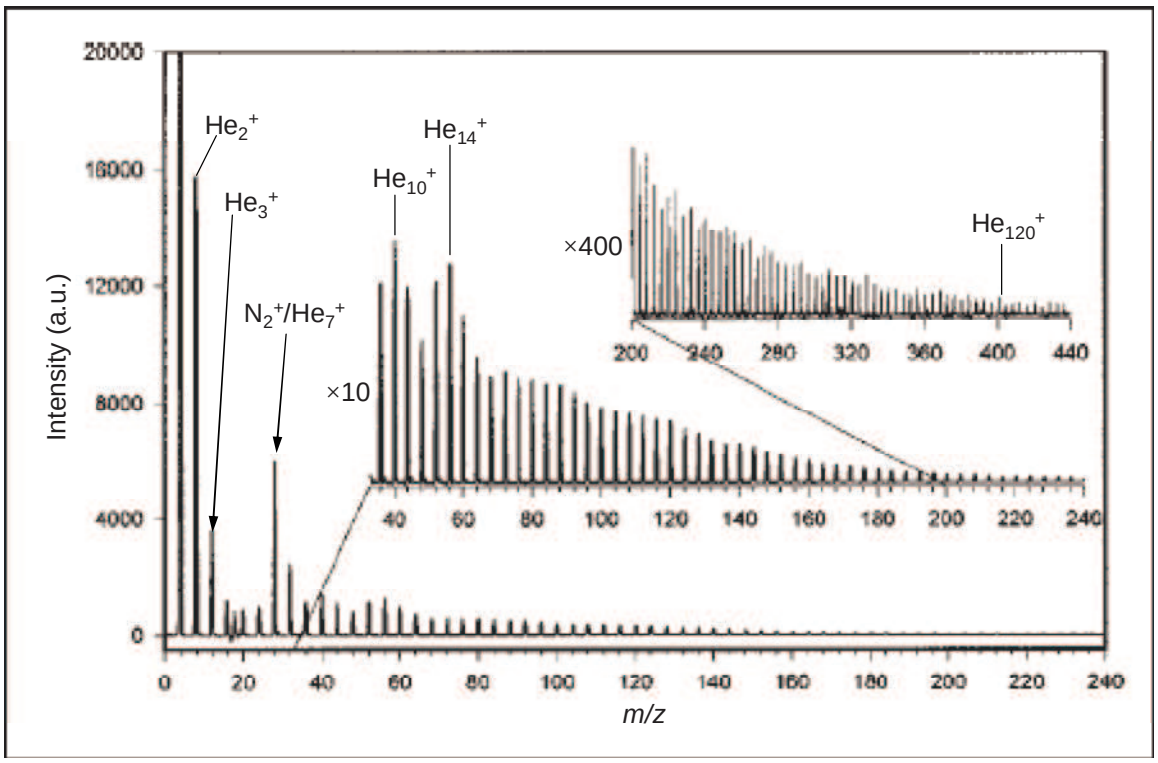

Figure 2.3 EI mass spectrum of pure helium droplets with $\overline{N}$ = 4000. Electron energy = 70 eV. Adapted from ref. [47].

the transfer of charge from helium to the dopant favorable. Indeed, it was observed that the appearance of dopant ions coincided with electron energies of at least 24 eV.[49] The direct ionization of dopants by electrons or photons of lower energy is possible;[51] however, ionization of a helium atom of the droplet has far higher probability of occurring, due to the large cross-section of the droplet. Of course, the presence of a dopant does not prevent the formation of He_N^+; rather it is a competing channel. As might be expected, the droplet size affects the likelihood of dopant ionization. It has been observed that the probability of dopant ionization increases as the droplet size is decreased.[45,52,53] In the limit of very large droplets, ionized dopants are rarely observed.

2.2.2 Cooling of Ionized Dopants

From the ionization potentials given above, it can be calculated that charge-transfer ionization of a dopant in a helium droplet liberates at least 12 eV of energy for most dopants. Thus, dopant ions are desolvated from the droplet in a similar fashion as He_N^+. Furthermore, charge-transfer ionization is a vertical process, which typically results in vibrationally excited ions and subsequent fragmentation. The rate of fragmentation varies widely between ions, but the overall trend is that small molecules fragment more rapidly than large ones.[54] To prevent fragmentation, the rate of cooling must be greater than the rate of fragmentation. Therefore, studying fragmentation patterns of molecules for which a gas phase mass spectrum is available provides information on the ability of helium droplets to cool ions. As expected, helium droplets were observed to effectively dissipate energy from the ionization process. The ionization of SF_6 resulted in the formation of SF_5^+, but all further fragmentation was suppressed.[49,55] Ionization of NO_2 resulted in fragmentation that was droplet size dependent.[45] Large droplets quenched all fragmentation and only the molecular ion, $NO_2^{+\cdot}$, was observed; however, at small droplet sizes fragmentation to NO^+ occurred. The extent to which helium droplets quench the fragmentation of the organic molecule triphenylmethanol (TPM) is shown in Figure 2.4.[56] Clearly, the amount of molecular ion present is greatly enhanced and the extent of fragmentation is significantly reduced when ionized in a helium droplet.

The study of TPM and a later study of the HCN molecule were the first to quantitatively analyze the cooling of ions provided by helium droplets.[57] It was discovered that helium droplets are able to dissipate the excess energy of the ionization

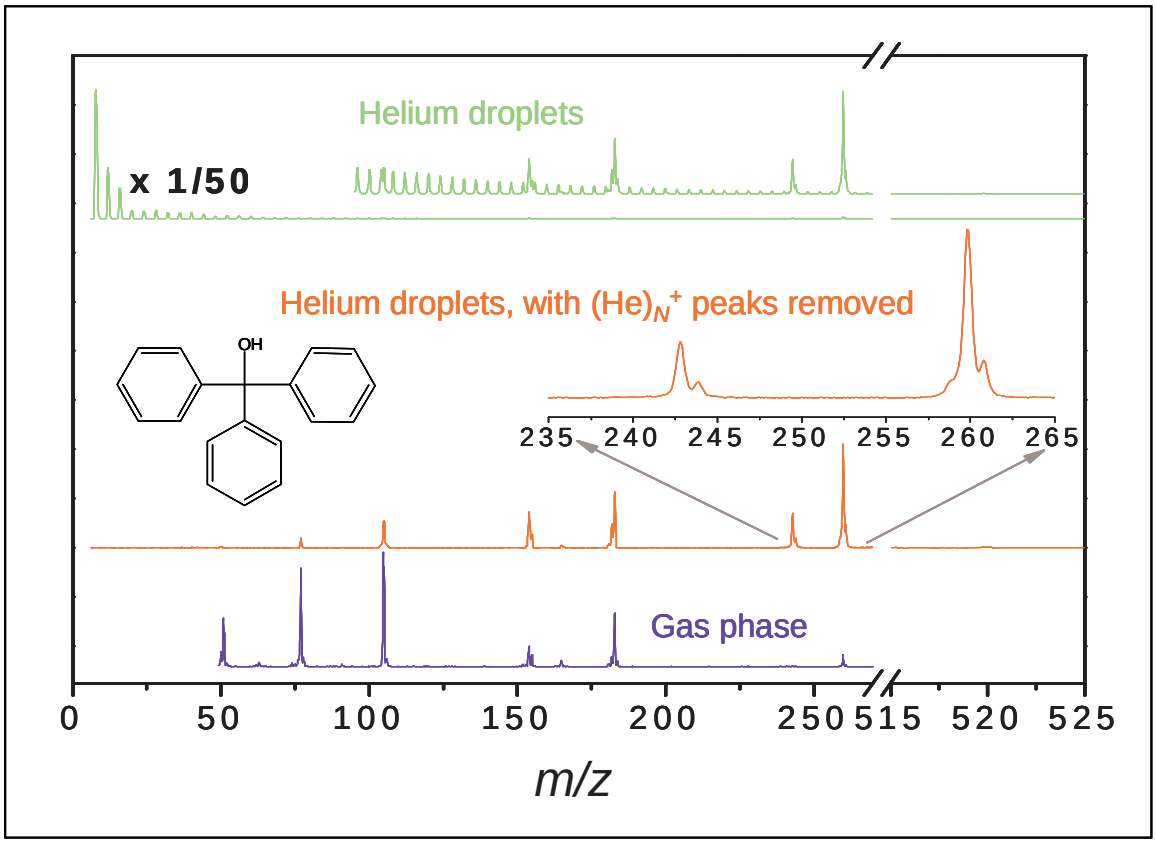

Figure 2.4 EI mass spectra of TPM in helium droplets (green, top), in helium droplets after subtracting the He_N^+ peaks (red, middle), and in the gas phase (blue, bottom). Molecular mass of TPM is 260.335 amu. Adapted from ref. [56].

process in a manner far more efficient than the thermal cooling mechanism described in Section 2.1 (5 cm^{-1}/atom). In the case of TPM, it was estimated that the first 5000 He atoms lost from the droplet removed ~22 cm^{-1} each.[56] For the cooling of HCN, it was observed that droplets with mean size, $\overline{N}$, of 2200 He atoms removed ~19 cm^{-1}/atom, but this value decreased with increasing droplet size.[57] The presence of two cooling regimes, non-thermal and thermal, was also observed. The idea of two distinct cooling mechanisms was recently explored through simulations of ionized neon clusters in helium droplets of N = 100. The simulations resulted in helium atoms that departed from the droplet with kinetic energies that fell into two distinct ranges: 3-7 cm^{-1} and 28-45

cm^{-1}.[58] These results strongly support the operation of both thermal and non-thermal cooling mechanisms for dissipation of energy after ionization.

2.2.3 Picking-Up Externally Generated Ions

Despite the impressive cooling abilities of helium droplets demonstrated in the above experiments, the ionization process often results in ejection of a bare ion from the droplet with energy that is not precisely known. Clearly, to achieve the maximum cooling afforded by the helium droplet, the ion must remain embedded within the droplet. The solvation of ions other than He_N^+ in a helium droplet has been accomplished by laser ablation of magnesium near the droplet nozzle.[59] In this way, Mg^+ was proposed to seed droplet formation and the resulting droplet size distributions were determined using time-of-flight mass spectrometry. Laser ablation additionally produces neutral and radical species that are also embedded in droplets. These studies did not demonstrate the ability to form clusters of neutral molecules with the ion. As described in Section 2.1, one of the most powerful abilities of the helium droplet technique is the controlled formation of clusters of various sizes through the doping of gas phase atoms or molecules into the droplet. To accomplish the formation of ion-neutral clusters in a helium droplet an ion with a low ionization potential must be used to avoid charge-transfer ionization from the embedded ion to the neutral molecule, which could possibly result in ejection from the droplet. Therefore, alkali cations, which have ionization potentials below those of other elements and molecules, are used in the work discussed in the subsequent chapters.

Alkali cations are closed-shell species, which are more easily studied by theoretical means than open-shell species. Thus, alkali cations are often the subject of

computational studies of ion solvation. Such studies have included the solvation by helium atoms in an effort to determine the strength and nature of binding of helium atoms to a cation. Interest in theoretical investigations stems from observations of increased local density of helium around cations in liquid helium.[60,61] The observed increase in density is attributed to electrostriction of the helium atoms by the ion and results in a solid-like shell of helium atoms around the cation, referred to as a "snowball."[62,63] The computational studies of such systems have recently confirmed these observations.[64-67] The formation of discrete solvation shells has been suggested, which are proposed to consist of 9-12 He atoms for Na^+, depending on the simulation method, and exhibit regular structure analogous to a classical solid. [65-67] It is hitherto unknown whether neutral molecules picked-up by a droplet with an embedded cation will form the desired ion-neutral cluster or if the snowball of solid helium will prevent ion-neutral cluster formation. The formation of such clusters is the focus of the work discussed in Chapter 4. The capture of alkali cations, which enables the subsequent ion-neutral cluster formation, is examined more thoroughly in Chapter 5.

CHAPTER 3

EXPERIMENTAL CONCEPTS AND DESIGN

3.1 Helium Droplet Formation

As discovered in 1961,[68] helium droplets are produced by expansion of a high pressure of helium through a cooled nozzle into vacuum. The mechanism by which droplets are formed depends on the stagnation pressure of helium, p_0, and nozzle temperature, T_0. All of the work discussed in this dissertation was performed with a stagnation pressure of 50 bar; thus, all conceptual descriptions will assume p_0 = 50 bar. When the nozzle temperature is ≥14 K, the isentropic expansion of gas results in condensation to droplets (Fig. 3.1a).[69] In this process, helium condenses into small precursor clusters upon expansion from the nozzle. Subsequently, the pressure of the expansion falls below the vapor pressure of the helium droplet and the droplet is cooled to 0.37 K by the evaporation of helium atoms from the surface. Below this temperature, the rate of evaporation of helium atoms from the droplet is negligible on the time scale of the experiment.[37] Production of droplets by the condensation of gas is referred to as Regime I expansion. The mean droplet size, $\overline{N}$, varies as a function of nozzle temperature according to the equation

$$\ln \overline{N} = 2.44 + 2.55 \ln \Gamma , \qquad (3.1)$$

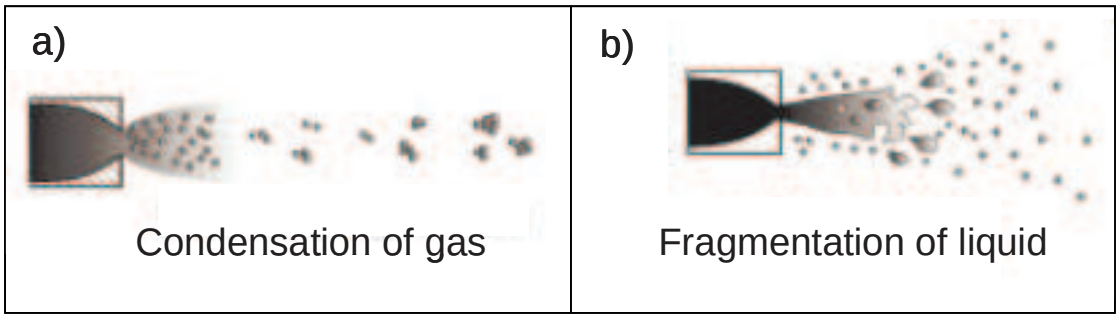

Figure 3.1 (a) Regime I droplet formation. (b) Regime III droplet formation. Adapted from [30].

where Γ is a dimensionless parameter described by:[70]

$$\Gamma = K_1^q K_2^{(1-q)}, \tag{3.2}$$

where q was empirically determined to be 0.6. K_1 and K_2 are kinetic and thermodynamic parameters, respectively, and are defined

$$K_1 = n_0 v (d_0/a_0)(2\gamma/\pi m)^{1/2} (T_{ref}/T_0)^{3/4} \text{ and} \tag{3.3}$$

$$K_2 = (p_0/A)(T_{ref}/T_0)^{5/2}, \tag{3.4}$$

where n_0 is the number density of He atoms, v is the volume per He atom in the droplet, d_0 is the nozzle diameter, a_0 is the speed of sound, γ is the droplet surface tension, m is the mass of a He atom, A is a vapor pressure constant, and T_{ref} is defined

$$T_{ref} = v^{2/3}\gamma/k, \tag{3.5}$$

where k is the Boltzmann constant. The surface tension of a droplet also exhibits a dependence on nozzle temperature:

$$\gamma = 2.05(T_c - T_0)k/v^{2/3}, \tag{3.6}$$

where T_c is the critical temperature of helium. The nozzle diameter used for all experiments discussed here was 5 μm. The dependence of mean droplet size on nozzle

temperature at p_0 = 50 bar is shown in Figure 3.2. Clearly, lower nozzle temperatures result in larger mean droplet sizes.

At nozzle temperatures ≤11 K, the helium gas in the nozzle condenses into a liquid and droplet formation results from the fragmentation of liquid upon expansion into vacuum (Fig. 3.1b).[69] The droplets then cool to 0.37 K by evaporation of atoms from the surface. Production of droplets under these conditions is referred to as Regime III expansion. Mean droplet sizes in Regime III also vary as a function of nozzle temperature according to

$$\overline{N} = \frac{80\pi}{3}\frac{\gamma}{m}\left(\frac{d_0}{a_0}\right), \qquad (3.7)$$

where γ, m, d_0, and a_0 are the same variables defined for Eq. 3.3.[71] Values of $\overline{N} > 10^6$ He atoms result from Regime III expansion conditions (Fig. 3.2).

Between Regimes I and III, 11 K < T_0 < 14 K, is Regime II, in which droplet formation is thought to result from a combination of condensation of gas and fragmentation of liquid.[69,72] Mean droplet sizes produced in these expansions are estimated to be $>10^5$ He atoms, but a quantitative expression has not been developed.

3.2 Droplet Size Distributions

Helium droplet formation is a statistical process that results in a distribution of droplet sizes. The distribution of droplet sizes produced in a Regime I expansion can be described by the log-normal function:[73]

$$P_N(N) = \left(N\sigma\sqrt{2\pi}\right)^{-1} \exp\left[\frac{-(\ln N - \mu)^2}{2\sigma^2}\right]. \qquad (3.8)$$

$P_N(N)$ is the probability of producing a droplet consisting of N helium atoms. The

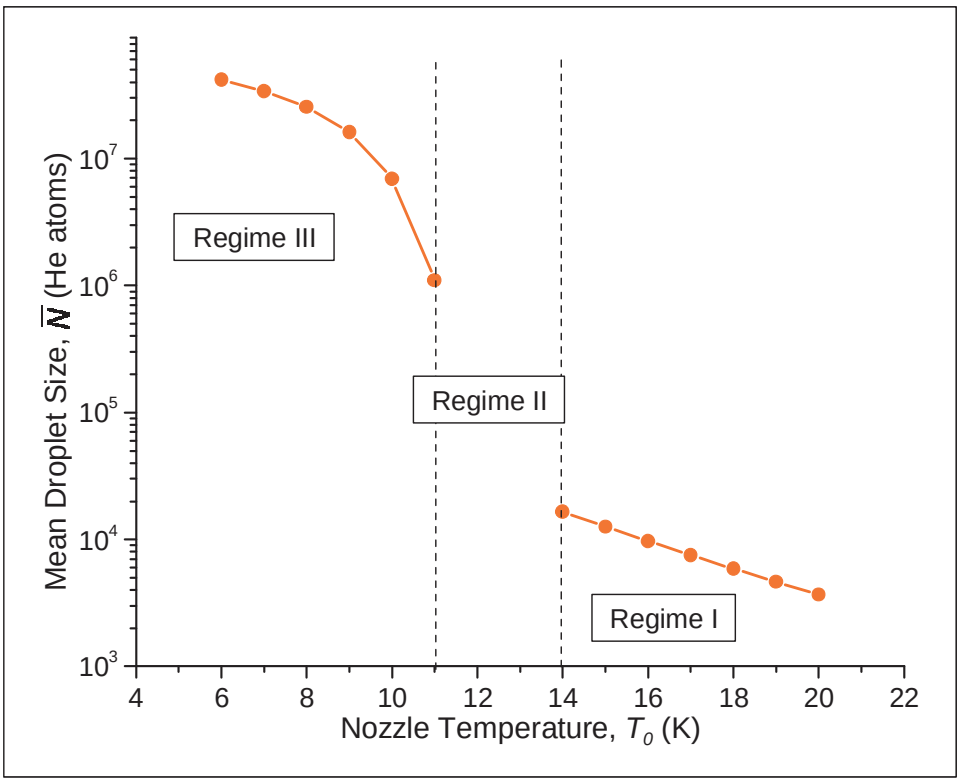

Figure 3.2 Dependence of mean droplet size, $\overline{N}$, on nozzle temperature, T_0, for p_0 = 50 bar and d_0 = 5 μm.

parameters σ and μ are the standard deviation and the mean of the distribution of ln N, and are defined by the following equations:

$$\mu = \ln(\overline{N}) - \frac{1}{2}\ln\left[\left(S/\overline{N}\right)^2 + 1\right], \tag{3.9}$$

$$\sigma = \sqrt{\ln[(S/\overline{N}^2) + 1]}, \tag{3.10}$$

$$\overline{N} = \exp\left(\mu + \sigma^2/2\right), \tag{3.11}$$

$$S = \exp\left(\mu + \sigma^2/2\right)\sqrt{\exp(\sigma^2 - 1)}, \tag{3.12}$$

$$\Delta N_{1/2} = \exp\left(\mu - \sigma^2\right)\left[\exp\left(\sigma\sqrt{2\ln 2}\right) - \exp\left(-\sigma\sqrt{2\ln 2}\right)\right], \tag{3.13}$$

where S and $\Delta N_{1/2}$ are the standard deviation and half-width of $P_N(N)$. Experiments have

shown that the standard deviation and half-width of the distributions vary approximately linearly with mean droplet size, and were determined to be $S = 0.65\,\overline{N}$ and $\Delta N_{1/2} = 0.87\,\overline{N}$, respectively.[74]

Using the mean droplet size values from Figure 3.2, the distribution of droplet sizes produced at a given set of nozzle conditions can be calculated (Fig 3.3). In accordance with the log-normal function (Eq. 3.8), droplet size distributions with a larger mean have a larger standard deviation. Indeed, the effect of increasing the mean droplet size on the width and height of the distribution can be seen in Figure 3.3. Warmer nozzle temperatures, which correspond to smaller mean droplet sizes, result in narrower distributions of droplet sizes, whereas colder nozzle temperatures result in broader distributions. An important property of the droplet production process is that, despite the range of sizes, all droplets produced at a given nozzle temperature have a narrow distribution of velocities, $\Delta v/v \approx 0.01\text{-}0.03$.[69]

Production of droplets via Regime III expansion conditions results in a distribution of droplet sizes (Fig. 3.4) that can be described by a linear-exponential function:[71,75]

$$P_N(N) = \frac{1}{N}\exp\left(-N/\overline{N}\right). \qquad (3.14)$$

Regime II expansions also result in a distribution of droplet sizes, but like the mean droplet size, a quantitative description of the droplet size distribution produced at these conditions has yet to be determined. The lack of quantitative descriptions for mean droplet size and droplet size distribution is relevant to the results discussed in Chapter 4, as Regime II expansion conditions were implemented.

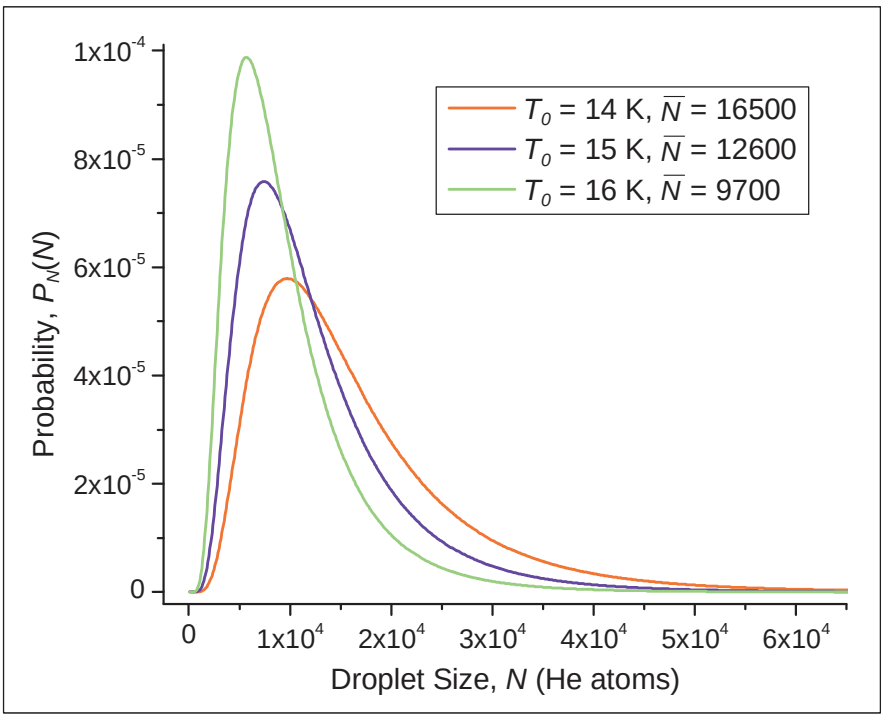

Figure 3.3 Droplet size distributions resulting from Regime I expansion for T_0 = 14 K (red), 15 K (blue), and 16 K (green) at p_0 = 50 bar.

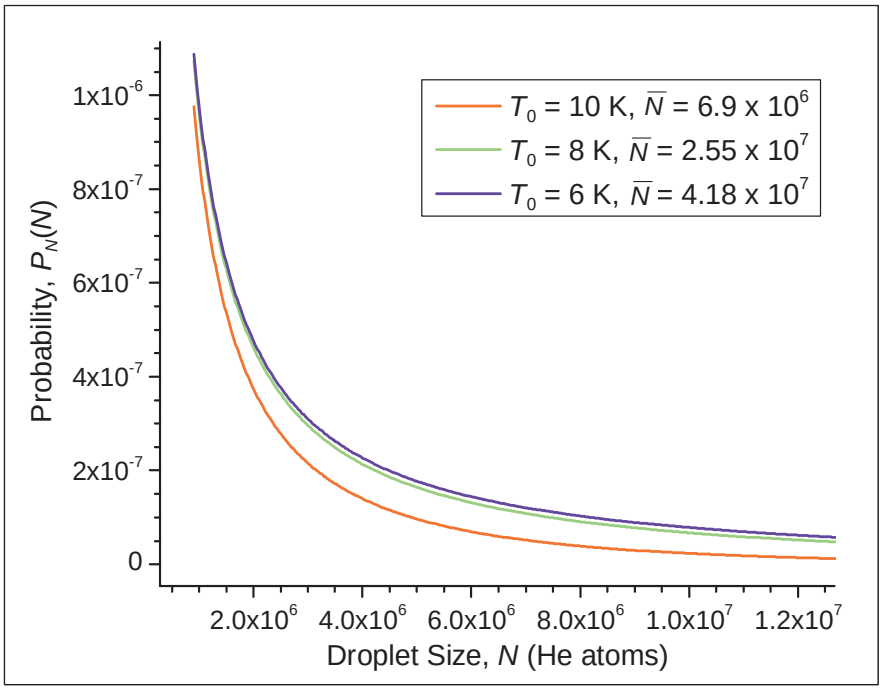

Figure 3.4 Droplet size distributions resulting from Regime III expansion for T_0 = 10 K (red), 8 K (green), and 6 K (blue) at p_0 = 50 bar.

3.3 Dopant Pick-up

As mentioned in Section 2.1, there is a favorable potential for gas phase neutral molecules to be solvated by a helium droplet.[43] As a result of the favorable interaction with helium versus vacuum, a helium droplet will pick-up nearly all neutral molecules it encounters during its flight. The number of molecules encountered by a droplet is determined by the cross-sectional area of the droplet and the number density of molecules throughout the flight path of the droplet.

Assuming that the droplet has a uniform density that is similar to that of bulk liquid helium, ρ = 0.0218 Å^{-3},[74] and is spherical in shape, the volume of the droplet can be calculated as a function of droplet size, N:

$$V = \frac{N}{0.0218} = \frac{4}{3}\pi r^3, \tag{3.15}$$

where r is the radius of the droplet in Å. Equation 3.15 yields a useful expression for droplet radius as a function of droplet size:

$$r = 2.22\sqrt[3]{N}\,. \tag{3.16}$$

Knowing the droplet radius permits calculation of the cross-sectional area, σ (Å^2):

$$\sigma = \pi r^2 = 15.5N^{2/3}. \tag{3.17}$$

Multiplying the cross-sectional area by the pathlength, L (Å), of the pick-up region provides the volume of the cylinder, V_{cyl} (Å^3), traversed by the droplet:

$$V_{cyl} = \sigma L = 15.5N^{2/3}L\,. \tag{3.18}$$

Multiplying V_{cyl} by the number density, η (Å^{-3}), yields β, the expected number of molecules encountered by the droplet as it traverses the cylinder:

$$\beta = V_{cyl}\eta = 15.5N^{2/3}L\eta\,. \tag{3.19}$$

Once a molecule is picked-up, it is rapidly cooled to the temperature of the droplet by the evaporation of surface atoms.[37] If the number density of molecules is such that a second molecule is encountered, it will also be picked-up and cooled down by the same means. Due to the potential of the droplet and the long-range interactions of the picked-up molecules, the two dopants will form a cluster within the droplet. The condensation energy associated with cluster formation is rapidly dissipated through the same evaporative mechanism. Thus, the rate of cooling is such that, in the case of multiple pick-ups, each molecule is completely cooled before the next one is encountered. This characteristic allows each pick-up event to be treated independently. Therefore, the pick-up of dopant molecules by helium droplets can be described by the Poisson distribution:[76]

$$P(k,N) = \frac{\beta^k e^{-\beta}}{k!}, \tag{3.20}$$

where $P(k,N)$ is the probability that a droplet of size N picks-up k molecules and β is given by Eq. 3.19.

The dependence on droplet size for the pick-up of 1-5 molecules at a pressure of 2.0×10^{-7} torr over a pathlength of 0.5 m is shown in Figure 3.5. These values are similar to the background pressure and pathlength of the pick-up chamber in the current studies. Clearly, pick-up of multiple molecules for the formation of large clusters is most probable at larger droplet sizes. At droplet sizes typically used for spectroscopy studies ($\overline{N}$ = 3000), the most probable event is pick-up of zero molecules, that is, most droplets of that size will not pick-up background impurities.

In Section 3.2, the ability to calculate the distribution of droplet sizes produced at a given nozzle temperature was demonstrated. The dependence of dopant pick-up on

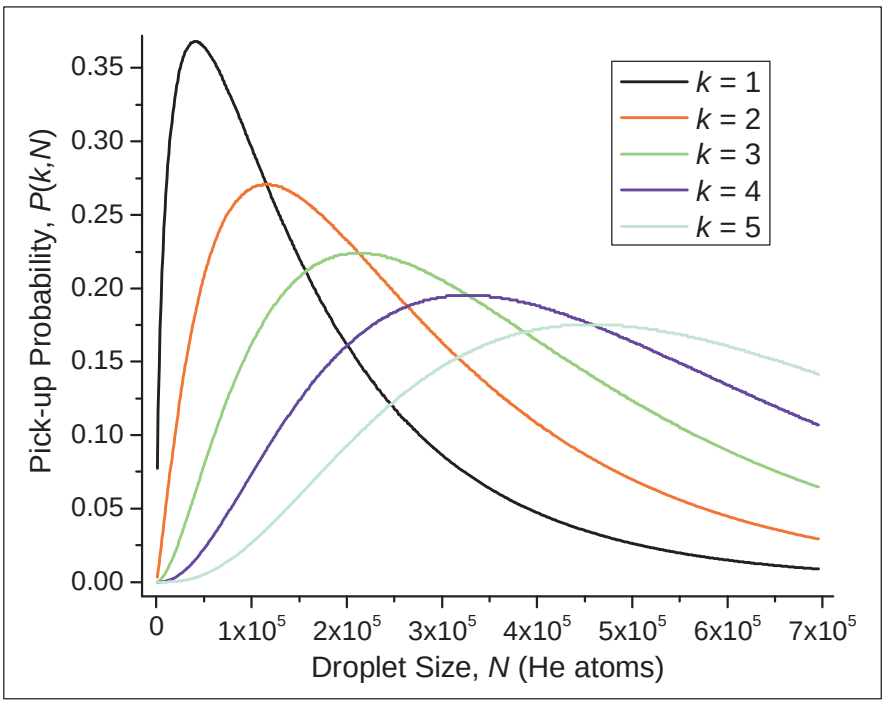

Figure 3.5 Dependence of the probability for pick-up of 1-5 molecules on droplet size. Calculated for pressure of 2.0×10^{-7} torr over a pathlength of 0.5 m.

droplet size was demonstrated above. The convolution of the droplet size distribution (Eq. 3.8 or Eq. 3.14) with the Poisson distribution (Eq. 3.20) yields the probability that a droplet of size N is produced and picks-up k molecules:

$$P_{occ}(k,N) = P_N(N) \times P(k,N), \qquad (3.21)$$

where P_{occ} is referred to as the occupancy probability. Occupancy probability distributions calculated using $\overline{N}$ = 16,500 (Regime I), and the same pressure and pathlength parameters used above, are shown in Figure 3.6. Note that the curves for k = 3-5 are multiplied by factors of 10, 100, and 1000, respectively, to make them observable on a linear y-axis with the curves for k = 1 and 2. Clearly, the log-normal distribution of droplet sizes is the dominant factor in the occupancy probability distributions. The occupancy probability distribution is relevant to the discussion of results in Chapter 4.

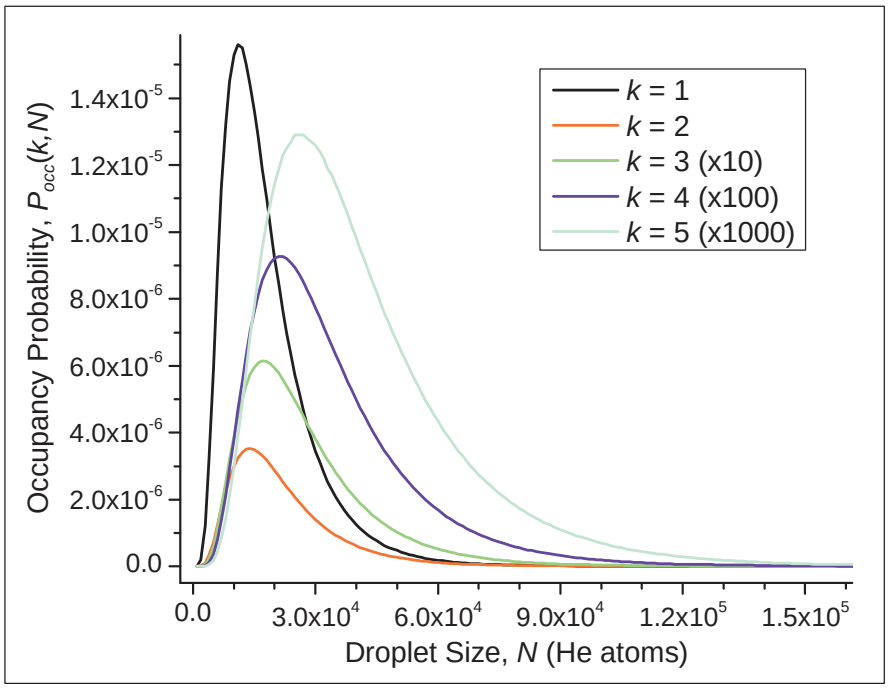

Figure 3.6 Occupany probability distributions for capture of 1-5 molecules. $\overline{N}$ =16,500 He atoms, pressure = 2.0 × 10^{-7} torr over a pathlength of 0.5 m.

3.4 Helium Droplet Instrument

3.4.1 Droplet Source

The production of helium droplets is accomplished by a continuous expansion of a high pressure of helium through a cold nozzle into vacuum. This concept is straightforward, but there are several factors that need to be taken into consideration. Perhaps the most important aspect of droplet production is the nozzle. The same nozzle was used for all experiments discussed in this dissertation.

The nozzle consists of a 3 mm o.d. × 0.25 mm thick platinum disc with a 5 μm aperture (Philips) crimped into a 1.5” long × 0.25” o.d. custom copper tube. It is vital that the disc be crimped into the tube in such a way that there are no leaks around the

circumference of the disc. The copper tube is placed in a copper clamp. The copper clamp is cooled by a closed cycle helium refrigerator (Sumitomo SRD-415D), which is capable of supplying 1.5 W of cooling power at 4.2 K to the second stage and 45 W at 50 K to the first stage. The thermal link from the coldhead to the nozzle is provided by a copper disc attached to the second stage of the coldhead and strips of copper that run from the copper disc to the copper clamp (Fig. 3.7). The copper strips also serve to minimize the impact of vibrations of the helium refrigerator on the nozzle position. In a newer helium droplet instrument, the use of copper braid has been demonstrated as even more effective at isolating the nozzle from vibration.[77] Slight adjustments to the nozzle position are made by a two-dimensional translation stage, which allows for precise alignment with the skimmer. The skimmer, which has a diameter of 400 μm and is located 2 cm downstream from the nozzle, prevents excess helium from reaching the pick-up chamber and results in a collimated beam of helium droplets. The translation mount is described briefly below.

To reach the lowest temperatures possible, the heat load on the nozzle must be minimized. Therefore, the entire second stage of the coldhead is shielded from blackbody radiation by a 1/16" thick copper shield attached to the first stage of the coldhead. Additionally, the helium gas undergoes two steps of pre-cooling before reaching the nozzle. First, it is passed through a copper tube that is in thermal contact with the first stage shield. Then, it is cooled further by wrapping the copper tube around the copper disc attached to the second stage of the coldhead (Fig. 3.7). The nozzle mount for the translation stage (Fig. 3.8) is also designed with cooling in mind. The nozzle clamp is held in an aluminum mounting bracket by nylon screws, which limit the thermal

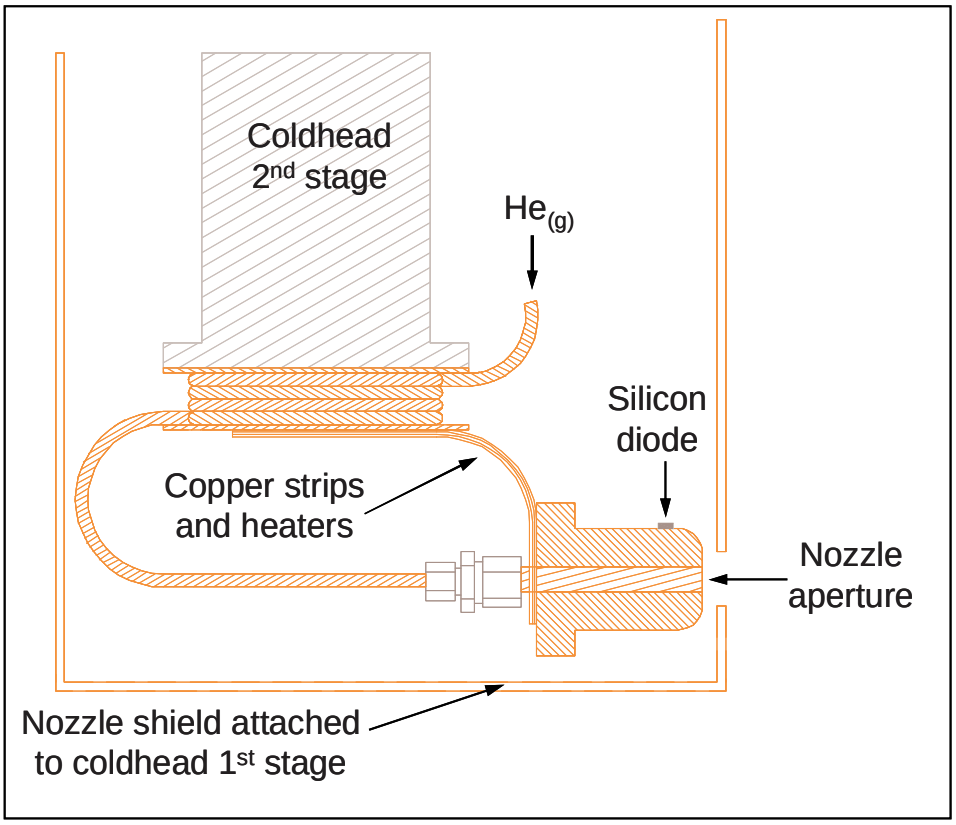

Figure 3.7 Illustration of nozzle assembly.

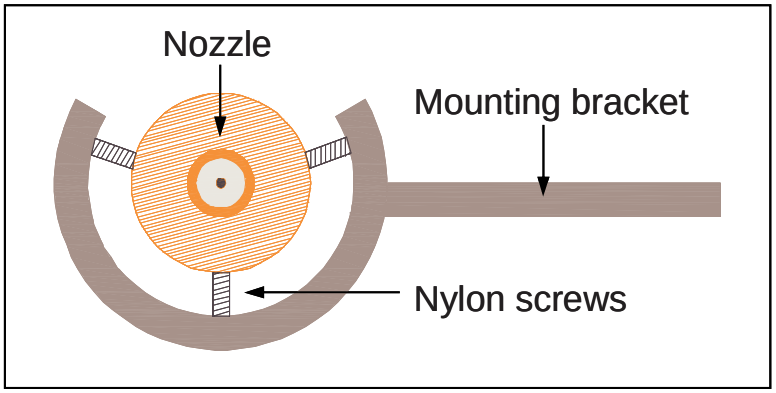

Figure 3.8 Head-on view of nozzle mount for 2-D translation.

contact between the nozzle clamp and the mounting bracket. The aluminum bracket is thermally linked to the first stage shield by copper strips to minimize the amount of

blackbody radiation it produces. The arm of the mounting bracket is then attached to a two-dimensional translation stage by a Bakelite™ clamp, which minimizes the thermal connection between the mounting bracket and the translation stage.

Nozzle temperature is measured with a silicon diode (Lakeshore DT-471 SD) placed on top of the nozzle clamp as near to the nozzle aperture as possible (Fig. 3.7). The signal from the silicon diode is read by a temperature controller (Lakeshore 321), which provides power to strip heaters (Minco HK5160R78.4L12A) that are used to control the nozzle temperature. The heaters are placed between the copper cooling strips linking the coldhead and nozzle (Fig. 3.7). The leads to the diode and heaters use fine gauge wire and are placed in thermal contact with the first stage shield to minimize the heat load that they introduce. With the described apparatus, measured nozzle temperatures can reach a minimum of less than 6.0 K at p_0 = 50 bar and a maximum of over 30 K, with control of the nozzle temperature to 0.1 K precision.

Operation of the nozzle at low temperature and high pressure introduces an additional factor to be considered: gas flux. The flux of droplets, *F*, depends upon nozzle temperature, pressure, and diameter according to the relationship:[77]

$$F \propto p_0 d_0^2 T_0^{-1/2}. \qquad (3.22)$$

Therefore, the amount of gas to be evacuated from the chamber increases as nozzle temperature decreases. To accommodate the high throughput of gas into the vacuum chamber, a diffusion pump (Varian HS-20) with maximum pumping speed of 21,000 L/s is used to evacuate the source chamber. This diffusion pump is backed by a high throughput roots blower. This vacuum system is able to maintain a pressure $<10^{-4}$ torr at

the highest gas loads produced by the nozzle, which is low enough for the pump and helium expansion to operate as intended.

The source of helium used in the production of droplets is 99.9999% purity gas. This degree of purity is required to minimize the amount of impurities that freeze onto nozzle surfaces, which would result in accumulation and clogging of the nozzle. The helium gas is passed through a 0.5 μm filter before reaching the coldhead and through a second 0.5 μm filter that is press fit into the coupling union between the coldhead second stage and the nozzle.

3.4.2 Droplet Doping

After passage through the skimmer cone, a collimated beam of droplets proceeds to travel through the pick-up chamber (Fig. 3.9), where droplet doping occurs. The skimmer also serves as an interface for differential pumping between the source chamber and pick-up chamber, which operate at typical pressures of 5.0×10^{-5} torr and 2.0×10^{-7} torr, respectively.

Alkali cations are produced by thermionic emission from a resistively heated tungsten filament coated with a zeolite paste. The rate of ion emission is temperature-dependent:[78]

$$\frac{\psi_+}{\psi_0} = \left(\frac{g_+}{g_0}\right)\exp\left[\frac{(\varphi - \Phi)}{kT}\right], \tag{3.23}$$

where ψ_+ and ψ_0 are the emission rates of cations and neutrals, respectively, g_+ and g_0 are the respective statistical weights of the ionic and neutral states, φ is the work function, Φ is the ionization potential, k is the Boltzmann constant, and T is the temperature. The preparation of the zeolite paste is adapted from that described by Draves et al.[79] The

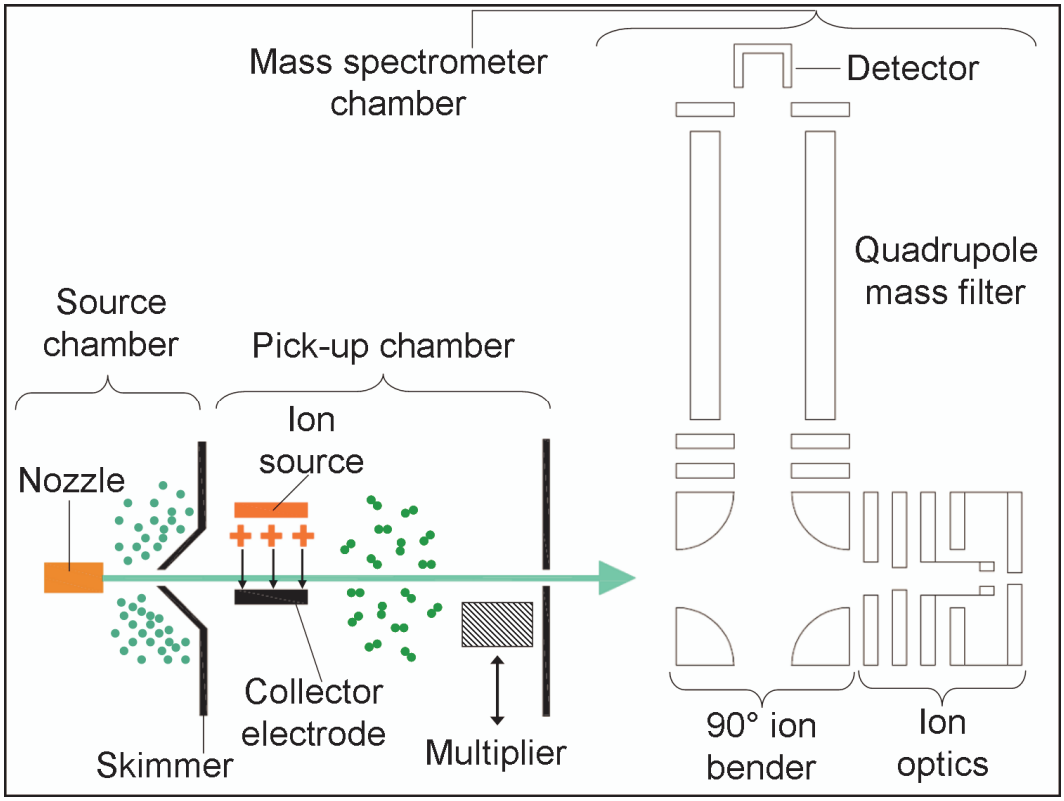

Figure 3.9 Schematic of helium droplet instrument for doping of droplets with alkali cations.

zeolite matrix (Sigma-Aldrich Molecular sieves, 13X, $Na_{86}[(AlO_2)_{86}(SiO_2)_{106}] \cdot xH_2O$) is rinsed with an excess of saturated NaCl or LiCl solution, to produce Na^+ or Li^+-enriched paste, respectively. The wet zeolite is then allowed to dry. After performing the rinse/dry cycle three times, the matrix is moistened to the point of a paste-like consistency. The cation-enriched paste is then applied to a coiled tungsten filament (Aldrich, 0.25 mm diameter) that has been repeatedly heated to a light orange glow. After application of the zeolite paste, the ion source is heated moderately for an hour to drive off moisture before placement in the vacuum chamber. In the vacuum chamber, shortly after initial pump-down, the ion source is heated just below the temperature necessary for thermionic emission, as determined by monitoring ion current, for at least

12 hours to drive off any residual moisture. Finally, the filament is briefly heated to a bright glow and quickly returned to low temperature. This annealing step improves the consistency of the ion current emitted from the source. In the case of Li^+ sources, an additional 12 hour period at elevated temperature is implemented to emit remaining Na^+ from the zeolite matrix since the native zeolite is rich in Na^+.

The ion source is located in the pick-up chamber near the source chamber. The ion source is positioned on one side of the droplet beam and a collector electrode is positioned on the opposite side. The collector electrode is made of 1/8" diameter copper tube. A negative dc potential is applied to the collector electrode, which extracts the ions in the region of the droplet beam and defines the kinetic energy of the ions. The collector electrode is also used to monitor the ion current. The measured ion current increases with increasingly negative potentials applied to the collector electrode.

For the majority of the experiments discussed in the subsequent chapters, no gas is added to the chamber. However, when additional gas is introduced to the pick-up chamber, it is added through an effusive source. The effusive source is quite simple: it consists of a supply of gas that is regulated by a fine metering valve (Parker) and enters the vacuum chamber through a 500 μm diameter tube. This tube is positioned in the chamber downstream of the ion source, so that pick-up of neutral molecules by helium droplets likely occurs after an ion has been captured.

3.4.3 Detection

The instrument is equipped with two means of detecting ion-doped droplets (Fig. 3.8). A translatable electron multiplier located in the pick-up chamber, downstream of the ion source. The use of adjustable detector position for the determination charged

droplet sizes is described in Chapter 5. The electron multiplier is useful for optimizing the conditions used to produce charged droplets, but provides no information about the charged species other than their relative abundance. To examine the composition of the charged droplets a mass spectrometer is used.

A linear quadrupole mass spectrometer (Extrel CMS) is located in a third differentially pumped vacuum chamber (Fig. 3.8). The pressure of this chamber in the absence of the helium droplet beam is 4.0×10^{-9} torr. The extremely low pressure in this chamber is important because it nearly eliminates the possibility of droplet doping in this region, enabling pressure values from the pick-up chamber to be used accurately when applying the pick-up statistics discussed in Section 3.2. The mass filter is oriented orthogonal to the droplet beam, effectively minimizing undesirable effects caused by collisions with scattered helium atoms from the droplet beam. This instrument is equipped with an axial electron ionization source and 90° bender. For analysis of the composition of charged droplets, the EI filament was turned off to prevent ionization of helium atoms and ensure that the source of ions was limited to those produced by the thermionic emission source in the pick-up chamber. The ionization region is oriented such that it is downstream of the 90° bender (Fig. 3.8). In this configuration, the ionization region is used as a desolvation region for ion-doped droplets. The desolvation process and other experimental details will be described in subsequent sections as appropriate.

CHAPTER 4

CLUSTERS OF NEUTRAL MOLECULES WITH SODIUM CATIONS

This chapter describes the first observation of ion-neutral clusters in superfluid helium nanodroplets. Sodium cations generated by thermionic emission were directed toward a beam of helium droplets. Downstream of the ion source, the Na^+-doped droplets encountered and picked-up neutral molecules: H_2O, N_2, and HCN. The helium-solvated ion-neutral clusters were desolvated and analyzed with a mass spectrometer. The mass spectra contain peaks assigned to $[Na(H_2O)_n]^+$, $[Na(H_2O)_nN_2]^+$, and $[Na(H_2O)_n(HCN)_m]^+$ complexes with n = 6-43 and m = 0-3. The results suggest that the snowball of solid helium that presumably forms around the captured Na^+ does not prevent subsequently captured species from clustering with the cation. Ab initio calculations indicated that binding of H_2O and N_2 with Na^+ occurs through barrierless insertion into the snowball.

4.1 Experimental

For the work described in this chapter, the instrument was configured as illustrated in Figure 3.9. Helium droplets were formed by expanding helium at p_0 = 50 bar. Upon entering the pick-up chamber, the droplet beam was modulated by a chopper (not shown) to allow for phase-sensitive detection. The sodium cation source was

prepared as described in Section 3.4.2. Production and transmission of Na^+-doped droplets was optimized using the electron multiplier located near the exit of the pick-up chamber. The signal from the electron multiplier was processed by a lock-in amplifier referenced to the droplet beam chopper, eliminating any contributions from stray ions. The mean droplet size and bias potential of the Na^+ collector electrode were then adjusted to maximize the number of ion-doped droplets reaching the electron multiplier.

In this geometry, there is an intrinsic trade-off. Using a large negative bias potential increases the flux of Na^+ crossing the droplet beam. The resulting higher kinetic energy of the Na^+ presumably requires larger droplets for capture. Larger droplets are also required to overcome the attractive potential of the collector. The nozzle conditions that produce large droplets, however, produce them in low numbers. The optimum nozzle temperature and bias potential were 13.0 K and -200 V, respectively, and these optimum parameters were used to collect all data. Nozzle conditions of T_0 = 13.0 K and p_0 = 50 bar result in an expansion from a state close to the critical point of helium, which corresponds to Regime II expansion conditions discussed in Section 3.2.[69] Although the mean droplet size formed in such expansions has been measured as $>10^5$ atoms/droplet,[72] the distribution of droplet sizes generated near the critical point is not well-characterized.

As noted above, the configuration limited the experiment to large droplets. The use of a collector electrode biased at -200 V creates a potential well from which the charged droplets must escape to be detected. Assuming a droplet velocity of 350 m/s,[69,73] a charged droplet must consist of approximately 10^5 He atoms to have sufficient kinetic energy to overcome this barrier. Droplets that do escape are deflected

off-axis by the negative collector electrode potential. Assuming that all droplets start on the beam axis and do not exhibit any divergence, SIMION[80] simulations show that only charged droplets with greater than ~10^6 He atoms maintain trajectories that allow passage into the mass spectrometer chamber. In reality, the initial neutral droplet beam is slightly divergent, so smaller charged droplets that start off-axis may be steered toward the axis. Nevertheless, a lower limit is placed on the sizes of droplets that may be detected by the mass spectrometer. Although the droplets used are too large to be useful in spectroscopy experiments,[29] the goal of this work was to demonstrate the capture of Na^+ and the assembly of ion-neutral clusters in helium droplets.

After ion-doping, neutral dopants may be added to the droplet by introducing gas molecules into the pick-up chamber in the volume following the ion source, as described in Section 3.4.2. The pressure of this chamber in the absence of the helium droplet beam was 2.8×10^{-7} torr. Although this pressure is low enough to avoid contamination of spectroscopically interesting droplets ($\overline{N}$ < 5000 He atoms), the larger droplets used in the current study encounter and pick-up ambient molecules in the absence of an introduced gas.

Using only the electron multiplier, it is not possible to determine the identity of the ion contained in the droplet. The ionization potential of helium is 24.6 eV,[50] so it is possible that the impact of a 200 eV sodium cation with the neutral droplet could result in charge transfer:

$$Na^+ + He_N \rightarrow Na + He_N^+. \qquad (4.1)$$

For large helium droplets, 10^5-10^6 atoms, it has been shown that helium ions created by electron ionization of the droplets can remain solvated.[48,55,81] To confirm the capture

of Na^+ by helium droplets, the electron multiplier was moved out of the beam path and the mass spectrometer was used to detect the captured ions after a desolvation step. In the configuration described in Section 3.4.3 (Fig. 3.9), the ionization region was used as a desolvation region for ion-doped droplets since the mass filter range (1-1000 Da) is not large enough to analyze intact, ion-doped droplets.

The large difference between the mass of the doped droplet and the mass of the captured ion is exploited by applying potentials to the ion optics such that the trajectories of the incoming ion-doped droplets are perturbed only slightly. The large droplets studied have kinetic energies on the order of 2 keV (assuming 350 m/s velocity[69,73]), so they are able to travel through the electric field generated by the 90° bender without significant changes in trajectory and reach the ion optics on the opposite side (Fig. 4.1). The ions are desolvated and extracted to the quadrupole mass spectrometer for analysis. A detailed view of the ion optics and the corresponding potentials applied to each element is shown in Figure 4.1. SIMION modeling of this region is shown in Appendix A.

Due to the divergence of the droplet beam, the beam waist at the desolvation region is several millimeters larger than the inner diameter of the ion optics,[82] as shown in Figure 4.1. This leads to several plausible explanations for the desolvation mechanism. Based on the divergence and kinetic energies of the droplets in the beam, it may be possible for ion-doped droplets to strike the positively-biased ion optic element and break apart, from which the bare ion is repelled toward the 90° bender. Neutral droplets may also collide with the ion optic elements. The scattered helium atoms could provide a means for the collisional desolvation of the ions from the droplets. Also, the

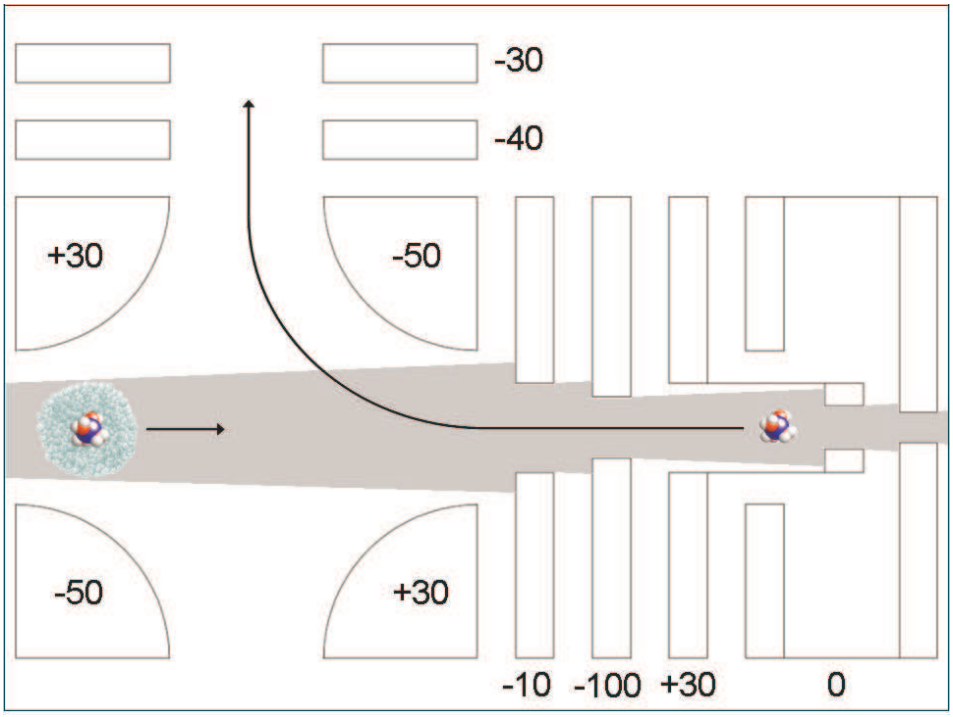

Figure 4.1 Close-up view of 90° bender and ion optics (droplet and cluster images not to scale). Values are dc potentials applied to each element, in volts. The shaded region represents the estimated divergence of the neutral droplet beam.

electric field created by the ion optic elements may promote the ejection of ions from droplets during these processes. Arguments may be developed to support each of these mechanisms and it is expected that the observed desolvation is caused by some combination thereof. Concerning the results discussed here, it is sufficient to say that the ions are desolvated from the droplets, directed to the bender, and extracted into the quadrupole mass spectrometer for analysis. The output from the mass spectrometer is processed by a lock-in amplifier to eliminate any signals other than those resulting from ion capture by the helium droplets.

4.2 Results

4.2.1 $[Na(H_2O)n]^+$ and $[Na(H_2O)nN_2]^+$ Clusters

A mass spectrum of ions desolvated from superfluid helium droplets is shown in Figure 4.2. Either blocking the helium droplet beam upstream of the ion source or ceasing Na^+ emission from the source caused the mass spectrum to vanish, confirming that the signals were indeed due to thermionically emitted Na^+ impacting the helium droplets. The spectrum consists of an envelope of evenly-spaced peaks, separated by 18 Da. Each peak is located at $m/z = 18n + 23$, where n is an integer value, indicating that these signals arise from $[Na(H_2O)_n]^+$ clusters. This is perhaps not surprising, given that the most abundant background gas present in the pick-up chamber is H_2O, as measured with EI mass spectrometry.

From the masses of the cluster ions in Figure 4.2, it can be seen that the majority of the desolvated ions contain 10-20 water molecules. Recall that the droplets expected to reach the mass spectrometer have at least 10^6 atoms/droplet. Using the background pressure of water in the chamber with the pick-up statistics that were described in Section 3.3,[76] it can be estimated that a droplet of 10^6 He atoms is most likely to pick-up 13 or 14 water molecules during its flight through the instrument. This calculation assumes that the pick-up statistics are unchanged from neutral droplets. The pick-up calculation also does not take into account the decrease in droplet cross-section caused by the evaporation of helium atoms that accompanies the dissipation of the condensation energy for ion-neutral cluster formation as this decrease is negligible for droplets of the sizes detected. It is important to note that this calculation represents the number of molecules a droplet is expected to encounter *after* Na^+ capture, it does not address the loss of helium

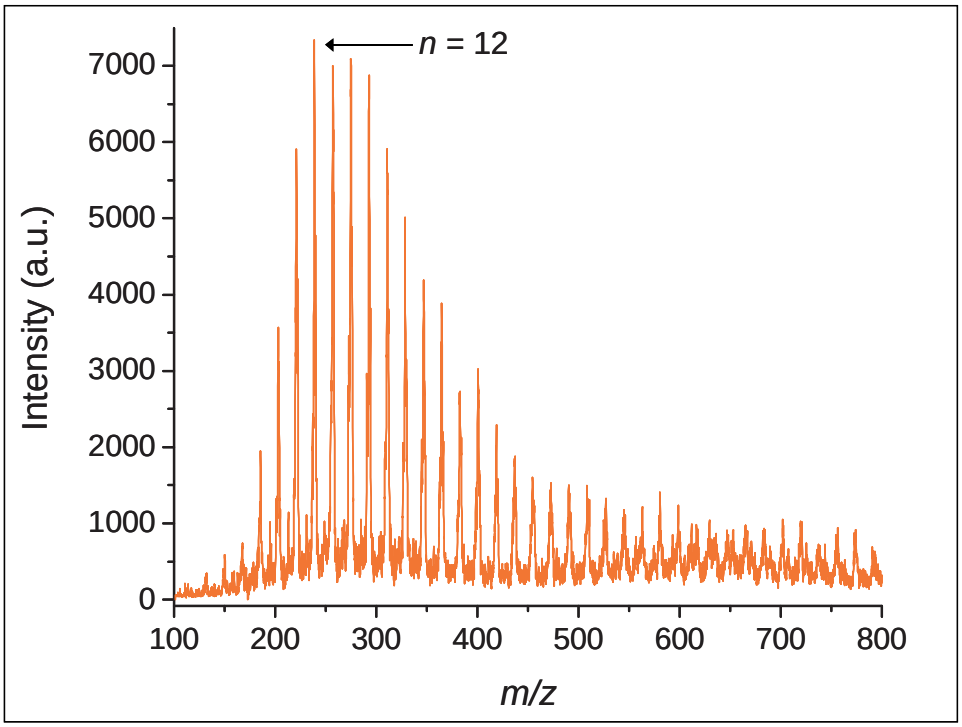

Figure 4.2 Mass spectrum of $[Na(H_2O)_n]^+$ clusters formed in superfluid helium nanodroplets.

atoms due to dissipation of the ion energy. This topic is discussed in Chapter 5. Additionally, while droplets larger than 10^6 atoms can make it downstream to the mass spectrometer, smaller ones cannot. Since larger droplets tend to capture a greater number of impurities, it is expected that the resulting distribution of ion-neutral cluster sizes would be asymmetric. That is, it is expected that the abundance of ion clusters with fewer than 10 water molecules would drop off more abruptly than those with a greater number of water molecules. In fact, this is very similar to the observed results. In Figure 4.2 it can be seen that the ion intensities rise quickly from $n = 6$ to $n = 12$ and then decrease more slowly with increasing n.

Further inspection of the spectrum in Figure 4.2 reveals a low intensity envelope of peaks starting at *m/z* 195. These peaks are marked in Figure 4.3 by arrows and are

shifted from the $[Na(H_2O)_n]^+$ peaks by 10 Da. Most likely, these peaks result from clusters formed by pick-up of both H_2O and N_2 from the background, resulting in assembly of $[Na(H_2O)_nN_2]^+$ clusters. Indeed, the lower intensity of this envelope relative to the $[Na(H_2O)_n]^+$ band correlates well with the relative abundances of ambient H_2O to N_2 in the pick-up chamber, ~9:1 as measured by EI mass spectrometry. The number of water molecules in these clusters, n = 8-11, also agrees with the relative abundances of H_2O and N_2. The possibility of a contribution from $[Na(H_2O)_nHe_7]^+$ cannot be ruled out, particularly since recent calculations show that the Na^+-He binding energy in Na^+He_N clusters begins to drop off above N = 6.[67] However, it seems very unlikely that the desolvation process should exclusively favor the attachment of exactly seven He atoms, when no other combinations are observed. The correlation of the masses, composition,

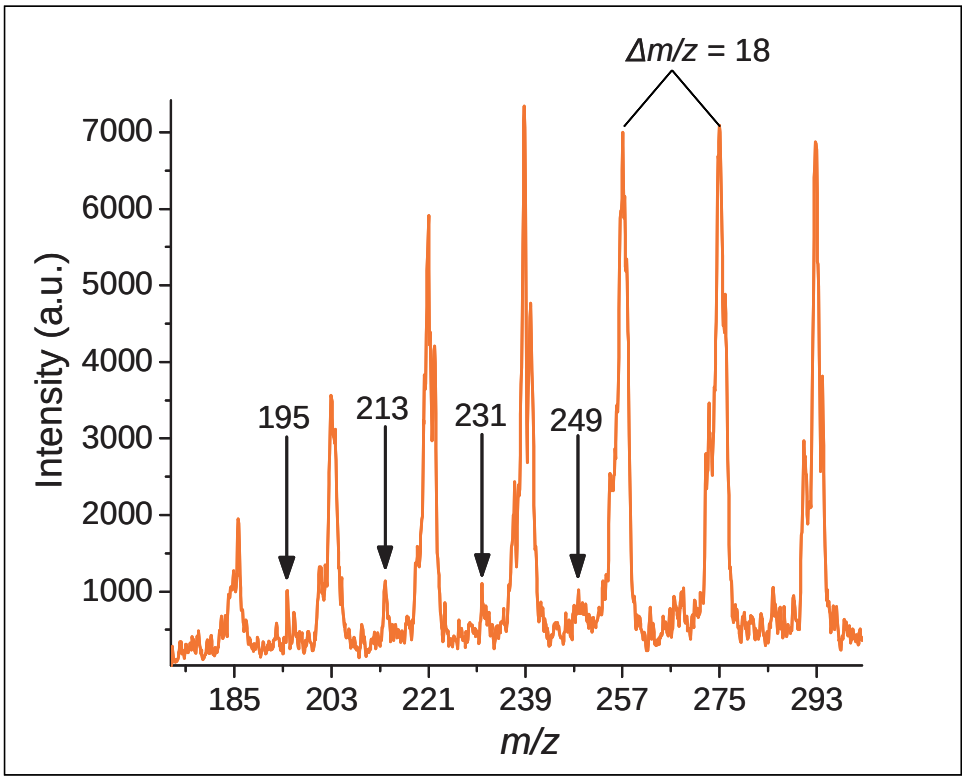

Figure 4.3 Zoomed-in view of *m/z* 173-301 from mass spectrum in Figure 4.2. Arrows indicate low intensity peaks corresponding to $[Na(H_2O)_nN_2]^+$ clusters.

and relative abundances of the observed ion clusters with the expected pick-up statistics suggests that the spectrum is at least qualitatively representative of the composition of the droplets before desolvation.

4.2.2 $[Na(H_2O)n(HCN)m]^+$ Clusters

Given that this experiment is limited to quite large droplets, the low chamber pressures required to avoid droplet contamination are difficult to achieve. However, in addition to the background impurities picked-up by the ion-doped droplets, other species can also be introduced for complexation with the embedded Na^+. Shown in Figure 4.4 is a mass spectrum collected with a small amount of HCN vapor added to the pick-up chamber. The pressure was such that, again assuming that the pick-up statistics are unchanged from neutral droplets, the droplets were most likely to capture one or two HCN molecules in addition to any background impurities.

The spectrum obtained with $HCN_{(g)}$ in the pick-up chamber consists of an envelope of peaks spaced by 9 Da (Fig. 4.4 inset), consistent with the masses of $[Na(H_2O)_n(HCN)_m]^+$ clusters. It is noted that under these conditions it is no longer possible to distinguish the low intensity envelope of peaks seen in Figure 4.3, since the resolution (FWHM = 3 Da) of the spectrum is insufficient to resolve them from the $[Na(H_2O)_n(HCN)_m]^+$ peaks. Although the pressure in the pick-up chamber was optimized to keep the number of captured HCN molecules small, uniquely assigning the identities of these cluster ions is not possible due to mass coincidences. For example, the peak at m/z = 275 may contain contributions from $[Na(H_2O)_{14}]^+$, $[Na(H_2O)_{11}(HCN)_2]^+$, or $[Na(H_2O)_8(HCN)_4]^+$, with the species containing 0 or 2 HCN molecules highest in abundance. Nevertheless, these results indicate that the sequential pick-up of dopant

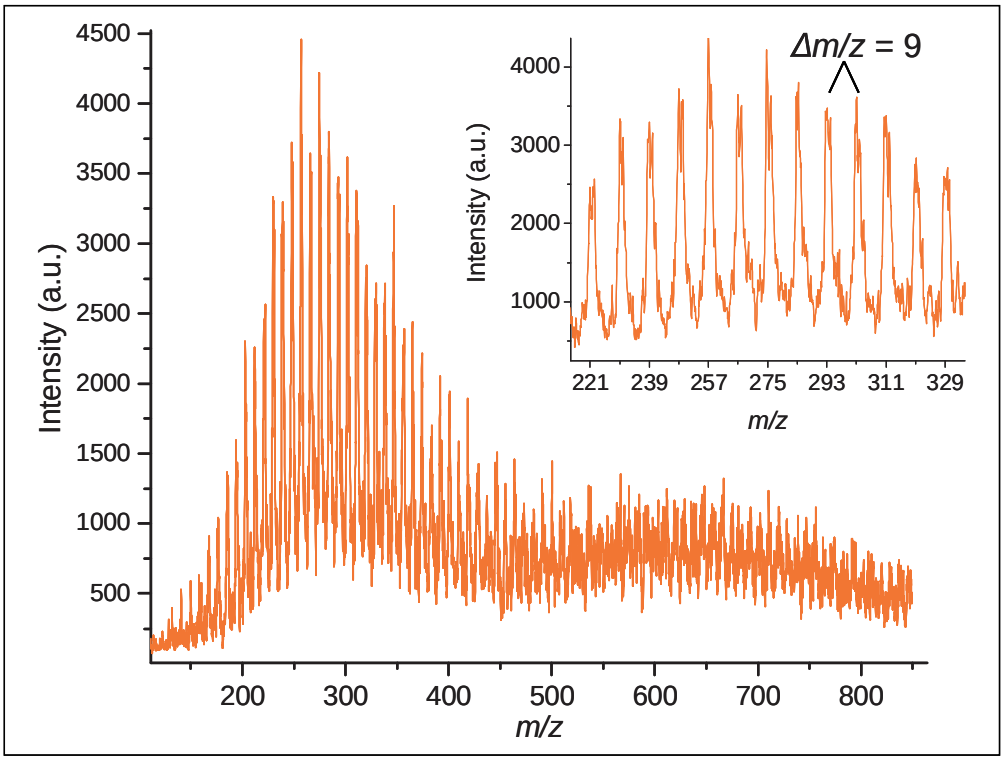

Figure 4.4 Mass spectrum of $[Na(H_2O)_n(HCN)_m]^+$ clusters formed in superfluid helium nanodroplets when $HCN_{(g)}$ added to pick-up chamber. Inset: zoomed-in view of *m/z* 215-335.

species typically used to assemble neutral clusters in helium droplets can analogously be used for ion-neutral complexes as well.

One of the most desirable abilities of the helium droplet method is that of forming tailor-made clusters in the droplet. From the above spectra it can be concluded that tailored cluster composition is not achievable when limited to large droplets at the experimental pressures. However, altering the pressure of HCN in the pick-up chamber should result in a change in the composition of clusters formed. Indeed, increasing the pressure of HCN in the pick-up chamber results in the formation of higher mass clusters, as can be seen in Figure 4.5. The pressure of HCN was not measured, so differences between the spectra can only be described qualitatively as resulting from either more or

less HCN present in the pick-up chamber. It should also be noted that the spectra in Figure 4.5 were obtained with tuning parameters that best exhibited the HCN pressure dependence. These tuning parameters were different from those shown in Figure 4.1, which resulted in spectra that are different in appearance than those in Figures 4.2-4.4 and are not directly comparable. Nevertheless, it can be determined from the spectra in Figure 4.5 that a limited degree of control over cluster composition is attainable at the droplet sizes studied. By extension, it can be concluded that tailored ion-neutral cluster formation in small droplets is possible in the same way that neutral cluster formation has been performed. Certainly, the capture of ions by smaller droplets is highly desirable. Considerable effort has been made in this direction and those studies will be described in the subsequent chapters.

4.3 Discussion

The fact that there are no helium "tails" on the ion-neutral cluster peaks implies that the desolvation process heats the droplet sufficiently to evaporate the helium atoms from the ion-neutral complex. On the other hand, the fact that the number of background impurities clustered with the Na^+ seems to reflect the pick-up statistics prior to evaporation suggests that the desolvation does not heat the ion-neutral cluster enough to drive off H_2O, N_2, or HCN. This behavior is particularly interesting in light of the observation that Na^+ in a helium droplet strongly binds the nearest helium atoms, forming a shell of solid helium, or snowball.[64,65,67] Since a snowball presumably forms around the Na^+ in these experiments, it is reasonable to suspect that during assembly of an ion-neutral cluster, the snowball might prevent impurity molecules from binding directly to the ion. Instead, they could be forced to coagulate around the existing

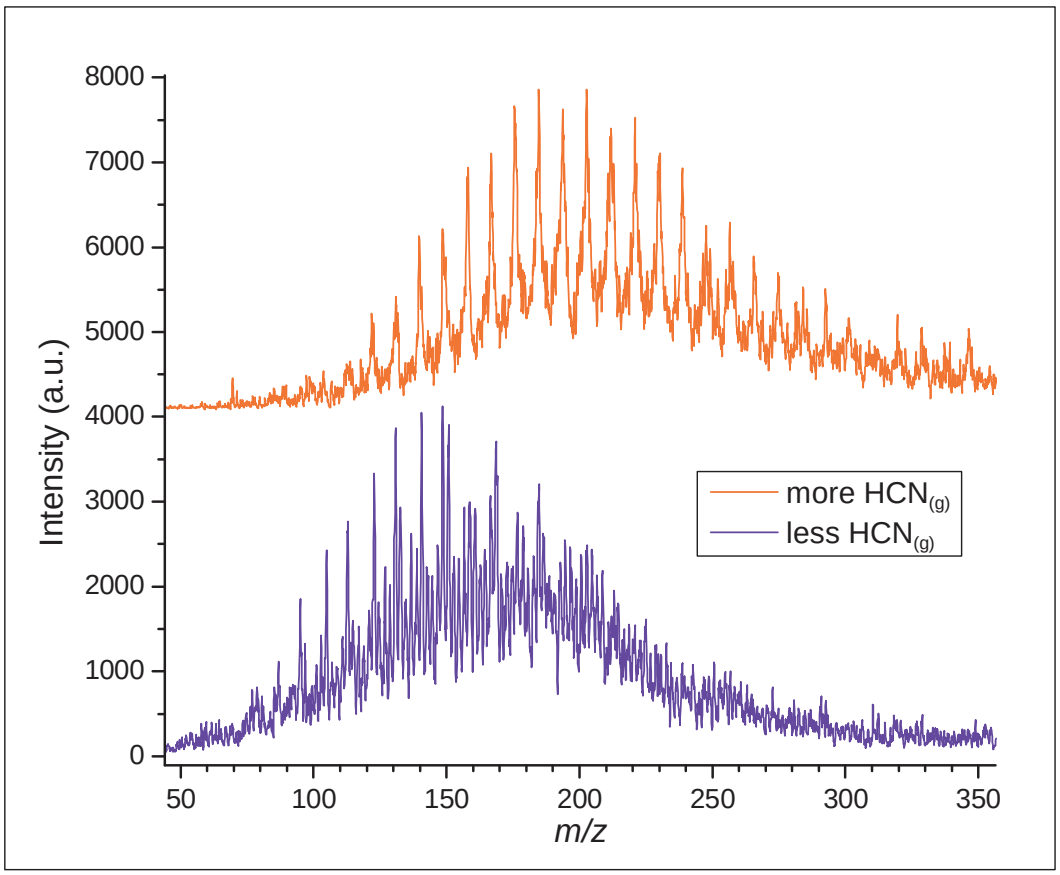

Figure 4.5 Mass spectra of $[Na(H_2O)_n(HCN)_m]^+$ clusters formed with different $HCN_{(g)}$ pressures in the pick-up chamber.

snowball. In contrast, the signals observed in the mass spectra correspond to ions without helium atoms (although a weak signal may be attributable to $[Na(H_2O)_nHe_7]^+$). Hence, either the neutral dopants are able to displace the helium atoms constituting the snowball during coagulation, or the cluster rearranges during desolvation so that the helium atoms of the snowball can be evaporated.

To displace the helium atoms in the snowball, the Na^+-impurity interaction must be stronger than the interaction of the ion with the surrounding helium atoms. To explore this issue, the binding energies of He, H_2O, N_2, and HCN with Na^+ have been calculated at the MP2/6-311++G(3df,3pd) level of theory using the Gaussian 03 suite of

programs.[83] The respective binding energy calculated for each system is listed in Table 4.1, along with the dipole moment and isotropic polarizability of each cluster partner. The calculated Na^+-He binding energy (263 cm^{-1}) is somewhat smaller than that obtained at higher levels of theory (331 cm^{-1}).[67] Nevertheless, it is clear that the binding energy of Na^+ to N_2, H_2O, or HCN is at least a factor of 10 greater than to a helium atom. For N_2, the stronger binding is likely related to the fact that N_2 is more polarizable than helium. In the case of H_2O or HCN, these molecules also are more polarizable than He, but have strong permanent dipole moments as well. Accordingly, it is calculated that the binding of Na^+ to these molecules is yet stronger. For H_2O, the interaction with Na^+ is calculated to be approximately 30 times stronger than the Na^+-He interaction. In light of the large difference in binding energies for N_2, H_2O, and HCN versus that for He, it seems reasonable to expect that incoming impurities could displace helium atoms in the snowball to interact directly with the embedded Na^+ ion.

Although the binding energies of Na^+ with the molecules studied are greater than with helium, displacement of the helium snowball is not guaranteed. The temperature of

Table 4.1 Binding energies of various neutral molecules to Na^+ calculated using MP2 level of theory and 6-311++G(3df,3pd) basis set.

Neutral molecule	Dipole moment (D)[a]	Polarizability ($Å^3$)[a]	Calculated binding energy to Na^+ (cm^{-1})	Experimental binding energy to Na^+ (cm^{-1})[b]
He	-	0.208	263	
N_2	-	1.710	2649	2868
H_2O	1.85	1.501	7954	8569
HCN	2.98	2.494	8726	

a) Values taken from NIST database;[84] all are experimental, except the polarizablity of HCN.
b) Values from Castleman et al.[85]

the droplet is 0.37 K and the rate of cooling is such that the Na^+-snowball cluster and incoming neutral molecule are both cold upon complexation. At this temperature, the thermal energy available to drive a reaction is extremely low. Thus, for a neutral molecule to bind directly to the Na^+, insertion of the neutral molecule must be nearly barrierless. To determine if barrierless insertion of these neutral molecules through the helium snowball is possible, additional ab initio calculations were performed.

Briefly, the calculations were performed as follows. A shell of nine helium atoms was placed around the sodium cation, as one group has reported this as the required number of atoms to complete the first solvation shell.[65] The geometry of the $[NaHe_9]^+$ cluster was then optimized to its lowest energy structure. A water or nitrogen molecule was placed at a distance from the $[NaHe_9]^+$ cluster such that the total energy of the system approximated that for infinite separation. That is, the initial position of the water or nitrogen molecule was such that displacement of the helium snowball was not forced to occur. The geometry of these systems was then optimized to its lowest energy structure. The results of this type of calculation for $[NaHe_9]^+ \cdot H_2O$ are shown in Figure 4.6.

The initial geometry of the $[NaHe_9]^+ \cdot H_2O$ cluster (top of Fig. 4.6) was defined as having 0 cm^{-1} of energy. The energies associated with subsequent geometries of the cluster relative to the energy of the initial cluster geometry are plotted in Figure 4.6. Clearly, the geometry at each step of the calculation is at a lower energy than the initial geometry, finally achieving an arrangement with the electronegative oxygen atom of the water molecule interacting directly with the sodium cation (lower-right of Fig. 4.6). It can be seen that the final state is approximately 600 cm^{-1} lower in energy than the initial

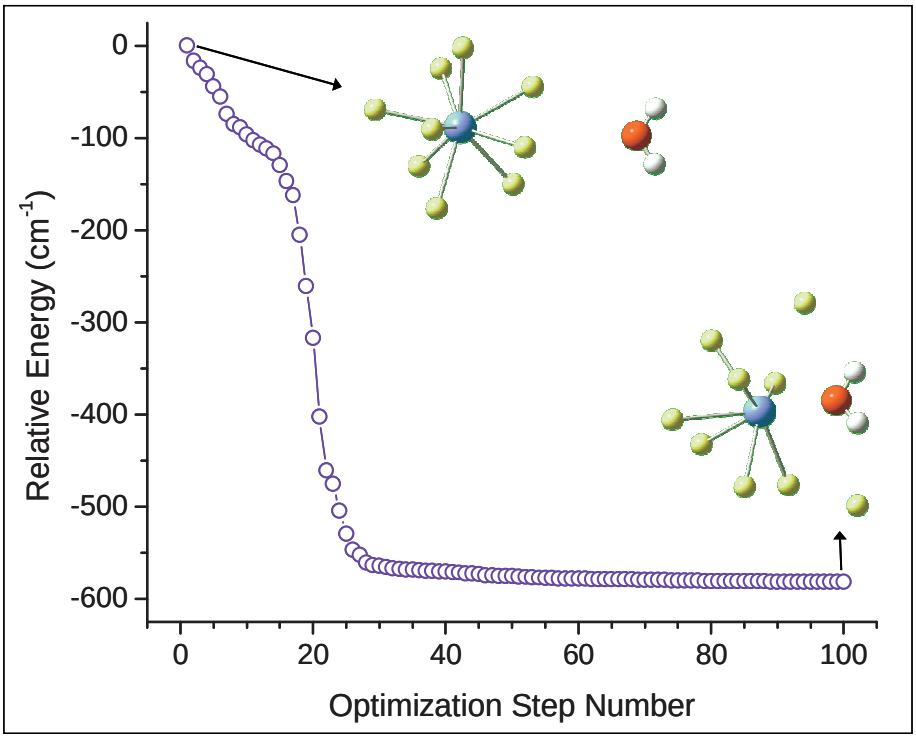

Figure 4.6 Optimization of $[NaHe_9]^+ \cdot H_2O$ geometry. Na^+, blue; He, yellow; O, red; and H, white. The Na^+-He "bonds" are drawn for clarity and do not represent covalent bonds.

system was maintained at 0 K, that is, there is no energy put into the system. Therefore, the result of the geometry optimization is taken to be representative of what occurs in a helium droplet at 0.37 K. The results indicate that there is at least one barrierless pathway for a water molecule to insert into the helium snowball. Results of an analogous calculation for N_2 are shown in Figure 4.7. Again, the results indicate the existence of at least one barrierless pathway for the insertion of a nitrogen molecule into the helium snowball surrounding Na^+. The results of these calculations suggest that the ion-neutral clusters observed in the mass spectra are formed in the droplets before desolvation.

The above results have shown that helium droplets can be doped with Na^+ ions, and that the pick-up processes associated with neutral droplets can also be used to assemble complexes in ion-doped droplets. Furthermore, these results have suggested

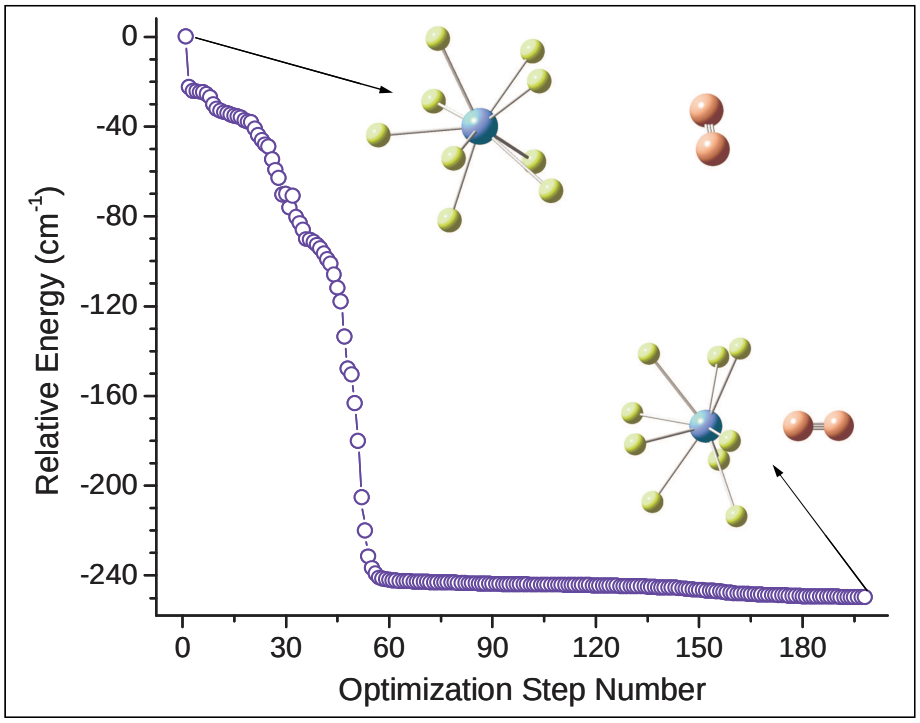

Figure 4.7 $[NaHe_9]^+ \cdot N_2$ geometry optimization. Na^+, blue; He, yellow; and N, pink. The Na^+-He "bonds" are drawn for clarity and do not represent covalent bonds.

that the desolvation process does not heat the ion-neutral cluster sufficiently to cause dissociation to small, thermodynamically stable clusters ($n \leq 6$). Consequently, these results can be used to generate a fit to the distribution of ions seen in Figure 4.2. Maintaining the assumption that the Poisson pick-up statistics are unchanged from neutral droplets, the background pressure of the vacuum chamber can be used to calculate the probability that a droplet of a given size will encounter precisely n water molecules. The pick-up statistics must then be averaged over the distribution of droplet sizes in the beam to calculate the probability of assembling each $[Na(H_2O)_n]^+$ cluster, which is the occupancy probability, P_{occ}, described in Section 3.3. It is then assumed that the distribution of ion-neutral clusters is unchanged by the desolvation process, that is, that no dissociation of the ion-neutral clusters occurs.

As mentioned above, the distribution of droplet sizes produced by helium expansion close to the critical point is not well characterized, although the mean size has been measured as $>10^5$ atoms/droplet.[72] At higher temperatures, where droplets form by condensation of helium gas,[69] the distribution is known to be log-normal.[73] At lower temperatures, droplets are formed by fragmentation of a liquid jet, and the distribution is a linear-exponential.[71,75] Regardless of which of these is used to generate a fit, there are two adjustable parameters, namely the mean droplet size, $\overline{N}$, and the minimum droplet size required to reach the mass spectrometer, N_{min}. The latter parameter simply cuts-off the distribution below the critical size. Plotted in Figure 4.8 is the distribution of $[Na(H_2O)_n]^+$ ions observed in Figure 4.2, along with the best fits to the data for both log-normal and linear-exponential droplet size distributions. The details of this calculation can be found in Appendix B. In either case, the best fit is produced assuming a mean droplet size of 3.0×10^5 He atoms and a cut-off of 9.0×10^5 He atoms. The value used for mean droplet size was based on previous estimates at similar expansion conditions and a SIMION calculation that had estimated a minimum droplet size of $\sim 10^6$ atoms for reaching the mass spectrometer. The fact that the fit is insensitive to the functional form of the droplet size distribution is simply because the cut-off threshold is much larger than the mean. Hence, only the tail of the respective distributions, which exhibit similar behavior for each, is being sampled in this experiment.

While the fit reproduces the data well from n = 5-20, it deviates at high n. There are several possible explanations for this behavior. It may be caused by differences in the trajectories of ion-doped droplets of differing sizes inside the desolvation region. Since

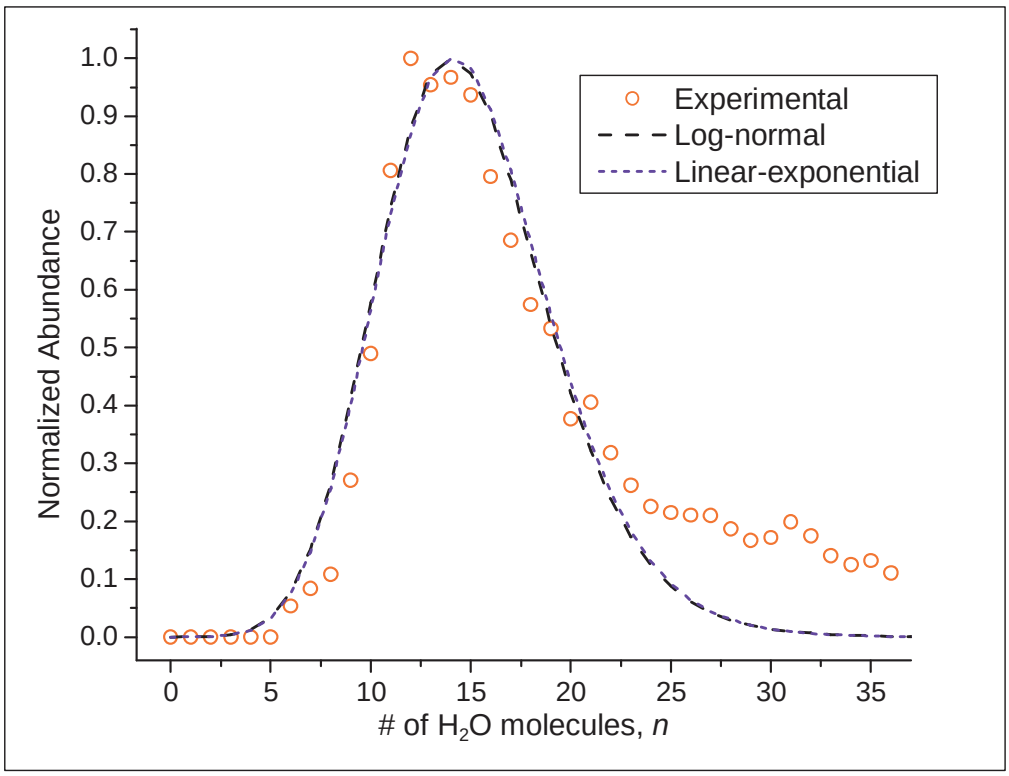

Figure 4.8 Normalized abundance of $[Na(H_2O)_n]^+$ clusters vs n. Open circles: experimental intensities; dashed curve: log-normal P_{occ} for $\overline{N} = 3.0 \times 10^5$ He atoms and $N_{min} = 9.0 \times 10^5$ He atoms; dotted curve: linear-exponential P_{occ} for $\overline{N} = 3.0 \times 10^5$ He atoms and $N_{min} = 9.0 \times 10^5$ He atoms.

the trajectories of smaller droplets would be expected to diverge from those of larger ones, this might produce a weighting factor that favors detection of ions desolvated from larger droplets (and hence a greater number of impurity pick-ups). Alternatively, the observed deviations could be due to the dissociation of larger ion-neutral complexes into smaller ones upon desolvation. In this case, the unexpected intensity at high n would be due to large complexes that did not dissociate, and the maximum in the distribution would have been shifted to lower n by complexes that did dissociate. However, the presence of N_2-containing clusters suggests that cluster composition is not significantly altered during the desolvation process. As shown in Table 4.1, the binding energy of N_2

to Na^+ is roughly three times weaker than that of H_2O, ~2650 cm^{-1} vs ~7950 cm^{-1}. Due to the statistical nature of the pick-up process and the ratio of H_2O:N_2 in the chamber and the ion-neutral clusters, it is probable that the N_2 of the $[Na(H_2O)_nN_2]^+$ cluster is bound to water molecules instead of directly to Na^+. The binding energy of N_2 to H_2O has been calculated to be only 441 cm^{-1}.[86] Such a weakly bound species would require little perturbation to cause dissociation. As discussed in Section 4.2.1, the ratios of N_2:H_2O in the clusters and the relative intensities of the $[Na(H_2O)_nN_2]^+$ and $[Na(H_2O)_n]^+$ peaks suggest that these clusters are not dissociating. Therefore, it is suspected that the discrepancy in the fit to the data at high *n* is not due to dissociation of clusters.

It is expected that a significant number of He atoms are evaporated during the capture of the Na^+ ion and so the mean droplet size before capture is likely substantially larger than afterward. Since droplet size distributions with larger mean sizes are also broader,[71,73,75] simply using the log-normal (or linear-exponential) distribution with a mean corresponding to the post-pickup size will produce a curve that is too narrow. This is entirely consistent with what is seen in Figure 4.8. If another adjustable parameter is introduced to allow the width of the distribution to increase independent of its mean, the fit could be improved since the cut-off value allows the fit to broaden preferentially on the high-*n* side. However, there are several reasons for hesitating to do so in the present discussion. Primarily, the pre-pickup droplet size distribution is not well-characterized under these conditions.[72] Also, the Na^+ capture dynamics are not sufficiently understood to predict the number of helium atoms evaporated from the droplet. Indeed, ions created inside helium droplets have exhibited a complex, highly non-linear cooling process (Section 2.2.2).[56,57] Given these constraints, attempts to make a more detailed

fit at the present time would be speculative. In any event, the ion capture process is of significance and is investigated in the next chapter.

4.4 Conclusions

The capture and solvation of externally generated Na^+ ions by superfluid helium droplets has been demonstrated. It was shown that after ion-doping, the pick-up processes normally associated with uncharged droplets can be used to assemble ion-neutral clusters inside the droplet. Using a novel desolvation technique, $[Na(H_2O)_n]^+$, $[Na(H_2O)_nN_2]^+$, and $[Na(H_2O)_n(HCN)_m]^+$ complexes assembled inside the droplets have been observed. The results suggest that the snowball of solid helium that presumably forms around the captured Na^+ ion does not prevent subsequently captured species from binding to the cation. This conclusion has been reinforced by ab initio calculations demonstrating barrierless insertion of H_2O and N_2 into the helium snowball.

These preliminary studies open the door to many interesting avenues of research. Sodium has a very low ionization potential: 5.14 eV.[50] Low ionization potential allows for cluster formation with neutral molecules without undergoing charge transfer, thus avoiding fragmentation. Preventing fragmentation could be useful in applications in which only a single mass spectral peak per analyte is desired. Furthermore, because helium droplets can pick-up any gas phase molecule, many molecules might be ionized with equal efficiency by complexation with Na^+, effectively avoiding differences in ionization cross-section associated with other methods. Uniform ionization efficiency would set the current method apart from techniques such as lithium ion attachment mass spectrometry, for which ionization efficiency depends on Li^+ affinity of the neutral molecule.[87]

Ion-neutral clusters solvated in helium droplets could also be studied with IR spectroscopy, which would be expected to exhibit better resolution than previously achieved in the gas phase due to the very low temperature of the droplets (see Section 1.6). Of course, these pursuits require control over the composition of the clusters in question, which requires the use of small droplets ($\overline{N} < 5000$ He atoms). The current results were obtained using droplets estimated to consist of ~10^6 He atoms, which are large enough to pick-up many background impurities. Examination of the ion capture process using lower energy ions and smaller droplets are the topic of the next chapter.

CHAPTER 5

STUDY OF ION CAPTURE PROCESS

In Chapter 4, the ability of superfluid helium nanodroplets to capture high-energy sodium cations was demonstrated. The formation of ion-neutral clusters within helium droplets was also demonstrated. Unfortunately, the study was experimentally limited to very large droplet sizes, $N > 10^6$ He atoms. The large cross-sections of such droplets prevented fine control over the ion-neutral composition at experimentally accessible pressures. The large droplet sizes also limited the insight that could be gained into the ion capture process. This chapter discusses experiments that utilized lower energy sodium and lithium cations and smaller droplets. Specifically, the size distributions of droplets that were produced at Regime I conditions were measured after capture of an ion. Since the neutral droplet size distributions produced in Regime I expansions have been well characterized, comparison of the ion-doped size distribution to the neutral size distribution provides information regarding the ion capture process. The measured distribution of ion-doped droplet sizes was found to depend on nozzle temperature, ion kinetic energy, and ion mass. The ion-doped distributions can be fit to a log-normal function, however, the maximum in the ion-doped distributions occurs at much larger values of N than for the neutral distributions, and there appears to be a non-zero minimum droplet size necessary for ion capture. These results are discussed in

terms of previous studies of cooling by helium droplets and possible ion capture mechanisms are contemplated.

5.1 Experimental

5.1.1 Charge-Steering Apparatus

The instrument used for these studies was the same as for those of Chapter 4, with additional ion manipulation capabilities, as described below. The nozzle conditions implemented in this work were p_0 = 50 bar and T_0 = 12.0-16.0 K. Again, after being skimmed, the droplet beam was modulated by a chopper for use in a phase-sensitive detection scheme. For the experiments described herein, the pressure of the pick-up chamber in the absence of the helium droplet beam was maintained below 3.0×10^{-7} torr.

The ion source was identical to that used in Chapter 4, which was described in detail in Section 3.3.2. Briefly, the source consisted of an enriched zeolite paste coated onto a coiled tungsten filament that emits alkali cations upon heating. The current used to heat the filament was kept constant throughout. Therefore, the temperature of the filament, and hence ion emission, was approximately constant. The coated filament was oriented vertically in the vacuum chamber on one side of the helium droplet beam (Fig. 5.1). On the other side of the droplet beam, opposite the filament, was a vertically-oriented, cylindrical, collector electrode. The collector electrode was biased at a negative potential, which focused the alkali cations in the region of the droplet beam and defined their kinetic energy. This collector electrode was also used to monitor the ion current, which increased as the potential applied to the collector electrode was changed to increasingly negative values. However, due to the increased velocities of higher kinetic

energy ions, the number density of ions in the pick-up region remained approximately constant, ~5×10^4 ions/cm^3.

A custom charge-steering apparatus (Fig. 5.1) was used for the determination of ion-doped droplet size distributions, similar in principle to that used in previously published work by Fárník et al.[48] Applying a positive dc potential to a steering electrode alters the trajectories of positively-charged droplets. In this experiment, droplets of different sizes were deflected to various distances from the neutral droplet beam axis, with smaller droplets steered farther off-axis than larger ones. Therefore, placing a detector at a fixed distance from the beam axis and ramping the dc potential applied to the steering electrode allowed for the separation of charged droplets based on size. The charge-steering apparatus consisted of two vertical, cylindrical, stainless steel electrodes, which were located on opposite sides of the droplet beam. The electrode on the same side of the beam as the collector electrode was held at ground. A positive potential was applied to the electrode on the same side of the beam as the filament, referred to as the steering electrode. The steering electrode was located between two ground shields, which were parallel, stainless steel plates orthogonal to, and centered upon, the helium droplet beam. Each plate had a circular aperture that was covered with 88% transmission nickel mesh to allow droplets to pass through while minimizing stray fields from the steering electrode that may have affected the ion-doping region.

Detection of charged droplets was accomplished with an electron multiplier downstream of the ion-doping region and charge-steering apparatus. It was held in a grounded housing with a 2.0 mm-wide entrance slit covered with 88% transmission nickel mesh. The output of the electron multiplier was measured with a lock-in amplifier

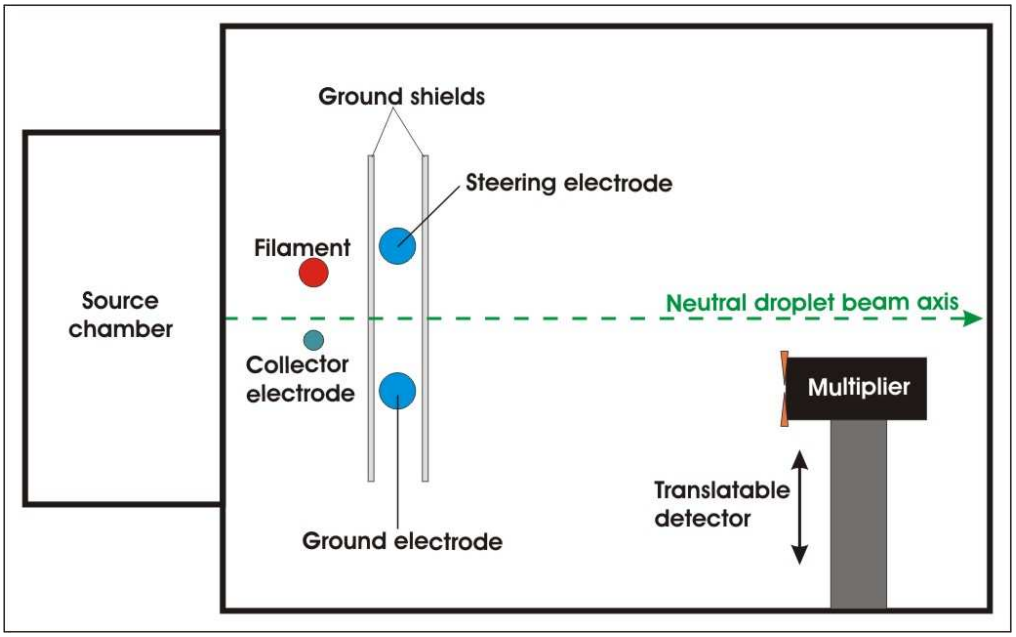

Figure 5.1 Top-down view of the apparatus for ion-doping and charged droplet steering.

for phase-sensitive detection. This detection scheme removed any contribution from stray ions that were not picked-up by helium droplets. The detector could be translated orthogonally to the droplet beam. For the results discussed here, the detector was positioned 0, 5, or 10 mm from the axis. As described below, the position of the detector, in combination with the collector and steering electrode potentials, determined the sizes of droplets that could be measured.

For determination of ion-doped droplet size distributions, signal from the detector was measured as a function of the steering electrode potential. The potential applied to the steering electrode was ramped from 0 to 2000 V at the rate of 2.0 V/s. This was done twice for each nozzle temperature, collector electrode potential, and detector position. These steps resulted in two intensity vs voltage curves for each combination of parameters, which were averaged and converted into intensity vs droplet size curves to

yield droplet size distributions. The conversion from voltage to droplet size was accomplished by convolution with simulated ion-doped droplet trajectories. The simulations are discussed below. The details of the voltage-to-droplet size conversion process are discussed in more detail in Appendix C.

5.1.2 Simulation of Ion-Doped Droplet Trajectories

The effect of the charge-steering apparatus on the trajectories of ion-doped droplets was modeled with SIMION[80] by a 1500 × 500 × 1 potential array with scaling of 0.1 mm per grid unit (Fig. 5.2). The filament and all electrodes were modeled by solid electrodes, while the shields and detector entrance were modeled as ideal grids, which are surfaces that exhibit 100% ion transmission and no field leakage. The ion-doped droplet trajectories started at an x-position aligned with the centers of the filament and collector electrode and at a y-position aligned with the axis of the neutral helium droplet beam (Fig. 5.2). The model droplets were assigned a mass, a charge of +1, and a kinetic energy in the x-direction that was determined by the droplet mass and velocity. Droplet velocity is a function of p_0 and T_0 and was estimated from previous work.[69,88] Implicit in this description is the fact that the model simulated only the trajectory of a droplet that had already captured an alkali cation; it did not simulate the pick-up process.

Simulation parameters were varied in a grid-like fashion. For a given droplet velocity, collector electrode potential, and potential applied to the steering electrode, the trajectories of ion-doped droplets of six different sizes, ranging from 200,000 to 2,000,000 He atoms, were simulated. This simulation was then repeated for increased potentials applied to the steering electrode, in steps of 200 V from 0 to 2000 V, while

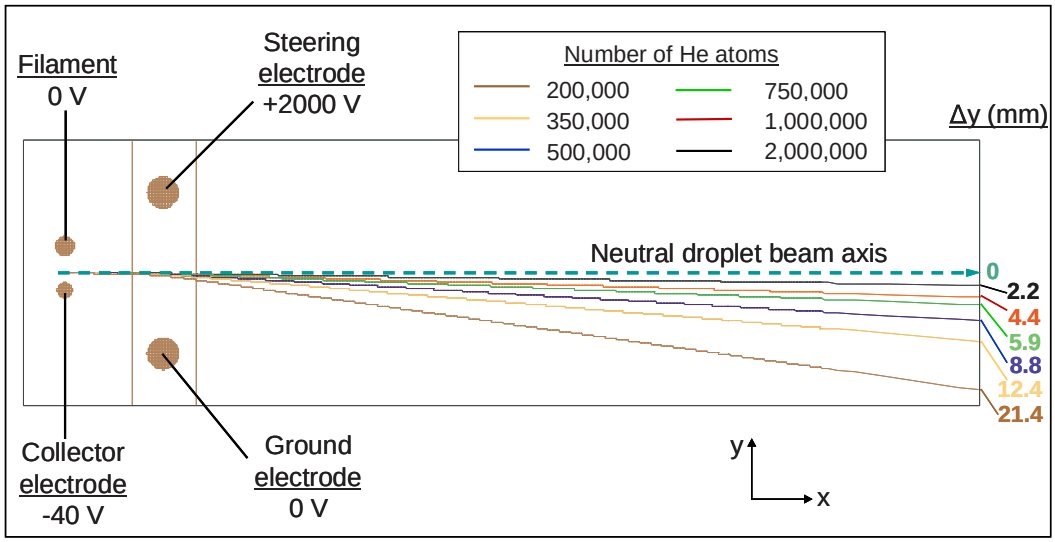

Figure 5.2 SIMION model and simulated trajectories of ion-doped droplets of various sizes with velocities corresponding to T_0 = 14.0 K; collector electrode potential = -40 V, steering electrode potential = +2000 V.

maintaining droplet velocity and collector electrode potential. The above steps were then repeated with the same droplet velocity, but at 10 V steps in collector electrode potential (-10 to -50 V). Finally, all of the aforementioned steps were repeated for the droplet velocities used, as determined by T_0, to experimentally measure ion-doped droplet size distributions. These simulations resulted in grids of droplet size and position data as a function of potential applied to the steering electrode. Interpolation of the calculated values was used to obtain the same data for other collector electrode potentials. These values were then used to convert the experimental steering electrode potentials to droplet sizes for a given nozzle temperature, collector electrode potential, and detector position.

An example of simulated ion-doped droplet trajectories is shown in Figure 5.2. In this example, the droplet velocities correspond to T_0 = 14.0 K, the collector electrode was at -40 V, and the steering electrode was at 2000 V, the maximum value used experimentally. Since this simulation was performed with the maximum steering

electrode potential, it was used to determine the maximum distance that a given droplet size can be deflected for the given collector electrode potential and nozzle temperature. If the detector is positioned 5 or 10 mm from the neutral droplet beam axis, the largest droplets that can be steered into the detector are approximately 7.5×10^5 or 4.0×10^5 He atoms, respectively, when the collector electrode is held at -40 V.

Conversely, from a simulation performed with the steering electrode at 0 V, the smallest droplets able to be detected at a given collector electrode potential and nozzle temperature can be determined. For a -40 V collector electrode and T_0 = 14.0 K, the smallest detectable droplet sizes are 160,000 and 80,000 He atoms for detector positions of 5 and 10 mm off-axis, respectively. The smallest detectable droplet sizes are so large due to the fact that the potential well created by the collector electrode serves to steer smaller ion-doped droplets farther off-axis than the detector is positioned. Certainly, reducing the magnitude of the collector electrode potential allows for smaller droplets to be detected. Therefore, the collector electrode potential, detector position, and steering electrode potential range combined to determine the size of droplets that were able to be detected for a given nozzle temperature.

5.2 Results and Discussion

5.2.1 Detector On-Axis

Ion-doped droplet signal resulting from Na^+ capture was first measured without a potential applied to the steering electrode, with the detector centered on the neutral droplet beam axis. In Figure 5.3, the signal is plotted as a function of T_0 for three different collector electrode potentials: -15, -30, and -45 V. The collector electrode potentials defined the kinetic energies of the sodium cations at the point they crossed the

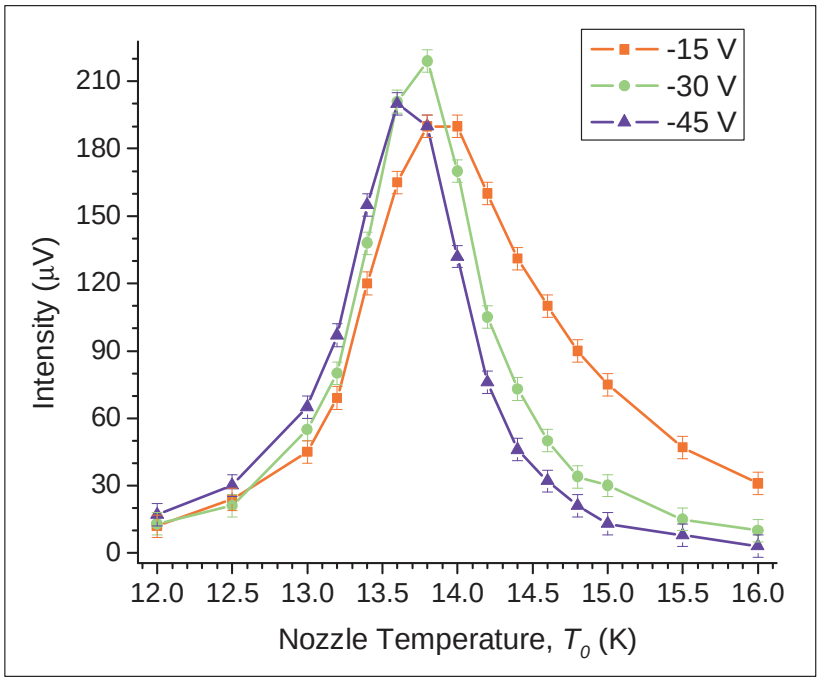

Figure 5.3 Charged droplet signal vs nozzle temperature for various collector electrode potentials (detector on-axis): squares, -15 V; circles, -30 V; and triangles, -45 V.

droplet beam path to be slightly less than 15, 30, and 45 eV, respectively. Subsequent discussion will refer to ions of 15, 30, or 45 eV of kinetic energy for simplicity, but the kinetic energy at the point of impact with a droplet is slightly less than these values. For collisions of alkali cations with noble gases, the height of the potential at the critical interatomic distance, at which electronic excitations can occur, is 40-65 eV.[89] Therefore, the probability of ionization of helium droplets by collision with Na^+ is expected to be negligible at the kinetic energies studied. In fact, 15 eV is well below the first ionization potential of He (24.59 eV).[50] Further, helium droplets have been shown to capture Na^+ at 200 eV kinetic energy (Chapter 4). Hence, it is assumed that the signals measured were due to helium droplets that captured a sodium cation.

As can be seen in Figure 5.3, the signal exhibited a strong dependence on nozzle temperature for all collector electrode potentials. A consistent terminology will be used throughout when referring to relative collector electrode potentials, in which going to increasingly negative voltages (e.g. from -15 V to -30 V) will be referred to as increasing the potential since related properties, such as electric field strength and ion kinetic energy, increase as well. Signal greater than the noise could not be measured below T_0 = 12.0 K or above T_0 = 16.0 K, except for perhaps -15 V (noise is depicted by the error bars in Fig. 5.3). Increasing the potential applied to the collector electrode resulted in a decrease in signal at the warmer nozzle temperatures. The temperature at which maximum signal was obtained decreases from 14.0 K for -15 V to 13.6 K for -45 V. The shift in signal maximum to colder nozzle temperatures, or to larger droplets, with increasing collector electrode potential has two possible causes. The higher the kinetic energy of an ion, the greater is the amount of energy that must be dissipated by the droplet to capture that ion. Depending on the mechanism by which the droplets dissipate the kinetic energy of the ion, it is likely that a larger droplet is necessary to capture an ion with higher kinetic energy. If this is true, then it would be expected that the signal at warmer nozzle temperatures decreased as the potential applied to the collector electrode increased. However, with the detector positioned on-axis, the effect of ion kinetic energy cannot be decoupled from the effect of the collector electrode potential on the trajectory of a charged droplet. As described above, the potential well created by the bias on the collector electrode steers charged droplets away from the neutral beam axis. Greater potentials steer the droplets further off-axis. Therefore, as the collector electrode potential is increased, the droplet size required to reach the detector is increased. Thus,

the observed decrease in signal at warmer nozzle temperatures, or smaller droplets, with increasing collector electrode potential could be unrelated to the ion kinetic energy and simply be an artifact of the charge-steering caused by the collector electrode. Nevertheless, the results suggest that an ample flux of low-energy ions in a low-field region should lead to capture by smaller droplets.

5.2.2 Detector Off-Axis

To decouple the effect of the collector electrode potential from the effect of ion kinetic energy, the charge-steering apparatus was used to measure the distribution of droplet sizes resulting from the capture of Na^+. Shown in Figure 5.4a are normalized droplet size distributions measured at T_0 = 14.0 K and collector electrode potential of -15 V. This figure serves as an example of the differences in observable droplet sizes at different detector positions. Positioning the detector closer to the neutral beam axis allowed for detection of larger droplets compared to the range accessible when the detector was farther off-axis. Furthermore, it can be seen that changing the detector position did not significantly alter the droplet size distribution measured, which is to be expected since the position of the detector should not have affected the capture of ions by droplets or the subsequent trajectories of ion-doped droplets. However, a slight difference between the two measurements is noticeable at larger droplet sizes. This difference arises from the finite slit width (2.0 mm) at the entrance to the detector, which allows a range of droplet sizes to reach the detector at a given steering electrode potential. The precision in droplet size measurement due to the slit width was calculated to be ±21% at a detector position 5 mm off-axis and ±10% at 10 mm off-axis. The determination of these values is described in Appendix C.

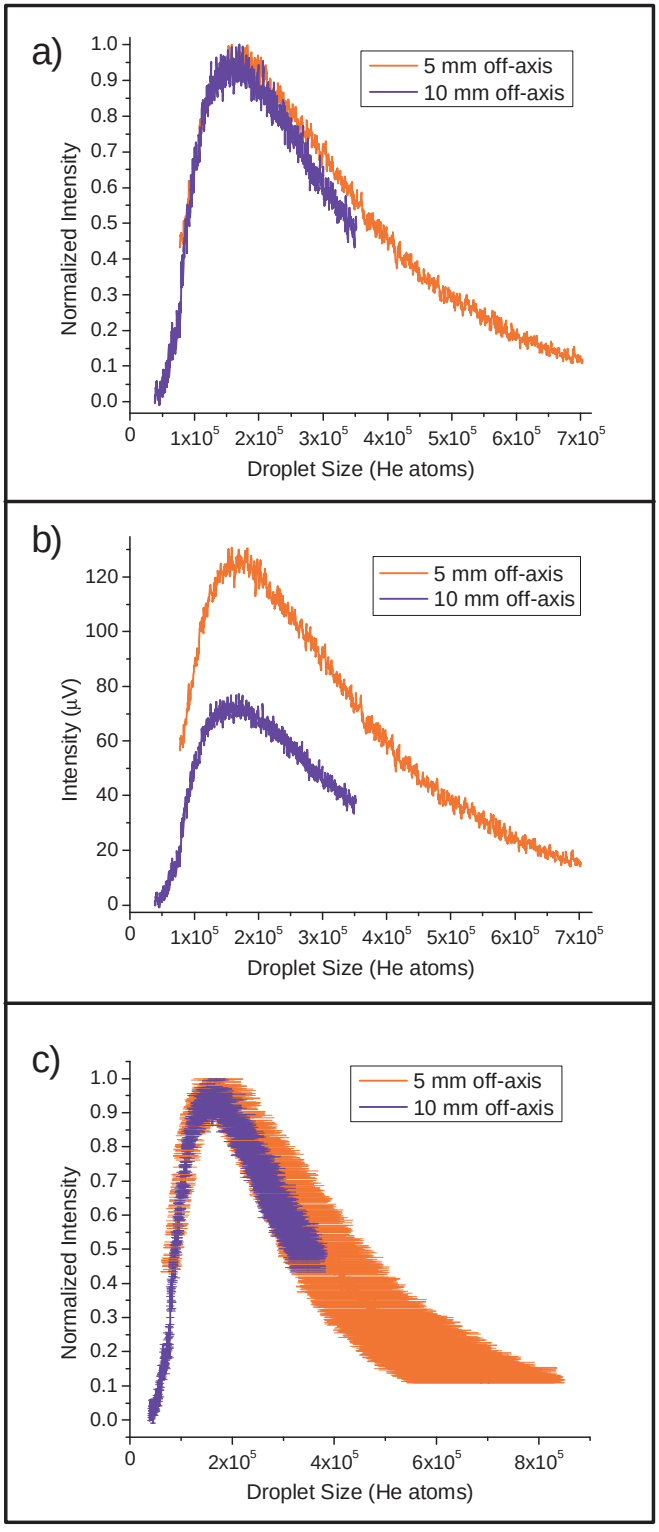

Figure 5.4 Na^+-doped droplet size distributions measured with detector positioned 5 mm (red) and 10 mm (blue) off-axis. Collector electrode = -15 V, T_0 = 14.0 K. (a) Normalized distributions; (b) measured distributions without normalization; (c) normalized distributions with droplet size precision superimposed.

The manifestation of the slit width on the measured distributions is shown in Figures 5.4b and c. In Figure 5.4b, the measured distributions are shown without normalization. In Figure 5.4c, the precision of the measurement has been superimposed on the droplet size distributions from Figure 5.4a. As can be seen in Figure 5.4c, the less precise measurement at 5 mm off-axis resulted in a wider range of droplet sizes detected compared to 10 mm off-axis. A broader range of detected droplet sizes means that a greater number of droplets reach the detector at any given time, resulting in greater signal. The result of greater signal at a detector position of 5 mm can be seen in Figure 5.4b, in which the intensity of the distribution measured at 10 mm off-axis is about half that measured at 5 mm. Due to the broader range of droplet sizes measured when the detector was closer to the axis, as the potential ramp was applied to the steering electrode, the signal changed more slowly for the distribution measured with the detector 5 mm off-axis. Accounting for the margin of error in droplet size measurement, it can be seen in Figure 5.4c that the distributions measured at different detector positions are experimentally equivalent.

5.2.3 Nozzle Temperature Dependence

The first factor studied in the capture of ions by helium droplets was nozzle temperature. Shown in Figures 5.5a and b are the measured size distributions for droplets doped with Na^+ at a collector electrode potential of -15 V. Distributions were measured for T_0 = 13.0, 14.0, 15.0, and 16.0 K. The most striking feature in Figure 5.5a is the similar shape of the observed distributions for $T_0 \geq 14.0$ K. The observed distribution for T_0 = 13.0 K exhibits no similarity to the others.

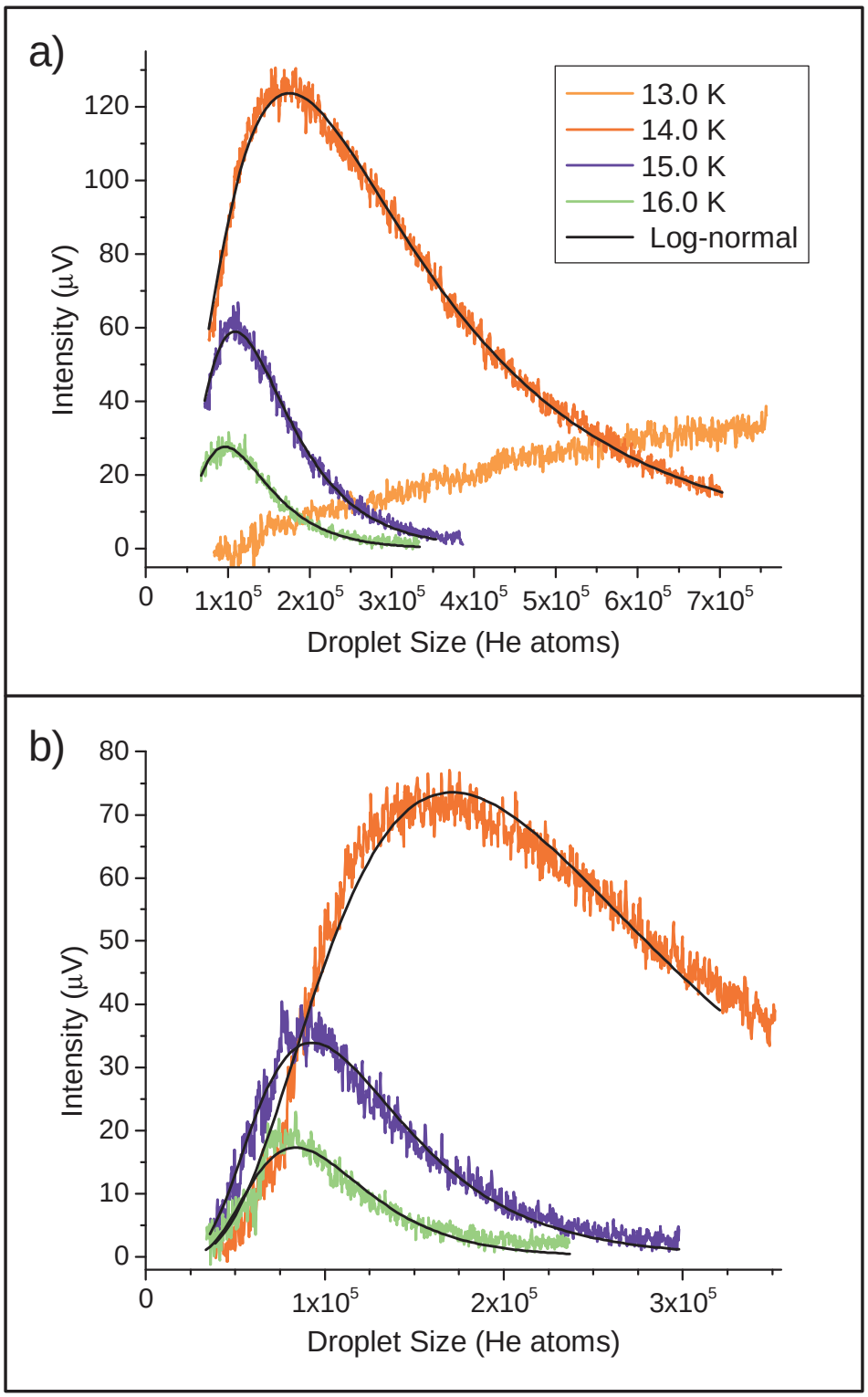

Figure 5.5 Droplet size distributions measured at various nozzle temperatures for capture of Na^+ with collector-electrode potential of -15 V. Detector positioned 5 mm off-axis (a) and 10 mm off-axis (b).

At a helium pressure of 50 bar, nozzle temperatures ≥14 K result in Regime I expansions, for which the mean droplet size, $\overline{N}$, can be calculated by published scaling laws.[70] For T_0 = 14.0 K, 15.0 K, and 16.0 K, the mean droplet sizes are 1.65×10^4, 1.26×10^4, and 9.68×10^3 He atoms, respectively (Fig. 3.2). The neutral droplet size distributions produced at these conditions are described by the log-normal function (Eq. 3.8) and were plotted in Figure 3.3. At p_0 = 50 bar, a nozzle temperature of 13.0 K corresponds to Regime II expansion. Droplet formation is this regime is thought to occur through a combination of Regime I and III mechanisms.[69,72] As mentioned in Section 3.2, the droplet sizes resulting from Regime II expansions have been estimated be $>10^5$ He atoms, but a quantitative description of the distribution of droplet sizes produced at these conditions has yet to be determined.

The distributions in Figure 5.5a that exhibit similar behavior, T_0 = 14.0, 15.0, and 16.0 K, are the result of ion capture by droplets formed in Regime I. The increase in intensity observed with decreasing T_0 can be explained by the differences in the corresponding neutral distributions. Lower nozzle temperatures result in larger mean droplet sizes and broader distributions. Therefore, the number of neutral droplets produced that are of the sizes observed in the ion-doped distributions increases as T_0 is decreased from 16.0 K to 14.0 K, which results in greater measured ion-doped droplet intensities at T_0 = 14.0 K. The distribution in Figure 5.5a that exhibits anomalous behavior, T_0 = 13.0 K, results from ion capture by droplets formed in Regime II. The measured distribution for T_0 = 13.0 K could be useful in describing the droplet sizes produced in Regime II. However, the ion capture process must be understood before relating the charged droplet size distribution to the neutral droplet size distribution.

Insight into the ion capture process can be gained from analyzing the measured distributions for the Regime I droplets.

Like the neutral distributions, the measured ion-doped droplet size distributions can be fit with the log-normal function shown in Equation 3.8. In Figure 5.5, the black curves correspond to log-normal distributions with the parameters listed in Table 5.1. The log-normal curves in Figure 5.5a fit the experimental data with an agreement of $R^2 > 0.99$. The log-normal curves in Figure 5.5b fit the experimental data with an agreement of $R^2 > 0.96$ for T_0 = 14.0 and 15.0 K, and $R^2 > 0.90$ for T_0 = 16.0 K. As a frame of reference, parameters obtained when fitting neutral droplet distributions produced at similar nozzle temperatures and a stagnation pressure of 40 bar are also shown in Table 5.1.[74] At the same nozzle temperatures, distributions produced at p_0 = 40 bar are slightly narrower and have slightly smaller mean droplet sizes than those produced at p_0 = 50 bar. The ion-doped droplet size distributions result in standard deviations (σ) that are, on average, smaller than those for the neutral droplet distributions, while the values for the mean (μ) are significantly larger. The decrease in σ relative to the neutral distributions is likely due to the presence of an apparent minimum droplet size threshold (Fig. 5.5b), which serves to narrow the distribution. That μ values are larger for the ion-doped distributions is not surprising when considering the large size of the droplets observed. Also shown in Table 5.1 are values for the half-widths, $\Delta N_{1/2}$, of $P_N(N)$. Clearly, the half-widths for the ion-doped distributions are much larger, which follows directly from the much larger values of $\overline{N}$. The large values of $\overline{N}$ and the presence of an apparent minimum droplet size threshold indicate that only a small portion of the neutral droplet distribution is sampled, as discussed below.

Table 5.1 Parameters resulting from fits of data in Figure 5.5 to the log-normal function in Equation 3.8. σ and μ are the standard deviation and mean, respectively, of ln N.

T_0 (K)	Collector-electrode potential (V)	Detector position (mm off-axis)	$\overline{N}$	σ	μ	$\Delta N_{1/2}$
14.0	-15	5	352000	0.680	12.54	394000
15.0	-15	5	152000	0.470	11.82	142000
16.0	-15	5	129000	0.443	11.67	116000
14.0	-15	10	280000	0.569	12.38	292000
15.0	-15	10	126000	0.450	11.64	114000
16.0	-15	10	104000	0.388	11.48	85000
13.5[a)]	-	-	13000	0.612	9.29	11240
15.0[a)]	-	-	8900	0.607	8.91	7719
16.0[a)]	-	-	7741	0.662	8.74	6484

a) Log-normal parameters found by Harms et al. when fitting to neutral droplet distributions produced at p_0 = 40 bar.[74]

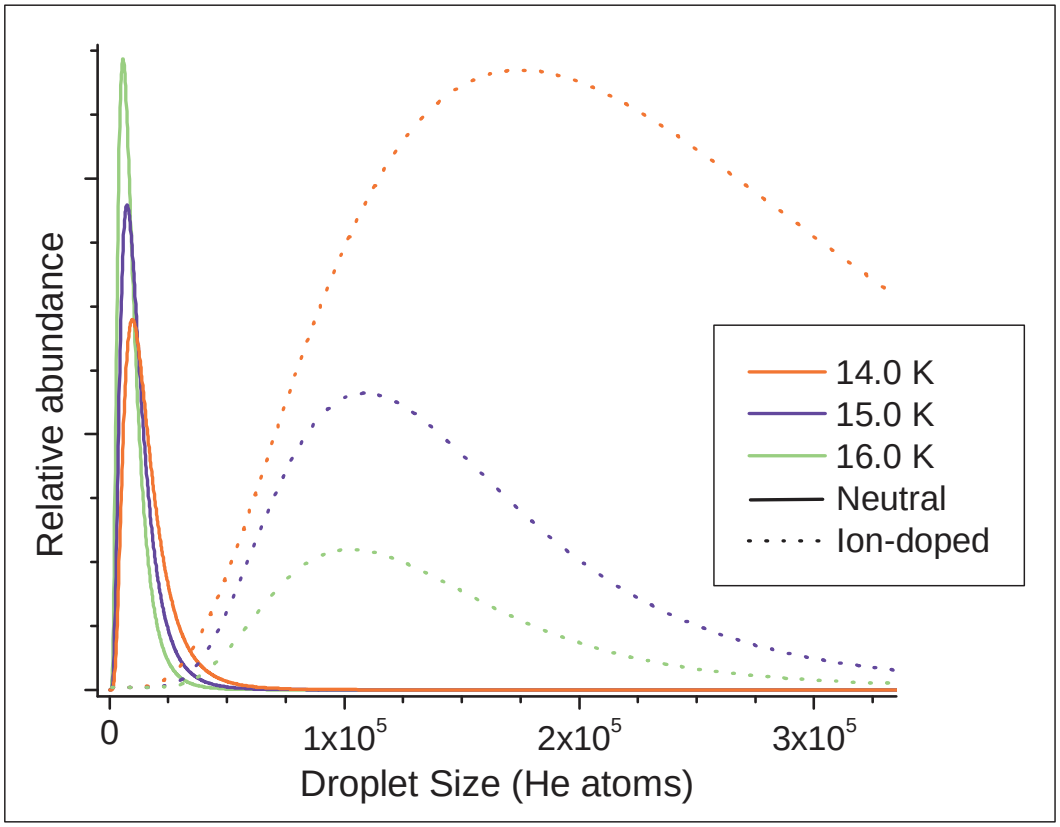

Figure 5.6 Comparison of Regime I neutral droplet size distributions to measured ion-doped droplet size distributions. Solid curves correspond to neutral distributions; dotted curves correspond to log-normal fits to the data in Figure 5.5a.

The log-normal curves resulting from the fits to the data in Figure 5.5a are plotted with their corresponding neutral distributions in Figure 5.6. It can be seen that the ion-doped distributions overlap the region of the neutral distributions that have near-zero relative abundance. These results indicate that the vast majority of the neutral droplets produced are not successful at capturing an ion. This effect is amplified when considering that the ion-doped droplet sizes are indicative of the size of the droplet *after* dissipation of the kinetic energy of the ion. If the process of kinetic energy dissipation requires the evaporation or cleavage of a significant portion of the droplet, which is discussed in the next section, then the droplet size after capture would be much smaller than the size of the neutral droplet before ion capture. Therefore, it is possible that the percentage of the neutral droplet distribution that successfully captures an ion is even lower than suggested by Figure 5.6.

5.2.4 Application of Previously Observed Cooling Rates

Another noteworthy feature of the observed Na^+-doped distributions is the presence of a minimum droplet size threshold, N_{thr}, of approximately 40,000 He atoms. The measured signal increases from zero at N_{thr} to a maximum at droplet size N_{max}, and then decays in a fashion expected from the neutral droplet size distributions. This phenomenon is surprising when considering the various cooling mechanisms that have been observed in helium nanodroplets. To capture an impacting ion, the droplet must dissipate enough of the kinetic energy of that ion for it to be retained by the potential well within the droplet.[90] For the capture of neutral molecules, dissipation of energy is accomplished by the thermal cooling mechanism discussed in Section 2.1, in which the evaporation of helium atoms from the surface of the droplet removes ~5 cm^{-1} of energy

per atom.[37] The dissipation of 15 eV by this mechanism would require the evaporation of >24,000 He atoms.

As discussed in Section 2.2.2, non-thermal cooling processes have been observed upon vertical ionization of neutral molecules embedded in helium droplets, indicating that helium droplets are capable of even more efficient cooling than previously thought.[56,57] These findings have been supported by recent theoretical work, which suggests that two distinct cooling mechanisms are at work when cooling embedded species that undergo vertical ionization.[58] The simulations took into account both the friction due to helium atoms on an ion moving at speeds greater than the Landau critical velocity[91,92] and the quantum nature of the helium droplet, as suggested by results from photodissociation experiments.[93-95] The conclusion of two distinct cooling mechanisms was drawn from the distribution of kinetic energies of the evaporated helium atoms following ionization of embedded Ne_x. The distribution of kinetic energies could be described by a sum of two exponential distributions, one having kinetic energies of 3-7 cm^{-1} and the other having kinetic energies of 28-45 cm^{-1}. Assuming the first 5000 He atoms each remove 20 cm^{-1}, as observed experimentally,[56,57] and subsequent atoms each remove 5 cm^{-1}, the loss of ~9400 He atoms would be required to dissipate 15 eV.

The results of applying the above cooling mechanisms to the neutral droplet distribution produced at T_0 = 14.0 K and p_0 = 50 bar are shown in Figure 5.7. The resulting distributions do not reproduce the shape of the measured Na^+-doped droplet size distribution. The thermal and non-thermal cooling mechanisms require the loss of thousands of helium atoms, which serves to eliminate the portion of the droplet distribution smaller than these critical sizes and shift the remaining distribution to the left.

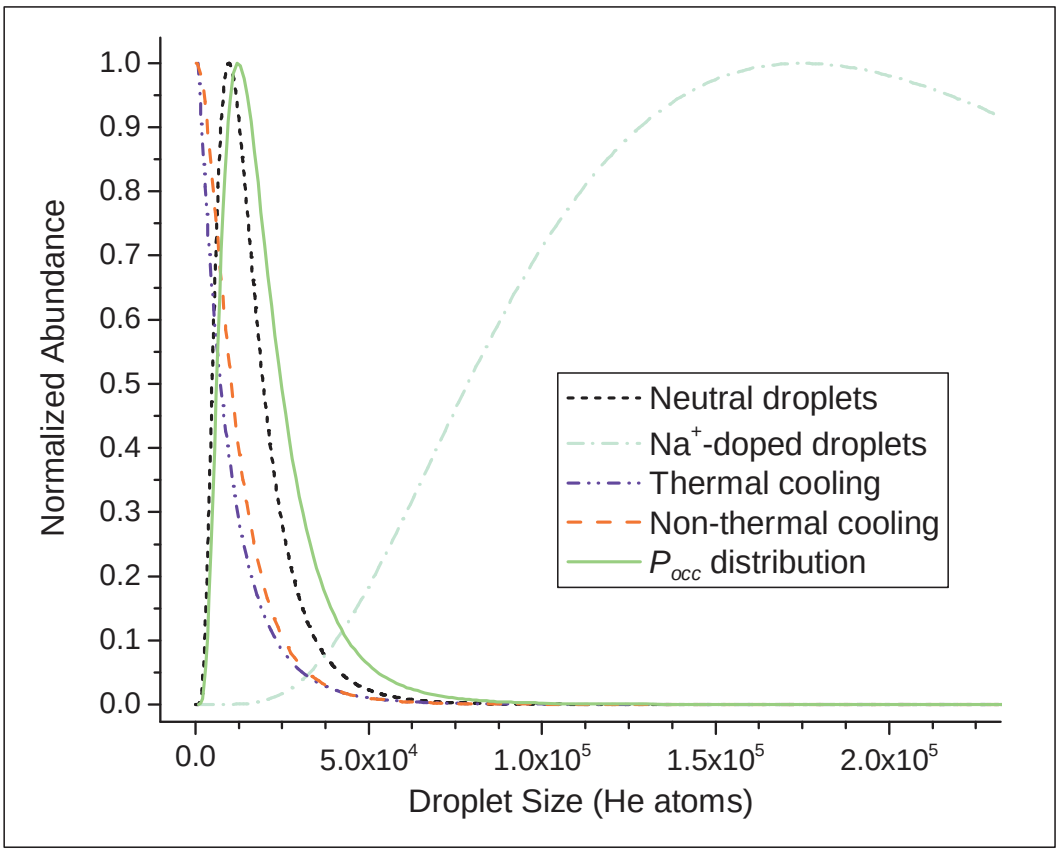

Figure 5.7 Comparison of various droplet size distributions anticipated for capture of a 15 eV ion at T_0 = 14.0 K. Neutral distribution: dotted black curve. Thermal cooling: dash-dot-dot blue curve. Non-thermal cooling: dashed red curve. Measured distribution: dash-dot light blue curve (plotted at arbitrary abundance for clarity). Occupancy probability distribution: solid green curve, normalized for clarity.

These processes both predict Na^+-doped distributions with $N_{thr} = N_{max} = 0$, followed by an exponential decay with increasing N (Fig. 5.7). It is due to the predicted outcomes of these currently accepted cooling mechanisms that the presence of a minimum droplet size threshold is unexpected.

5.2.5 Probability of Ion-Droplet Collision

It could be hypothesized that the shape of the measured Na^+-doped distribution is due to the pick-up statistics associated with the low number density of ions over a short

pathlength. The number density in the pick-up region is about 5×10^4 ions/cm^3, over a pathlength of only a few millimeters. This number density is far below that used in the pick-up of neutral molecules, which is typically 10^{11}-10^{12} atoms/cm^3 over a pathlength of ~2 cm. This point is worth emphasizing: the number density of ions used in this experiment is a factor of roughly 10^6 lower than that typically used in the pick-up of neutral molecules, over a pick-up pathlength nearly 10 times shorter. Larger droplets have larger cross-sections, so they have the highest probability of encountering an ion and it may be expected that N_{max} would be greater than $\overline{N}$ of the neutral distribution. However, as can be seen in the shape of the neutral distribution (Fig. 5.6), there are far fewer of these large droplets produced.

The probability that a droplet of size N is produced and encounters a dopant species can be described by the occupancy probability, P_{occ} (Eq. 3.21). The calculation of P_{occ} for the pick-up of neutral molecules is demonstrated in Appendix B. Using the ion density given above, the maximum in the P_{occ} distribution for one ion occurs at N = 16,000 He atoms with $P_{occ} = 6.5 \times 10^{-18}$. Compare this to the pick-up of a neutral gas at typical conditions, for which the maximum in the occupancy probability distribution occurs at N = 11,000 He atoms with $P_{occ} = 1.5 \times 10^{-5}$, a factor in excess of 10^{12} greater than that for the encounter of an ion. For neutral species at thermal energies, it is assumed that every encounter results in capture; however, this is likely not a valid assumption for the capture of a dopant with 15 eV of kinetic energy since many of the droplets are too small to dissipate this amount of energy. Considering the much lower number densities, and resulting occupancy probabilities, associated with the ion-doping experiment, it is remarkable that Na^+-doped droplets are able to be detected.

Furthermore, the occupancy probability distribution resulting from the ion-doping conditions, plotted in Figure 5.7, is qualitatively similar to the neutral droplet distribution. This similarity is because the number of droplets produced at large N decreases extremely rapidly with increasing N, as indicated by Equation 3.8. Therefore, despite increasing cross-section with increasing N, the much greater number of droplets produced with sizes near $\overline{N}$ dominates the shape of P_{occ}. Thus, accounting for the pick-up statistics does not predict the presence of a minimum droplet size threshold, although it does suggest that vast improvements in the doping of droplets could be made by increasing the ion density and pathlength of the ion source.

5.2.6 Consideration of Experimental Artifacts

It is tempting to attribute the intensity increase from N_{thr} to N_{max} in the measured Na^+-doped distributions to an experimental artifact related to the finite slit width of the detector entrance. In this case, it would be assumed that $N_{thr} = N_{max} \neq 0$. Then, as the potential ramp applied to the steering electrode forces droplets of the size N_{max} toward the detector entrance, some of these droplets are detected before they should be, due to the finite slit width at the detector entrance. This phenomenon would cause a rapid increase from zero intensity to the intensity at N_{max}. At first glance, the Na^+-doped droplet size distributions measured for T_0 = 14.0 K and collector electrode potential of -15 V appear to fit this description (Fig. 5.4a). However, in the distribution measured with the detector 10 mm off-axis, $N_{thr} \approx$ 40,000 He atoms and $N_{max} \approx$ 160,000 He atoms. As described above, the precision associated with the slit width of the detector positioned 10 mm off-axis is ±10%, which indicates that when the steering electrode has an applied potential corresponding to 160,000 He atoms, droplets as small as 144,000 He atoms may be

detected. In reality, this number may be slightly smaller due to field leakage through the 88% transmission mesh across the detector entrance, but it is still significantly larger than the maximum size able to reach the detector when the steering electrode potential corresponds to N = 40,000. Therefore, the presence of a minimum droplet size threshold is not attributed to the finite width of the detector entrance.

5.2.7 Kinetic Energy Dependence

To further probe the ion capture process, the effect on the measured droplet size distribution due to the kinetic energy of the ions was studied. As mentioned previously, the kinetic energy of the ions was defined by the potential of the collector electrode. Through the use of the charge-steering apparatus, the effect of kinetic energy was isolated from the effect of the collector electrode potential on the trajectory of the charged droplets. Therefore, measuring ion-doped droplet size distributions at varying collector electrode potentials allowed for examination of the effect of kinetic energy on ion capture. Distributions measured for the capture of Na^+ with collector electrode potentials of -15, -30, and -45 V, or kinetic energies of nearly 15, 30, and 45 eV, are shown in Figure 5.8. Each of these distributions can also be fit to the log-normal function (Eq. 3.8). The results of such fits are also plotted in Figure 5.8, with the associated parameters given in Table 5.2. It can be seen that there is a slight shift to larger values of N_{max} with increasing kinetic energy.

The dependence of the measured droplet size distributions on kinetic energy may be indicative of the ion capture mechanism. If ion capture were to proceed through either of the cooling processes described above, it would be expected that higher energy ions would cause the loss of a greater number of helium atoms from the droplet. Given the

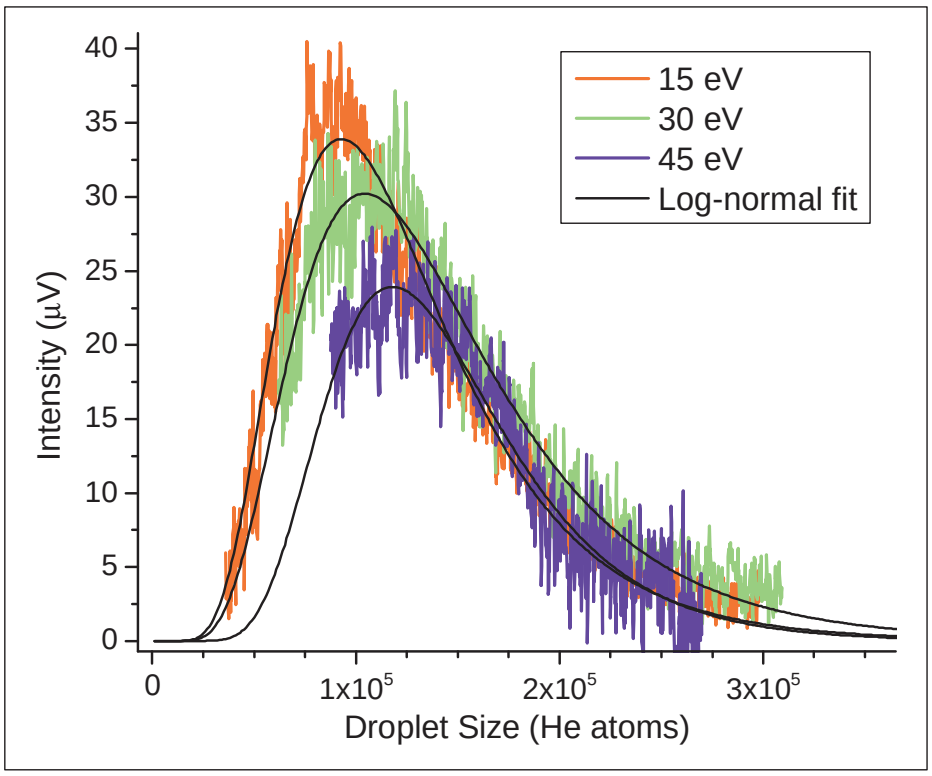

Figure 5.8 Droplet size distributions for capture of Na^+ at various kinetic energies: 15 eV (red), 30 eV (green), and 45 eV (blue). Fits to log-normal function shown in black. Detector positioned 10 mm off-axis, T_0 = 15.0 K.

Table 5.2 Parameters resulting from fits of the data in Figure 5.8 to the log-normal function in Equation 3.8.

T_0 (K)	Na^+ kinetic energy (eV)	Detector position (mm off-axis)	N_{max}	$\overline{N}$	σ	μ	$\Delta N_{1/2}$
15.0	15	10	93000	126000	0.450	11.64	114000
15.0	30	10	104000	144000	0.466	11.77	134000
15.0	45	10	118000	145000	0.369	11.81	113000

same initial neutral droplet size distribution, which is the case for data obtained at a constant nozzle temperature, increasing kinetic energies would result in lower intensities at all N. This predicted result is shown in Figure 5.9, in which the non-thermal cooling mechanism is applied using the same assumptions as above. Clearly, the distributions

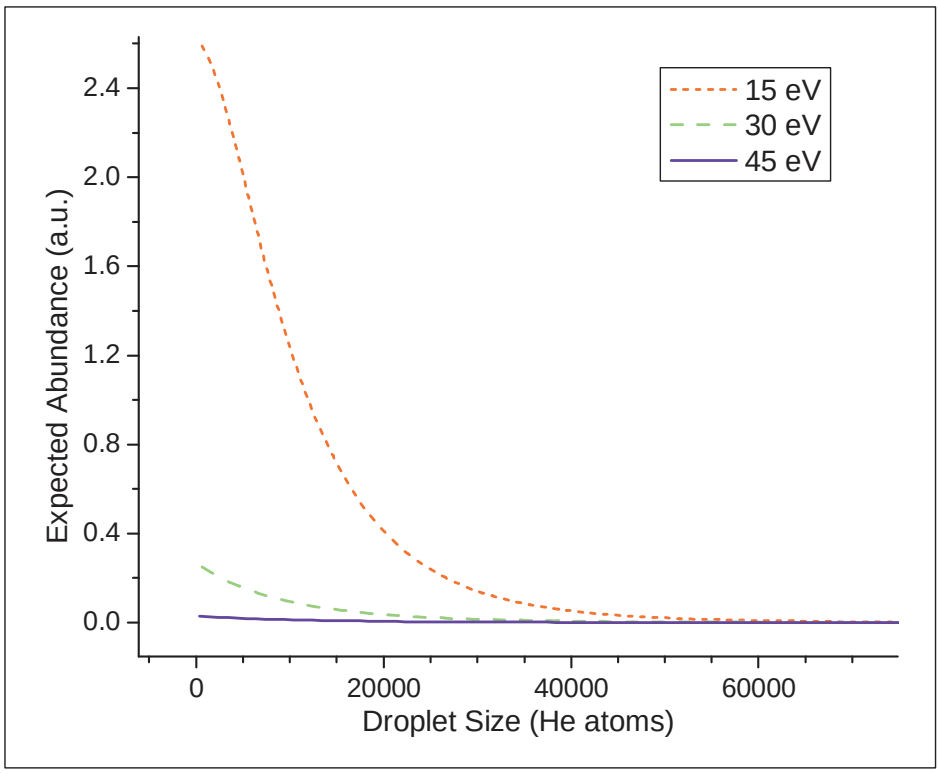

Figure 5.9 Predicted ion-doped droplet size distributions for T_0 = 15.0 K, using the non-thermal cooling mechanism, as a function of ion kinetic energy. Dotted red curve, 15 eV; dashed green curve, 30 eV; and solid blue curve, 45 eV.

predicted by such a cooling process do not accurately model the experimental results. In fact, the observed distributions exhibit a nearly opposite behavior. While higher kinetic energies are expected to result in ion-doped droplet size distributions that are increasingly shifted to the left relative to the neutral distribution, the experiment suggests that the ion-doped distributions are either not shifted at all relative to the neutral distribution or shifted equally by all kinetic energies, as indicated by the overlap of the large N tails of the distributions in Figure 5.8. The effect of increasing the kinetic energy appears to be limited to a shift of $N_{max,}$ and possibly N_{thr}, of the ion-doped distributions to the right (to larger droplet sizes). The shift in N_{max} is ~12,000 He atoms per 15 eV increase in kinetic

energy. These values correspond to energy dissipation of ~10 cm^{-1} per atom, which could be interpreted as an observed average of thermal and non-thermal cooling.

Comparison of the measured ion-doped droplet size distributions to predictions based on previously observed cooling mechanisms is tenuous. In this experiment, atomic ions were generated external to the droplet. These ions were focused by an electric field, which resulted in ions with high kinetic energy that then collided with droplets. Therefore, the ion-doping process shares features of each of the aforementioned cooling mechanisms, but none of the mechanisms possesses all of these features. The thermal mechanism successfully describes the capture of neutral atoms and molecules.[37,76] This process involves external species being captured by the droplet, but these species are not charged and have kinetic and internal energies that are much lower than the kinetic energies of the ions studied here. The non-thermal cooling mechanism is used to describe the fragmentation patterns of molecules that are ionized within the droplet.[56-58] This process addresses the cooling of ions, but the ions in question are formed from neutral molecules already embedded in the droplet and cooled to 0.37 K.

Perhaps the most relevant studies are those on the photodissociation of alkyl iodides in helium nanodroplets.[94,95] These experiments have demonstrated the ability of the droplet to attenuate the velocities of photofragments with 1.25 eV of recoil energy produced by photodissociation. The attenuation of the photofragment kinetic energy was dependent on droplet size, but independent of initial kinetic energy. These phenomena were accurately modeled by assuming a direct escape mechanism in which the photofragment undergoes a series of independent, hard-sphere binary collisions. Implicit in this model are the following features: the mean relative kinetic energy lost by the

photofragment is determined by the number of collisions; in larger droplets, photofragments will undergo a greater number of collisions; the hard-sphere collision cross-sections are independent of the relative speeds of the collision partners; and the mean relative kinetic energy lost by the photofragment per unit distance is independent of the absolute kinetic energy of the fragment.[95] Applying these principles to dissipation of the kinetic energy of an impacting ion, it would be expected that the capture of increasingly energetic ions would require the loss of a greater number of helium atoms from the droplet. The resulting distributions would then be qualitatively similar to those predicted by the mechanisms described above (Fig. 5.9). However, the experiments leading to this model are also not completely analogous to the present work. The photodissociation experiment did study the motion of a moderate velocity species through a droplet, but the species in question was again a neutral molecule that was already embedded in the droplet.

5.2.8 Ion Mass Dependence

Although the hard-sphere collision model cannot be used to explain the observed ion-doped droplet size distributions, the photodissociation of alkyl iodides yields other results of relevance to the capture of an ion. First, the majority of ejected iodine fragments were observed with attached helium atoms, IHe_N, while bare alkyl fragments were primarily observed. These effects were attributed to the high internal energies of the alkyl fragments and the strength of the He-I interaction.[96] The interaction energy of He-I has been calculated to be ~27 cm^{-1},[97] much less than that calculated for Na^+-He (~330 cm^{-1}).[67] If an iodine radical with high kinetic energy was able to retain helium atoms, it then seems reasonable that an alkali cation could remain solvated by helium

atoms at the kinetic energies studied here. Also observed in the photodissociation experiment was a mass dependence on kinetic energy attenuation, with lighter fragments cooled more efficiently than heavier ones. This effect was also accurately described by the hard-sphere collision model, for which the mean energy loss per collision depends on the ratio of fragment mass to helium mass.[95]

The mass dependence of kinetic energy dissipation by helium droplets can be probed in the current experiment by using ions other than Na^+. Plotted in Figure 5.10 are droplet size distributions measured for the capture of Li^+ and Na^+ at equal kinetic energies. Also plotted are fits to the data using the log-normal function. The plots are normalized to clarify the effects of ion mass. The most apparent feature of these distributions is an increase in N_{thr} with increased mass. $N_{thr}(Na^+)$ can be estimated from the log-normal fit to be roughly 30,000 He atoms, and $N_{thr}(Li^+)$ can be estimated to be approximately 13,000 He atoms. Similar to the kinetic energy dependence of ion capture, there does not appear to be a mass dependent effect on the distribution at droplet sizes greater than N_{max}, as the distributions in this region overlap each other. The observation of smaller droplet sizes with lower mass ions fits within the framework of the hard-sphere collision model used to describe photodissociation of alkyl iodides in helium droplets, in which lighter species are cooled more efficiently than heavy ones.[95]

Unfortunately, mass is not the only parameter than changes when changing ions. The binding energy of a helium atom to an alkali cation is calculated to decrease with increasing mass: approximately 700 cm^{-1} and 300 cm^{-1} for Li^+ and Na^+, respectively.[66] Based on the observed binding of helium atoms to ejected iodine photofragments in the photodissociation work,[96] it is reasonable to believe that the binding strengths of the

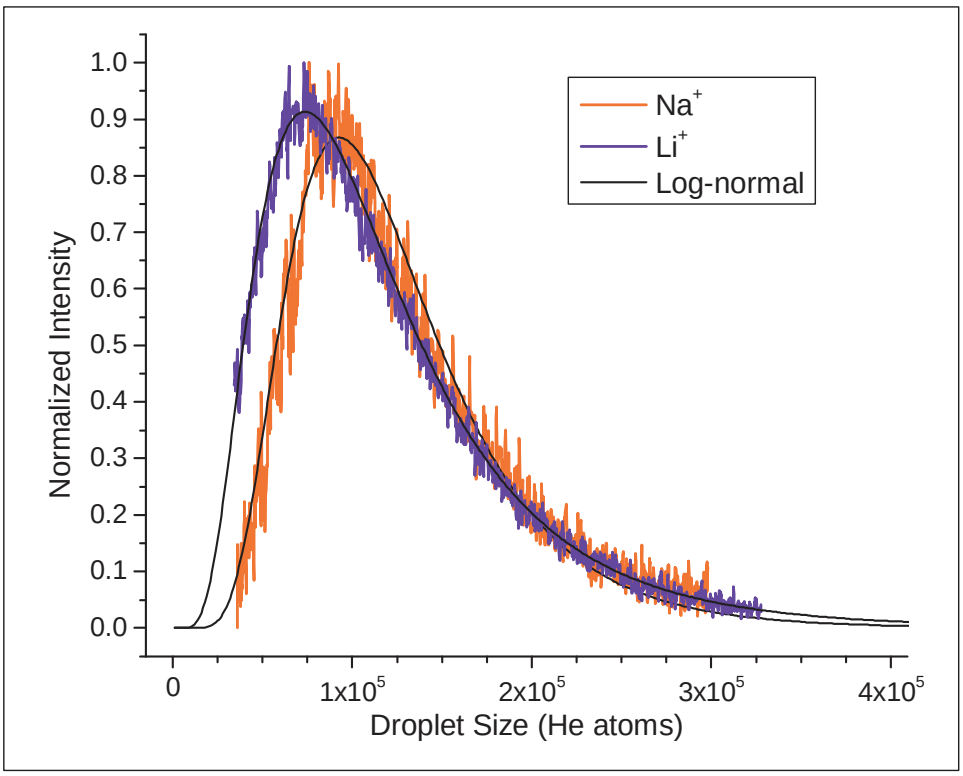

Figure 5.10 Measured ion-doped droplet size distributions for Li^+ and Na^+. Detector positioned 10 mm off-axis, collector electrode potential was -15 V, and T_0 = 15.0 K.

ions could play a significant role in the measured droplet sizes. It must be noted here that the ion source did not have mass-selection capabilities and the preparation method cannot completely eliminate the emission of Na^+. Therefore, although the majority of ions emitted from the source are the alkali cation chosen, slight contributions from Na^+ may be present, but these are not expected to affect the qualitative interpretation of the results. An alternative ion source adapted from a single-ended Q machine[98] is being developed to overcome the mass-selection limitation and will be described in Chapter 6.

5.3 Summary

The capture of alkali cations by superfluid helium nanodroplets was studied by analyzing the size distributions of ion-doped droplets. There are many parameters that may affect the capture of ions by helium droplets. The three parameters studied here were nozzle temperature, kinetic energy of the ion, and mass of the ion. Decreasing the nozzle temperature, T_0, did not result in a change in the minimum droplet size threshold, N_{thr}, but did result in an increase in the droplet size at which maximum intensity was detected, N_{max}, as well as increased intensity at larger droplet sizes (Fig. 5.5). This result is to be expected, as the ion source conditions remained constant and thus the ion capture process should not have changed. The only differences caused by decreasing T_0 are broadening of the distribution of neutral droplets and an increase in the mean droplet size (Fig. 5.6). Therefore, beyond the apparent critical droplet size necessary for ion capture, intensity should increase to some point at which it is limited by the number of droplets of that size available and subsequently decay in accord with the number of droplets produced at increasing size. The data in Figure 5.5 reflect this trend exactly: at T_0 = 14.0 K there is a greater number of droplets produced at large N and this results in a larger value for N_{max} and greater intensity at all values except those near N_{thr}.

The distributions obtained for various kinetic energies (Fig. 5.8) are consistent with the nozzle temperature results. Again, a minimum droplet size threshold is present in the measured distributions, which appears to increase slightly with increasing ion energy. There also appears to be a small increase in N_{max} with increasing ion energy. However, at droplet sizes larger than N_{max} the distributions overlap. The results indicate that the kinetic energy of the ion plays a role in determining the critical droplet size for

successful capture, N_{thr}. Then, as in the distributions obtained with varying T_0, intensity increases to some point at which it is limited by the number of droplets of that size available and subsequently decays in accord with the number of droplets produced at increasing size. Since this experiment was performed with a fixed nozzle temperature, the neutral distribution accessible was the same at each kinetic energy. Therefore, the overlap in distributions at $N > N_{max}$ indicates that changing the kinetic energy of the ion either does not result in an effect on droplets in this region or results in the same effect at all kinetic energies studied. These results are in stark contrast to the distributions predicted by previously described cooling mechanisms, for which the dissipation of energy results in energy dependent loss of helium atoms from the droplet. Such mechanisms predict ion-doped droplet size distributions that have maximum intensity near $N = 0$ He atoms and non-overlapping tails (Fig. 5.9).

The distributions measured as a function of ion mass also display the same behavior as those for nozzle temperature and kinetic energy dependence. That is, the distributions exhibit a minimum droplet size threshold and overlap at $N > N_{max}$. In this experiment, both nozzle temperature and ion energy were kept constant, only the alkali cation studied was changed. In a similar fashion to the kinetic energy dependence, changing the ion resulted in a shift in N_{thr}, from which a slight shift in N_{max} follows. The decrease in N_{thr} observed with decreasing mass is in qualitative agreement with the results of photodissociation of embedded alkyl iodides.[95] However, the cations studied also have different binding strengths to helium atoms, which may play a role in their ability to remain solvated by helium atoms.

Taken together, the results suggest that the mechanism by which high energy alkali cations are trapped in helium droplets cannot be described by previous models. The data indicate that there is a minimum droplet size threshold for trapping these highly energetic ions, which does not depend on the size distribution of neutral droplets before ion capture. The temperature dependence data also show that the abundance of ion-doped droplets at $N > N_{thr}$ is directly related to the abundance of neutral droplets of that size, or greater, before ion capture. The data also show that changing either the kinetic energy or mass of the ion causes a change in N_{thr} and, as a result, in N_{max}. However, changing these parameters does not alter the relative intensities at $N > N_{max}$. The presence of N_{thr} and the behavior at $N > N_{max}$ as a function of kinetic energy and mass are particularly problematic when applying the previously proposed cooling mechanisms. Those models do not predict a critical droplet size for ion capture. They also predict that N_{max} should occur near $N = 0$. The measured ion-doped droplet size distributions best fit a model in which the success of ion capture is determined by droplet size, but the capture process does not dramatically affect droplet size. Such a model would describe the presence of N_{thr} and its decrease with decreasing ion kinetic energy and mass. It would also describe the overlap at $N > N_{max}$ for distributions measured at various kinetic energies and ion masses. That an ion should be captured, for example, by a droplet of 50,000 He atoms and retain those helium atoms, but not be captured by a droplet of 30,000 He atoms, is not an intuitive result. A particular argument against this idea is the rate of decay of the ion-doped droplet intensity at values of N greater than N_{max}, which is much less severe than for either the log-normal distribution or the occupancy probability

distribution for neutral droplets of similar size. This comparison suggests that the droplet sizes do not go unchanged during the ion capture process.

Perhaps the formation of an ion-doped droplet does not involve the capture of an ion by a droplet, but the removal of helium atoms from a droplet by an ion. In this case, the ion could form a snowball of solid helium after impact with the droplet.[62,63] The snowball would then move through the droplet, accumulating helium atoms in a fashion similar to that described for the movement of a charged vortex ring through superfluid liquid helium.[99] This concept raises an interesting point regarding whether the droplet remains superfluid after collision with the ion. It is expected that the energy input would raise the temperature of the droplet such that it is no longer superfluid. The timescales associated with these processes would need to be considered when determining if such a mechanism is possible.

At this point a mechanistic description of the capture of high energy alkali cations is not possible. However, it can be stated that, at the studied conditions, the capture of alkali cations requires droplets greater than ~20,000 He atoms, which results in the majority of neutral droplets produced being discarded. The results indicate that, as expected, the efficiency of droplet doping with ions can be improved by providing a high flux of low energy ions over a longer pathlength. Understanding of the ion capture process would benefit from a thorough theoretical treatment in which the effects due to kinetic energy, velocity, momentum, and mass can more readily be isolated from one another. Furthermore, such work could either incorporate or avoid altogether the effects of differing ion-helium binding energies. Of further interest are similar ion capture experiments involving molecular ions. In the photodissocation work described

above,[95,96] iodine radicals ejected from the droplet were observed to have helium atoms attached, whereas the ejected alkyl radicals were not. An experiment using molecular ions might indicate the possibility of a mechanism in which the impacting ion drags helium atoms with it. Another potential effect worth investigation is that of the vibrational degrees of freedom of a molecular ion. In the photodissociation work, the lack of helium atoms attached to the alkyl radicals was attributed to the internal energy of these species. It is interesting to ponder whether the available degrees of freedom that help neutral molecules couple to the surface modes of the droplet, resulting in evaporation of helium atoms (the thermal cooling mechanism), would result in more or less efficient capture for molecular ions.

CHAPTER 6

DEVELOPMENT OF ION-DOPING APPARATUS

The previous chapters have demonstrated that, at the experimental conditions employed, capture of an ion was limited to helium droplets much larger than the mean size produced by the nozzle. Very few droplets of these sizes are produced, which results in more stringent requirements for detector sensitivity and signal processing. Several reasons for the inefficient doping of droplets with ions have been discussed, including very low number density and high kinetic energy of ions. To address these issues, an apparatus incorporating ion-focusing elements has been designed. Ion-focusing elements were implemented for improved transmission of ions from the source such that lower kinetic energy ions could be used. Focusing elements also improved the overlap of the ion beam with the helium droplet beam, increasing the number density of ions in the interaction region. Modifications to simplify the electric field and ensure the emission of a single type of ion were made. Finally, characterization of the performance of the final version of the apparatus was carried out. The development and characterization results are discussed, as well as some limitations encountered in the current design.

6.1 Initial Design of Apparatus

The primary goal of the apparatus was the production of a high flux of low energy alkali cations for efficient doping of superfluid helium nanodroplets. To achieve this goal, a zeolite-coated filament was used in conjunction with a series of stainless steel electrodes for focusing of thermionically emitted cations (Fig. 6.1). The electrodes are mounted on alumina tubes and separated from each other with alumina spacers, which results in electrical isolation so that different voltages can be applied to each. The assembly is held together by threaded stainless steel rod that passes through the alumina support tubes and has nuts on each end for tightening. The hemispherical-shaped electrode is attached to an aluminum bracket with a thin alumina spacer and alumina shoulder washers to maintain electrical isolation. Stainless steel, alumina, and aluminum components allow the use of elevated temperatures, which is a factor with the resistively heated ion source. The aluminum bracket is mounted to a translation stage, which is mounted to the inside of the top flange of the pick-up chamber. The translation stage allows fine adjustment of the ion-focusing apparatus relative to the helium droplet beam. The coated filament is placed in the hemispherical-shaped electrode, as indicated in Figure 6.1. Applying a positive potential to the hemispherical electrode repels the alkali cations emitted from the coated filament toward the ion-focusing elements. Applying a negative potential to the nearest element extracts the repelled ions and the application of various voltages to the subsequent elements focuses the ions in the region of the droplet beam. Operation of the apparatus in this fashion results in ion trajectories that are orthogonal to the droplet beam, which is directed into the page in Figure 6.1 (depicted by

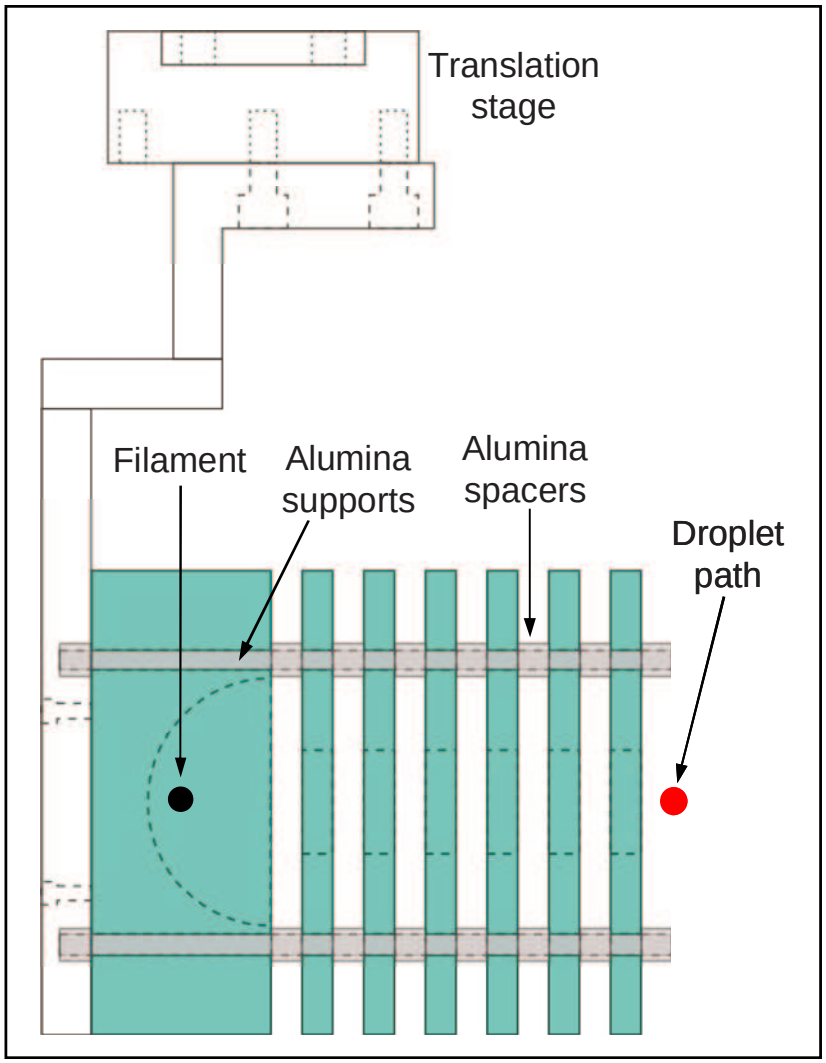

Figure 6.1 Side-view of 1st generation ion-focusing apparatus (electrodes shaded blue).

red circle). This arrangement, however, is not mandatory and other possible geometries are addressed below.

The focusing of cations was modeled using SIMION.[80] An example of such a simulation is shown in Figure 6.2. In the figure the electrodes are shaded brown and labeled 1-7, example ion trajectories are depicted by blue lines, and the red contour lines represent the electric field present in the device. The simulation is representative of typical operation of the apparatus, in which elements 1 and 2 are biased positively and

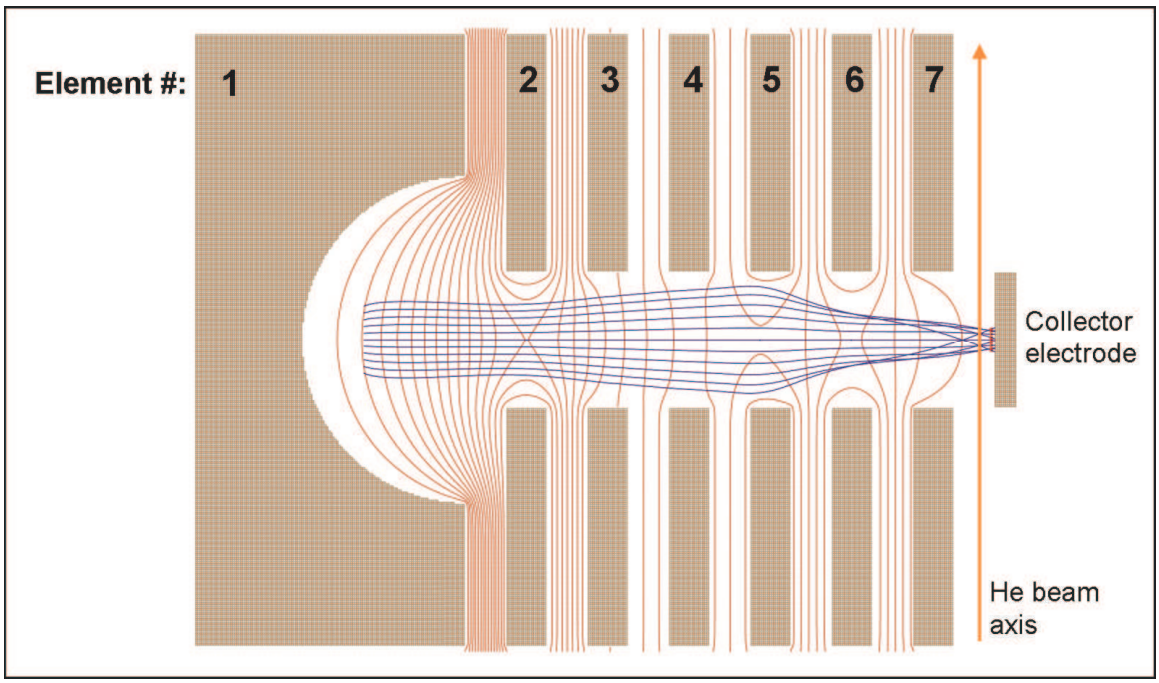

Figure 6.2 Top-down, cross-sectional view of SIMION simulation of ion focusing.

negatively, respectively, to direct the emitted cations toward the droplet beam. Elements 3 and 4 are held at negative potentials that result in a smooth potential gradient between elements 2 and 5. Elements 5-7 function as an Einzel lens, with elements 5 and 7 held at ground while element 6 is adjusted to optimize ion current. A collector electrode is positioned on the opposite side of the helium droplet beam to measure ion current. The collector electrode can also be biased to aid in the extraction of the ions to the region of the droplet beam. However, applying such a bias is undesirable, as it results in the steering of ion-doped droplets off-axis. If the collector electrode remains at ground, and element 7 is also held at ground, the ion-doping region is nearly field-free and ion-doped droplets are not steered off-axis, alleviating some of the problems experienced in the work described in previous chapters.

As mentioned above, the ion-focusing apparatus need not be arranged orthogonal to the droplet beam. Simply placing a hole in element 1 and rotating the device 90° would allow the droplet beam to travel lengthwise through the apparatus. Operation of the apparatus in this arrangement, in which the ion trajectories would be roughly collinear with the droplet beam, may be expected to result in improved overlap and doping efficiency. There are two possible collinear arrangements: ion trajectories countercurrent to the droplet beam, that is, the ions are directed toward the droplet nozzle; or ion trajectories concurrent with the droplet beam, that is, the ions travel in the same direction as the droplets. If the ions travel countercurrent to the droplets, the ion-doped droplets would travel through the electric field that focused the ions, which may result in size-dependent divergence of ion-doped droplets from the beam. Alternatively, if the ion trajectories are concurrent with the droplet beam, the droplets would capture the ions downstream of the apparatus, avoiding the electric field of the apparatus. Unfortunately, the ions would be directed downstream toward the detector, preventing the phase-sensitive detection scheme from differentiating between ion-doped droplets and ions that were not captured by droplets. Therefore, the orthogonal mode of operation was maintained.

6.2 Modifications for Improved Control

The ion-focusing apparatus depicted in Figures 6.1 and 6.2 was able to dope droplets with alkali cations, but the performance was not significantly enhanced relative to the simple ion-doping arrangement employed in Chapters 4 and 5. The lack of improvement was attributed to sub-optimal ion transmission and imperfect alignment with the droplet beam. The use of a hemispherical electrode for element 1 was intended

to improve ion focusing toward the center of the apparatus. However, a non-linear electric field is generated around the filament, which results in ion energies that are not well-defined. A distribution of ion energies makes focusing difficult and limits accuracy when studying kinetic energy dependence of ion capture by helium droplets. Therefore, the first modification made was the replacement of the hemispherical electrode with a flat plate (Fig. 6.3). The use of a flat surface results in an electric field that is linear in the region of the ion source. Electric field linearity allows the ions to be emitted and repelled with well-defined energy.

Improved control of the vertical alignment of the ion beam with the helium droplet beam was achieved by splitting the element nearest the droplet beam (element 7 in Fig. 6.2). The two halves of this element could then have different potentials applied to each for control of the vertical position of the ion beam to correct for any misalignment introduced during assembly and installation. The simplest method of operation involved holding one half of the split element at ground and adjusting the other half to maximize the intensity of ion-doped droplet signal. In practice, the voltage applied was <0.5 V, minimizing perturbation to the field-free ion-doping region and maintaining the function of the Einzel lens. Maximum control over the vertical position of the ion beam was achieved by attaching electrodes to each half of the split element that extend horizontally (labeled “vertical steering electrode” in Fig. 6.3).

The trajectories of low-energy ions are easily perturbed by electric fields. Since one of the goals for this device is the transmission of low-energy ions, stray fields must not be permitted to penetrate the region through which the ions travel. This problem is largely addressed by the large outer diameter of the ion-focusing elements. However, in

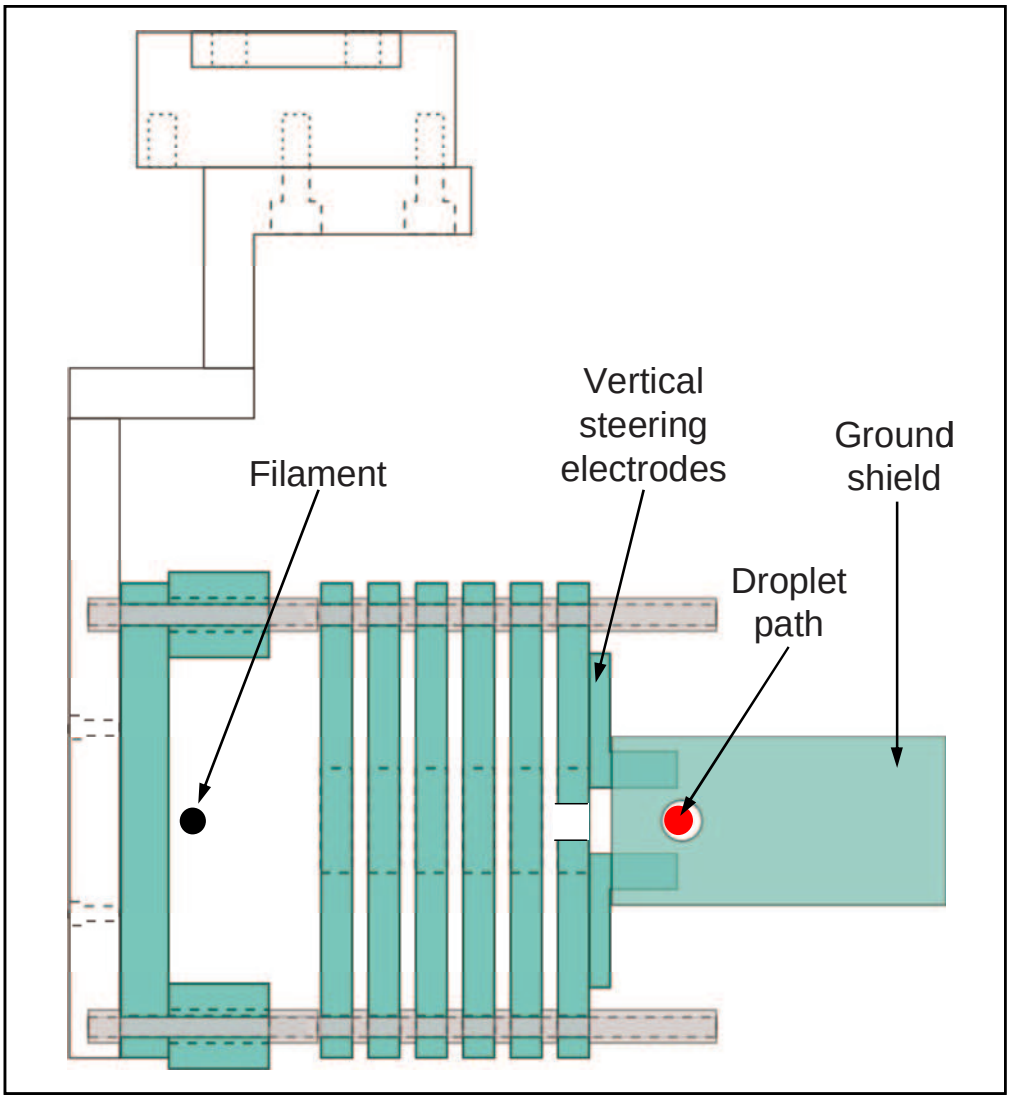

Figure 6.3 Side-view of 2nd generation ion-focusing apparatus.

the design depicted in Figures 6.1 and 6.2, there was no shielding provided in the region where the focused ions collide with the helium droplets. To prevent stray fields from affecting the trajectories of the cations in the droplet-doping region, a shield was mounted to the vertical steering electrodes (Fig. 6.3). The shield rests on a Teflon® sleeve wrapped around the vertical steering electrodes to maintain electrical isolation and was connected to ground. The effectiveness of the ground shield was tested by placing an

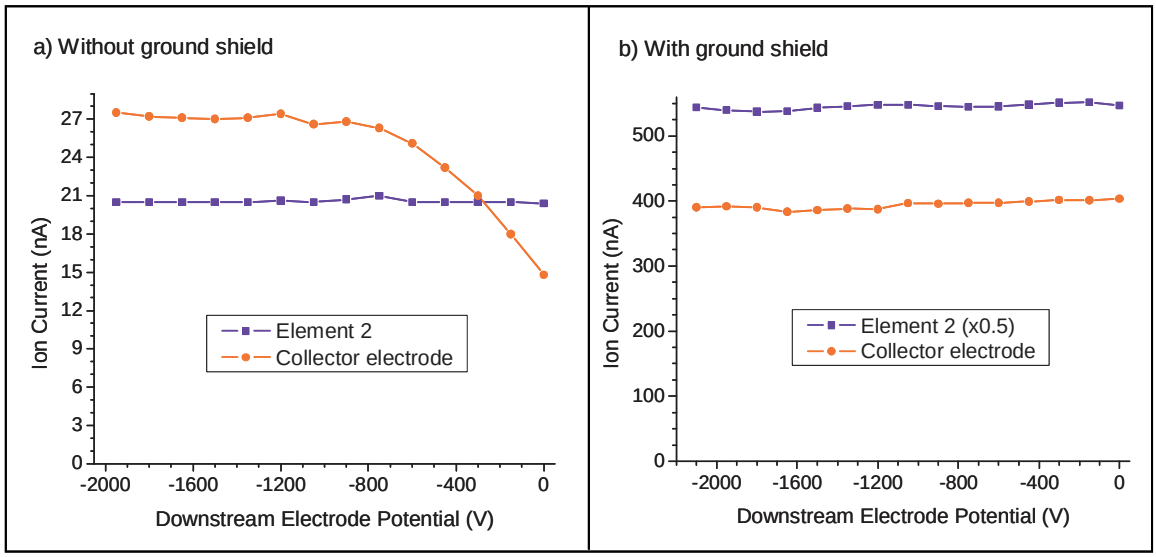

Figure 6.4 Effect of downstream electrode voltage on ion current measured at element 2 and at the collector electrode. (a) No ground shield. (b) Ground shield attached. Differences in measured ion currents between (a) and (b) are due to non-identical conditions and parameters used on different days.

electrode ~1.5 cm downstream of the ion-doping region and varying the voltage. As illustrated in Fig. 6.4a, highly negative stray fields aid in extraction of cations to the collector. If the stray fields affect the ion trajectories they also affect the ion kinetic energies, which prevent the doping of droplets with ions of well-defined kinetic energy. The ground shield was observed to be effective at preventing the interference of stray fields on the current of ions measured at the collector electrode, as shown in Figure 6.4b.

6.3 Modifications for Improved Ion Flux and Selectivity

The changes to the ion-focusing apparatus described in Section 6.2 resulted in improved control of the ion beam and reduced perturbation by stray fields. However, the measured ion current did not reach the desired levels of >10 nA at low kinetic energies (<20 eV). Another shortcoming associated with the designs described in Sections 6.1 and

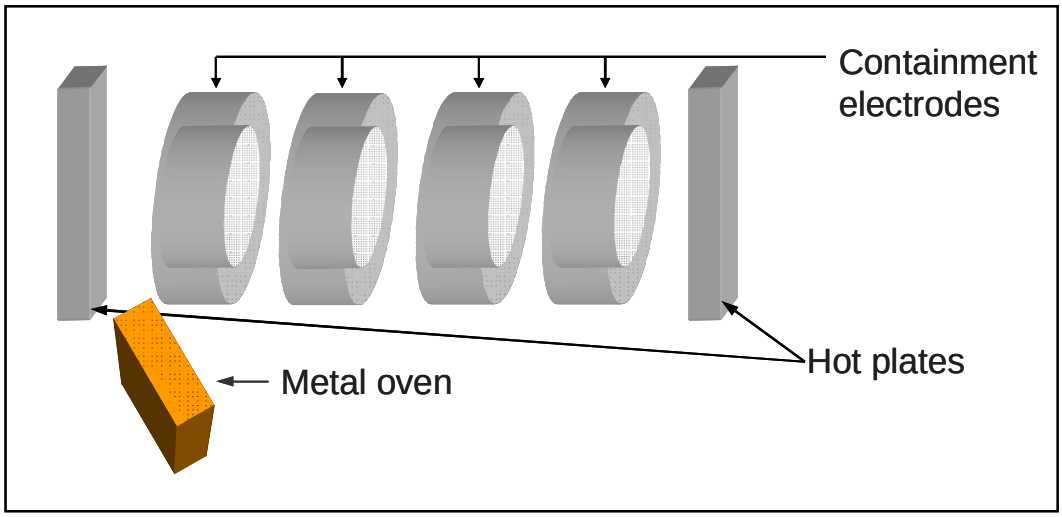

Figure 6.5 Diagram of a Q machine for producing a plasma. Adapted from [100].

6.2 is the inability to select a single type of ion. The zeolite matrix used to coat the filament is naturally rich in Na^+. Therefore, when using a Li^+ source a small amount of Na^+ may possibly be emitted as well. To overcome these limitations the ion-focusing apparatus was modified in a manner inspired by the "Q machine."

Originally described in 1960, a Q machine is a device used to generate a highly-ionized plasma.[101] Advancements in Q machine technology continue to be made as these devices see continued use in studies of plasma instabilities.[102,103] A simplified schematic of a Q machine is shown in Figure 6.5. An oven is filled with an alkali metal, which emits vapor of the metal upon heating. The beam of neutral atoms emitted from the oven is directed toward a hot plate. The hot plates are maintained at temperatures in excess of 2000 °C.[102] At this temperature electrons are emitted and alkali metal atoms are ionized, thus creating a plasma. The plasma is confined by electric and magnetic fields. Typical plasma densities observed in a Q machine are 10^8 –10^{11} cm^{-3}.[102] Certainly, the formation of a plasma, which consists of ions, electrons, and radicals, is not

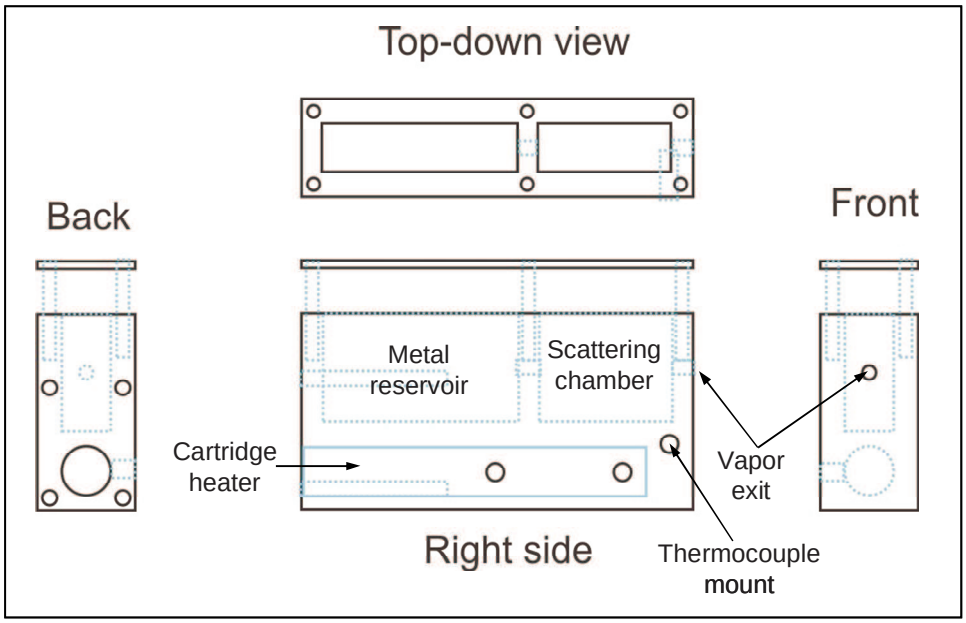

Figure 6.6 Copper oven for producing beam of neutral alkali atoms.

desirable for the doping of helium droplets with ions. However, operating the hot plates at decreased temperatures prevents the emission of electrons and formation of plasma, while maintaining the ability to ionize alkali metals, making the incorporation of the relevant components of a Q machine a natural extension from the device described in the previous sections.

Conversion of the ion-focusing apparatus to a Q machine-type device was accomplished by making several changes, including the addition of a copper oven. The oven consists of two segments: a reservoir for alkali metal and a scattering chamber (Fig. 6.6). Metal is placed in the reservoir and determines the alkali cations produced, which overcomes the aforementioned ion selectivity issue. Upon heating, metal vapor enters the scattering chamber before exiting to the vacuum chamber. The scattering chamber acts as a stage of differential pumping so that the alkali vapor is aerodynamically focused and minimizes the effect of spikes in pressure that may occur while heating the metal. The

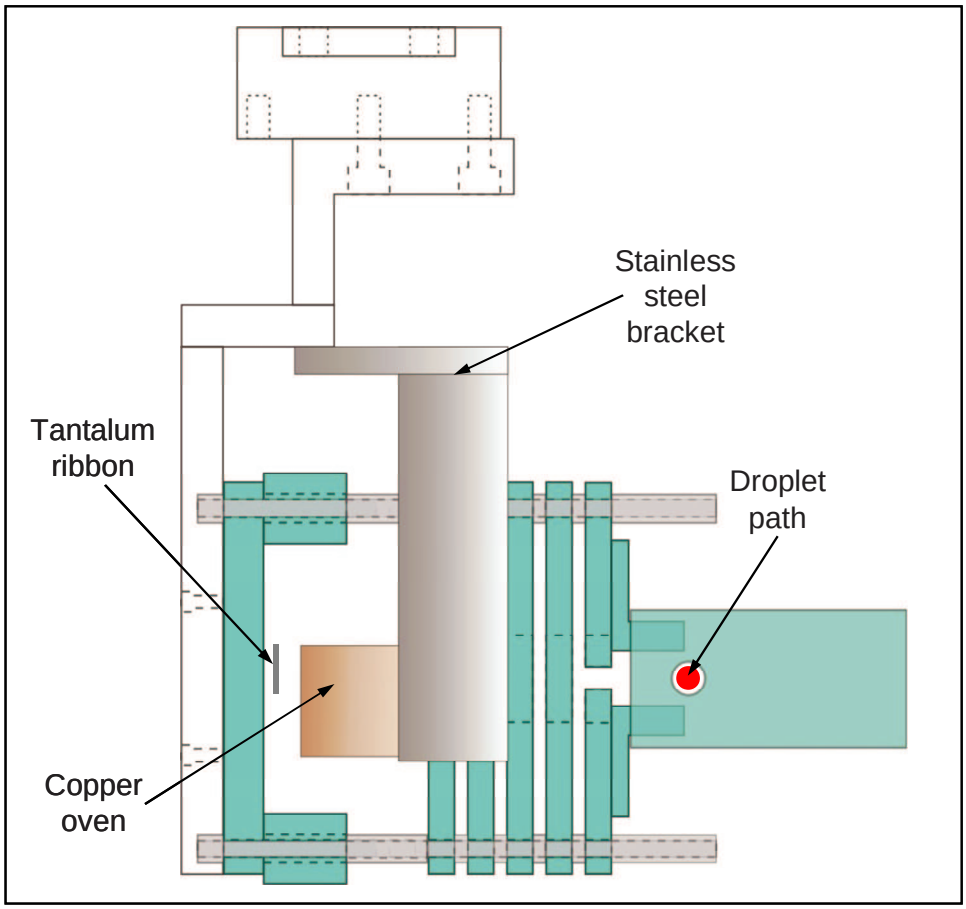

Figure 6.7 Side-view of Q machine-inspired ion source and focusing apparatus.

entire oven is heated by a 100 W cartridge heater (Watlow) inserted into a cavity in the bottom of the oven (Fig. 6.6). The length of the heater and the cavity are such that the heater occupies about half the length of the cavity and the heater is inserted such that it rests against the front of the cavity. This heater arrangement allows for greater heating at the front of the oven, which prevents the vapor exit from becoming clogged with condensed metal. The temperature of the oven is measured by a K-type thermocouple near the vapor exit (Fig. 6.6), which provides an upper limit on the temperature of the metal due to the proximity to the cartridge heater.

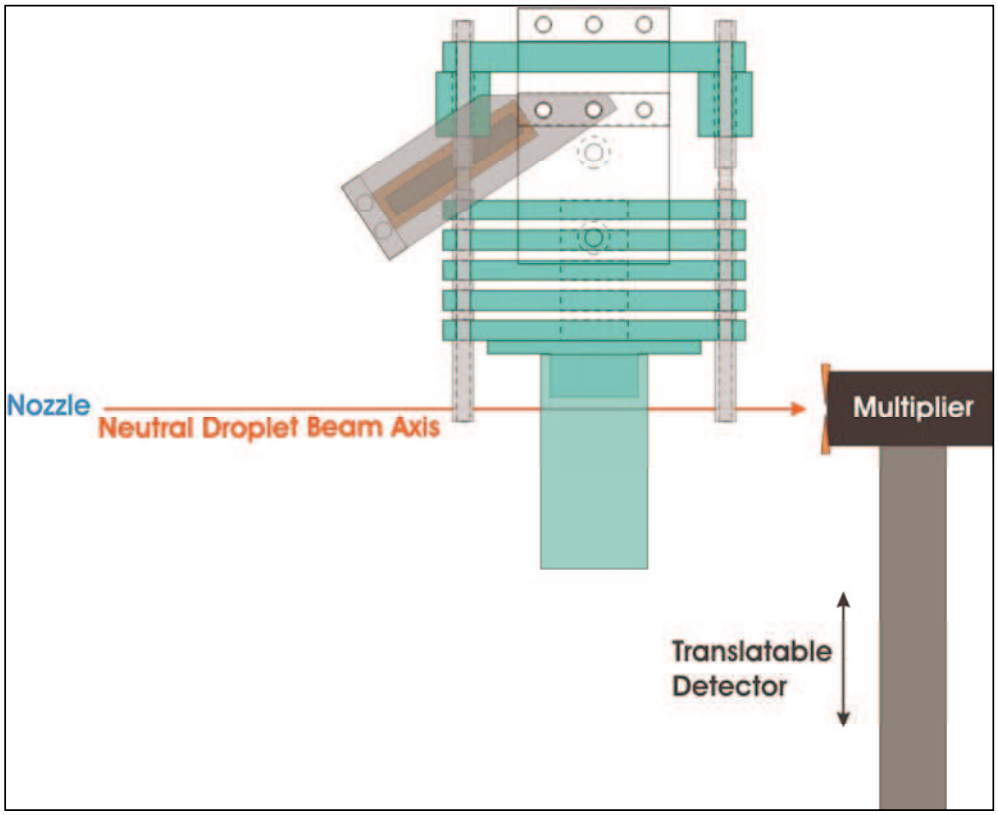

Figure 6.8 Top-down view of ion-doping with Q machine-type ion source and ion focusing apparatus.

The oven is mounted to the ion-focusing apparatus by a stainless steel bracket (Fig. 6.7), which orients the oven ~33° from parallel to the back plate (Fig. 6.8). The angle of orientation was primarily determined by the geometry of the focusing apparatus. In fact, to accommodate the oven, the focusing element nearest the back plate, element in Figure 6.2, was removed and element 3 was beveled to prevent shorting to ground by contact with the oven. Photographs of the apparatus are shown in Figure 6.9, in which the assembled components can be seen.

To improve the efficiency of ionization, a tantalum ribbon was installed in place of the coiled tungsten filament. Use of a ribbon increases the heated surface area for alkali atoms to strike, increasing the probability that the vapor emitted from the oven is

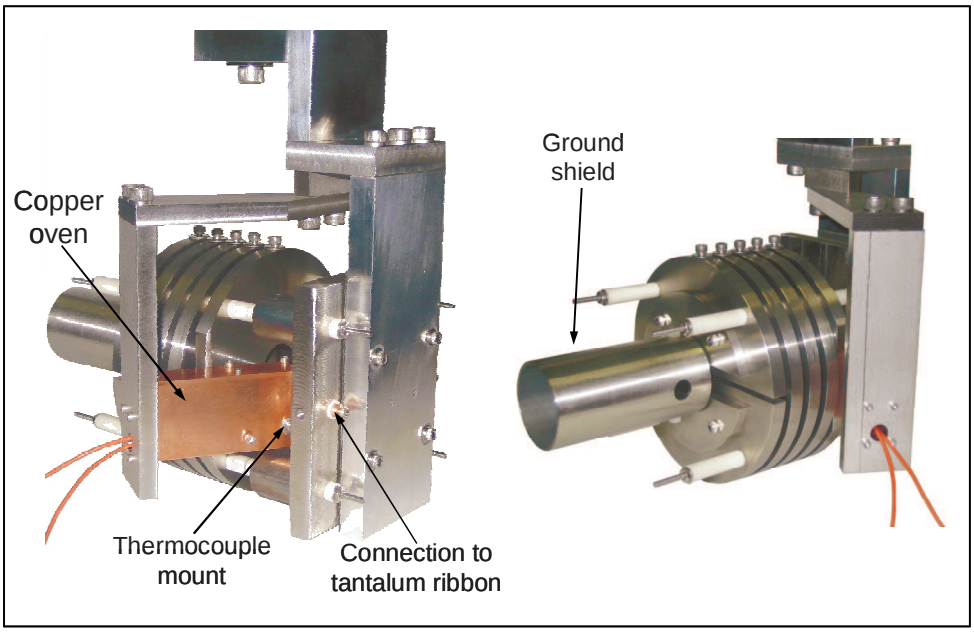

Figure 6.9 Photographs of Q machine-type ion source and ion focusing apparatus.

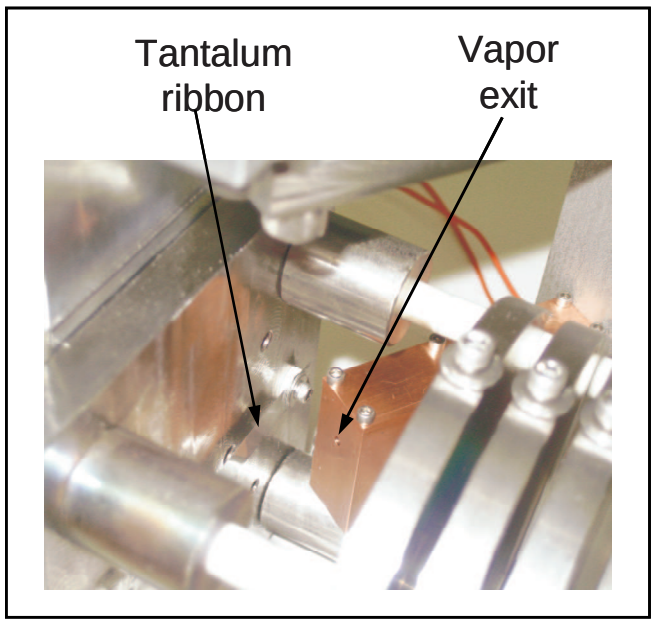

Figure 6.10 Photograph of ion source displaying tantalum ribbon.

ionized. The position of the ribbon is shown in Figure 6.7 and can also be seen in the photograph in Figure 6.10. The ribbon has much lower resistance than the filament, so higher currents are necessary to achieve resistive heating. Therefore, custom copper lugs

were fabricated for connection to the ribbon (Fig. 6.9) and solid copper wire was used to conduct the current. The power supply was floated by a second dc source, which determined the potential bias at which the ribbon was operated. This potential, in combination with the potential of the collector electrode, determines the kinetic energy of ions colliding with the helium droplets.

6.4 Characterization of Q Machine-Type Ion Source

6.4.1 Performance

Experiments to characterize the performance of the modified ion source and ion-focusing apparatus were performed with sodium metal in the oven reservoir. Sodium was chosen for several reasons, which include ready comparison to results obtained using zeolite-coated filaments and the vapor pressure curve of sodium. A satisfactory vapor pressure, 10^{-5}–10^{-4} torr, is generated at oven temperatures of 150–190 °C.[104] These temperatures are within the operating range of the cartridge heater, but above the boiling point of water and other substances that must be degassed from the metal. Ion-doped droplets were detected by the translatable electron multiplier described previously, positioned on the droplet beam axis (Fig. 6.8).

The dependence of ion current measured at the collector electrode and the corresponding Na^+-doped droplet signal on temperature of the copper oven are plotted in Figure 6.11. The ion current and doped droplet signal both increase approximately linearly at oven temperatures of 140–210 °C. This is expected, as increased oven temperature results in greater flux of sodium atoms, which results in a greater number of sodium cations. However, at oven temperatures above 210 °C, the ion current and

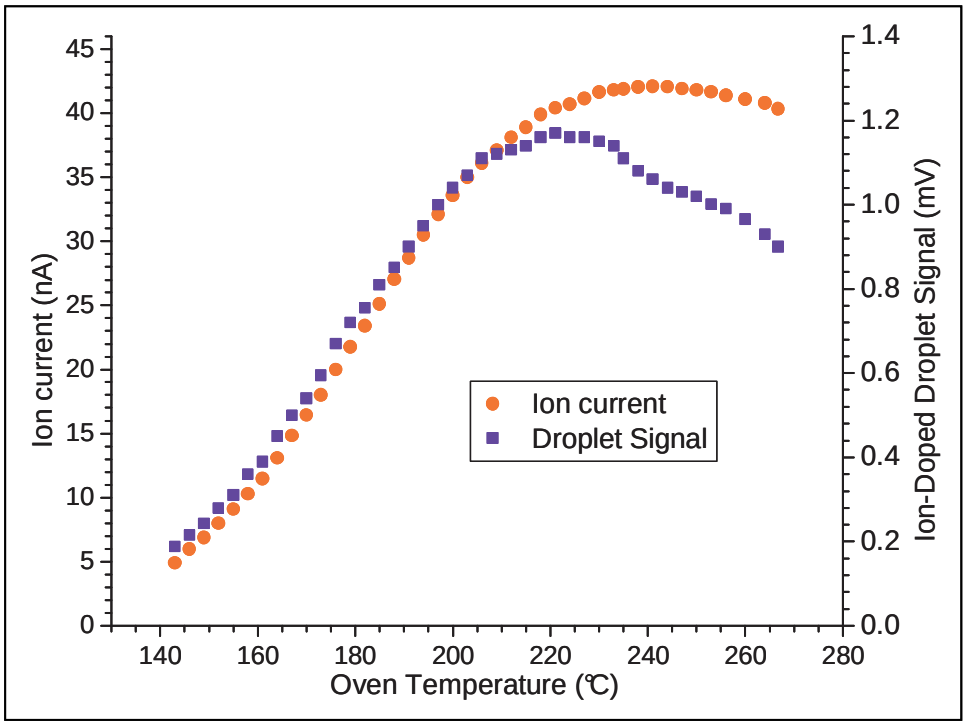

Figure 6.11 Dependence of ion current (red circles, left axis) and Na^+-doped droplet signal (blue square, right axis) on oven temperature.

droplet signal decrease. Initially, it was suspected that the increased flux of sodium atoms at elevated temperature resulted in the formation of enough ions to reach the space-charge limit, at which Coulombic repulsions limit the number of ions capable of occupying a given volume. This hypothesis was supported by the non-linear dependence of sodium vapor pressure on temperature.[104] However, space-charge effects are not likely to occur at the ion currents observed (Fig. 6.11).

Further examination revealed that the pressure of the pick-up chamber increased in a non-linear fashion with increased oven temperature (Fig. 6.12). The dependence of ion current and Na^+-doped droplet signal on chamber pressure is shown in Figure 6.13. At pressures less than ~8.0×10^{-7} torr, the ion current and droplet signal cover a wide range. These values correspond to the regions of Figure 6.11 and 6.12 below 200 °C.

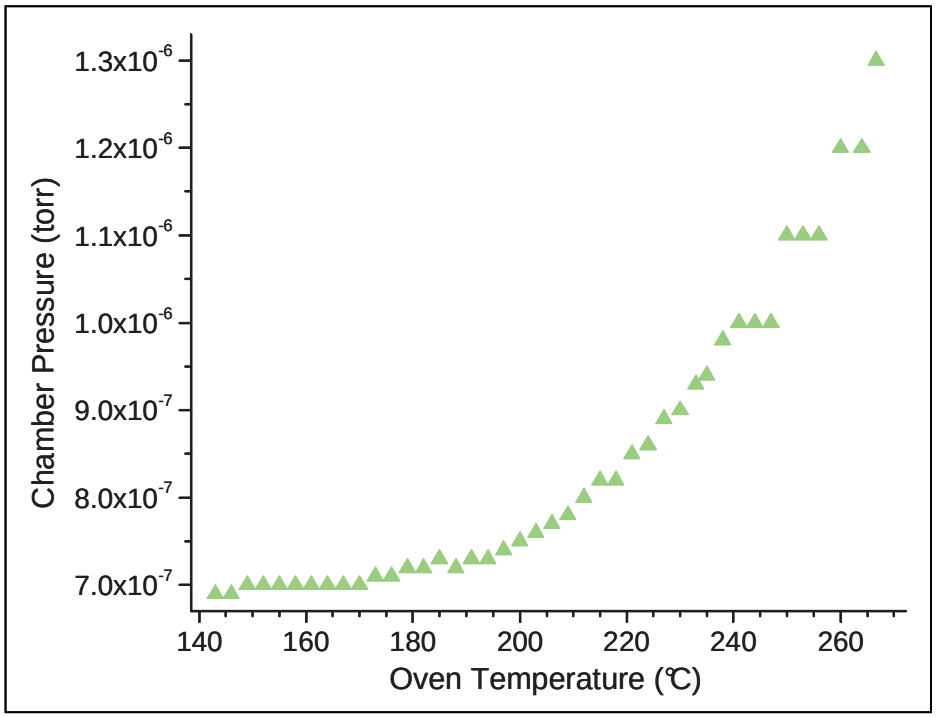

Figure 6.12 Dependence of chamber pressure on oven temperature.

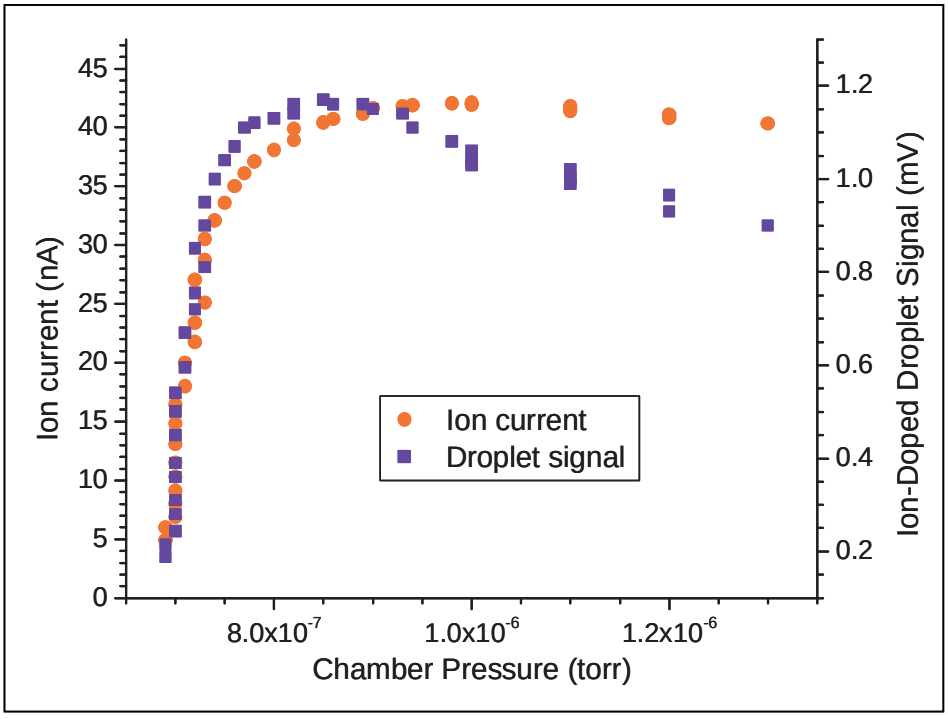

Figure 6.13 Effect of chamber pressure on ion current (red circles, left axis) and Na^+-doped droplet signal (blue square, right axis).

Clearly, the rollover in ion current and droplet signal shown in Figure 6.11 are correlated to increased chamber pressure. The non-linear dependence of sodium vapor pressure on temperature made it a likely candidate to be the cause of the increased pressure. However, EI mass spectrometry of the contents of the pick-up chamber did not reveal gaseous sodium. Instead, as the temperature of the oven was increased, an increase in the intensity of several peaks was observed (Fig. 6.14). The peaks at *m/z* 28, 32, and 44 are most likely due to N_2, O_2, and CO_2 degassing from various metallic parts. The peaks at *m/z* 26, 27, 29, 39, 41-43, and 55-57 are attributed to fragments from hydrocarbon compounds.[105] No known sources of hydrocarbons were present in the chamber. The most likely source was the sodium itself, which is stored in mineral oil. Before use, the sodium was rinsed several times with hexane to remove oil from the surface, but it is possible that oil absorbed into the metal was released upon heating to high enough temperatures. Indeed, an oily substance was observed on surfaces of the vacuum chamber upon inspection.

Despite the limitation placed on ion current by elevated pressure at high temperature, the ion source could be operated at temperatures corresponding to the linear region of Figure 6.11. The ability of the ion-focusing apparatus to efficiently transmit ions was used to study the effect of kinetic energy on the dependence of ion-doped signal on nozzle temperature with the detector positioned on-axis. This was also discussed in Section 5.2.1, however, in that experiment the kinetic energy of the ions was defined by the potential applied to the collector electrode. The effect of ion kinetic energy could not be decoupled from the collector electrode potential in that case. In the experiment discussed here, the collector electrode was fixed at -5 V and the tantalum ribbon was

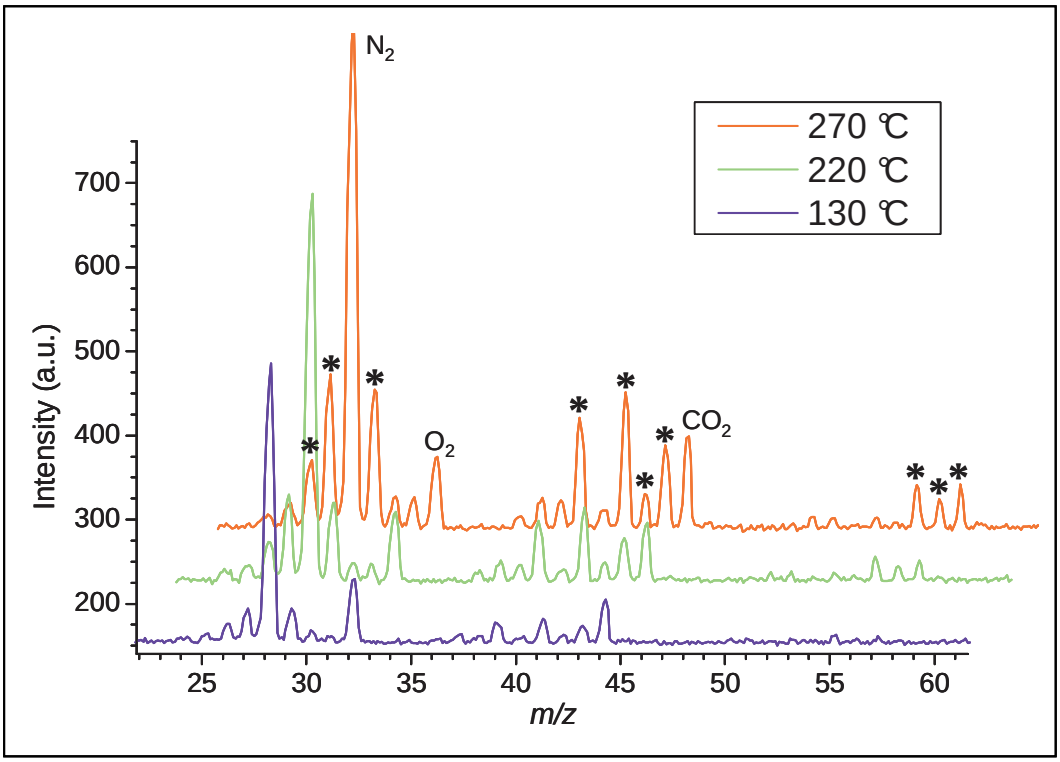

Figure 6.14 Mass spectra of the contents of the pick-up chamber at various copper oven temperatures. Peaks attributed to hydrocarbons are marked with an asterisk (*).

positively biased to determine the kinetic energy. That is, if the tantalum ribbon was floated at +15 V, the kinetic energy of the ions upon reaching the helium droplet beam was ~20 eV.

Shown in Figure 6.15 is the nozzle temperature dependence of Na^+-doped droplet signal at three kinetic energies. The potentials applied to the focusing elements were adjusted at all energies to achieve maximum ion current, but the collector electrode potential was kept constant. The measured signal is normalized in the plot to emphasize the effect of kinetic energy on nozzle temperature dependence. Decreased kinetic energy results in a relative increase in Na^+-doping of smaller helium droplets (higher T_0), as expected. The lowest kinetic energy studied, 8 eV, was the lower limit for achieving

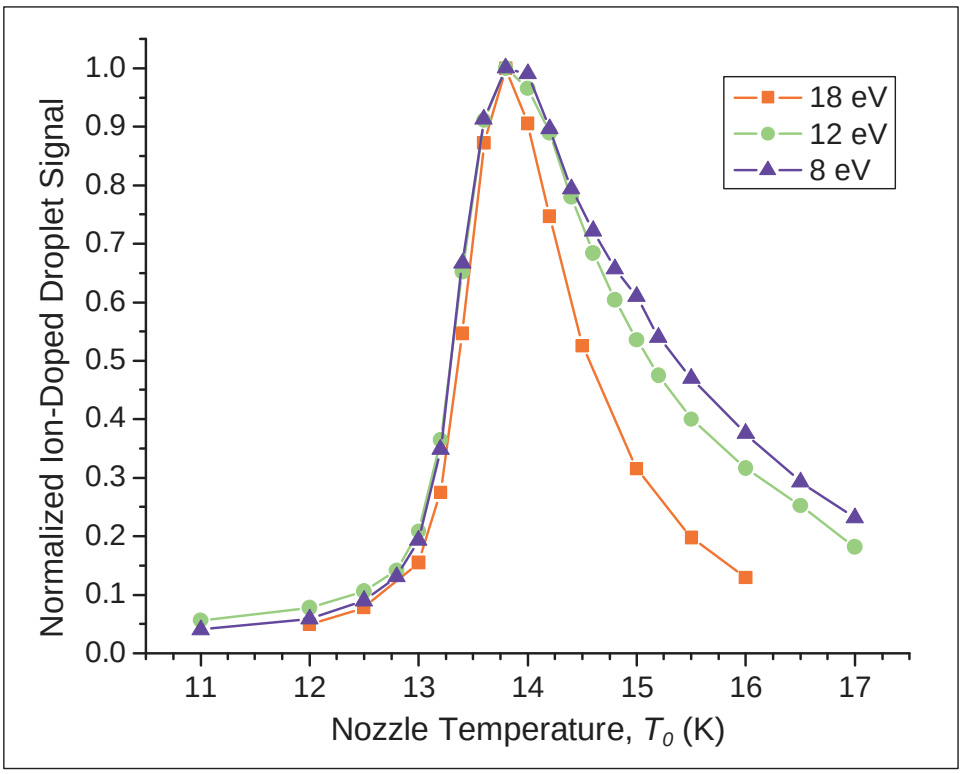

Figure 6.15 On-axis measurement of Na^+-doped droplet signal dependence on nozzle temperature at various kinetic energies.

sufficient ion current. Sufficient ion current at lower energies will likely be achievable through additional tuning of the apparatus or the ability to use higher oven temperatures. Nevertheless, the sustainable production of 8 eV ions is an improvement over the zeolite-coated filament, which can produce either low-energy ions for a short time by using high filament temperatures or high-energy ions for extended time periods.

6.4.2 Focusing Low Kinetic Energy Ions

Although achieving ion-doping with 8 eV ions was an improvement over what was previously accomplished, lower energy ions were desired. To understand why performance decreased at lower kinetic energies, simulations were performed using

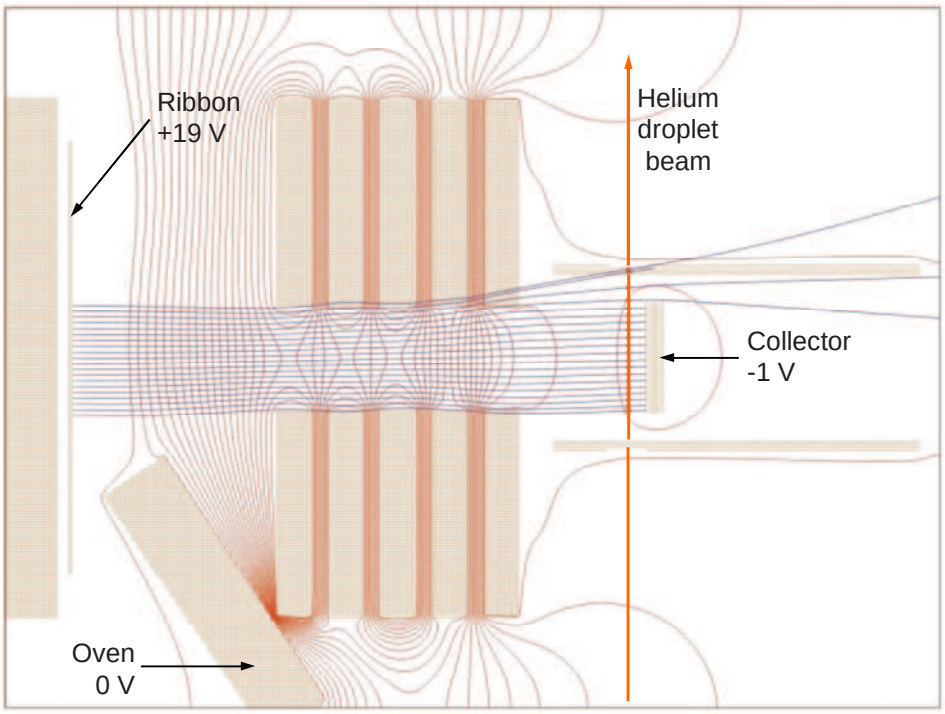

Figure 6.16 SIMION simulation of 20 eV Na^+ trajectories. Brown areas represent electrodes, blue lines are ion trajectories, and red lines are electric field contours.

SIMION.[80] Shown in Figure 6.16 are the trajectories of sodium cations through the ion-focusing apparatus toward the droplet beam. The important parameters are the bias of the tantalum ribbon and the collector electrode, which were +19 V and -1 V, respectively. These values define the kinetic energy of the ions at the droplet beam to be ~20 eV. A collector electrode potential of -1 V was chosen in an effort to move closer to a field-free droplet doping region but is also effective at attracting low-energy ions for measuring ion current. As can be seen in Figure 6.16, the trajectories of 20 eV ions are such that there is good overlap with the helium droplet beam.

Shown in Figure 6.17 is a simulation identical to that shown in Figure 6.16, with the exception of the tantalum ribbon bias, which is set at +4 V, resulting in ion kinetic energies of ~5 eV at the helium droplet beam. The ion trajectories are skewed to one side

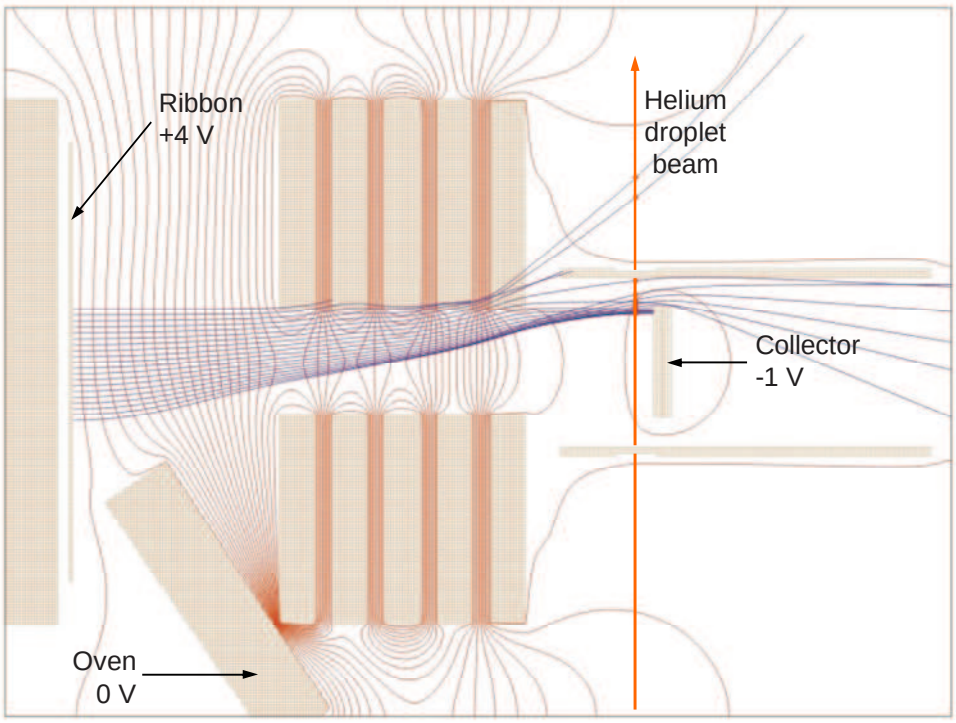

Figure 6.17 SIMION simulation of 5 eV Na^+ trajectories.

due to the asymmetric electric field near the tantalum ribbon. It appears that most of the ions still reach the droplet beam path, but the diminished pathlength of the droplets through the ion beam results in reduced pick-up probability, as described in Section 3.2, and misleadingly low ion current measured on the collector electrode. The asymmetric electric field is caused by the presence of the copper oven at ground potential. Apparently, at the potentials used for generating ions in Figure 6.16, the presence of the oven at ground potential does not disturb the symmetry of the electric field.

Simulations were performed to optimize the transmission of 5 eV sodium cations to the droplet beam and collector electrode. In Figure 6.18 it can be seen that applying -10 V to the copper oven results in a symmetric field in the ionization region. A symmetric field in this region results in ion trajectories that cover more of the droplet

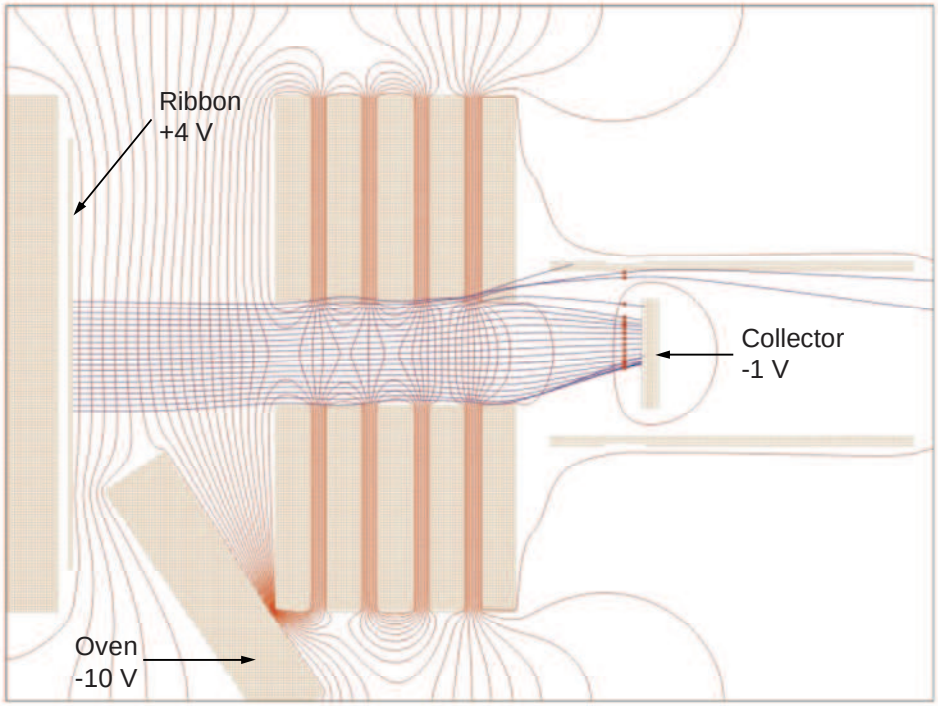

Figure 6.18 SIMION simulation of 5 eV Na^+ trajectories with oven biased to -10 V.

beam path. The copper oven, as currently installed (Fig. 6.9), cannot be floated because it is in electrical contact with the mounting bracket, which is electrically ground. Therefore, experiments have not confirmed that transmission of low kinetic energy ions is improved by biasing the oven. To do so, a spacer plate and shoulder washers made of alumina would have to be fabricated so that the oven could be electrically isolated from the mounting bracket. Alumina is preferable to nylon or Teflon® because those materials would degas, or possibly melt, at the temperatures used.

6.5 Conclusions

Several versions of an apparatus for the generation and focusing of low kinetic energy alkali cations were discussed. The final apparatus, inspired by the Q

machine,[101] uses a copper oven to heat bulk metal to produce atomic vapor. The gaseous atoms strike a resistively heated tantalum ribbon and are ionized. The tantalum ribbon is biased at a positive potential, which repels ions toward the focusing elements and defines the kinetic energy of the ions. The focusing element nearest the ionization region is biased negatively to extract the cations. The three elements nearest the droplet beam function as an Einzel lens: the two outer elements are held at ground while the voltage applied to the center element is varied to optimize the doping of droplets. The element nearest the droplet beam is split into an upper and lower half, which can be held at individual potentials to steer the ions vertically and maximize overlap with the droplet beam. The collector electrode is held at a potential as near to ground as possible to minimize the electric field in the region of droplet doping. Maintaining a low-field droplet doping region reduces the problem of droplet-steering associated with the ion-doping technique employed in Chapters 4 and 5.

The method of ionization employed in the final apparatus has several advantages over the zeolite-coated filament. The use of an oven for emission of metallic vapor avoids the issue of ion selectivity without the use of a complicated mass filter. Although the problem of emitting multiple species of ions from zeolite matrices can be limited through careful preparation and conditioning, it cannot be eliminated completely. Residual metal in the oven could be a concern for ion selectivity purposes, but cleaning and baking the oven is not difficult. Furthermore, the design and construction of the oven is very simple, so it is not cost-prohibitive to have different ovens for different metals.

Other advantages of the updated ion source are the low kinetic energies achievable and the length of time over which this source produces a consistent flux of

ions. The zeolite source can produce sufficient flux of low-energy ions if heated to high temperatures. However, operation of the zeolite source at high temperatures greatly reduces its lifetime. The Q machine-style ion source produces a flux of ions that is proportional to the flux of atomic vapor from the oven. The ability to load more than a gram of metal into the oven reservoir allows for extended periods of continuous operation.

The advantages discussed in the preceding paragraph allowed the doping of droplets with Na^+ at kinetic energies as low as 8 eV, approximately half the kinetic energy at which operation of the zeolite source was sustainable. The inability to effectively transmit and dope droplets with ions < 8 eV was attributed to the asymmetric electric field created in the ionization region by the oven, which was at ground. Based on the results of simulations, it was hypothesized that this problem can be resolved by floating the oven at a small negative potential. The results of doping droplets with ions at 8, 12, and 18 eV of kinetic energy indicate that the kinetic energy of ions does play a role in the relative efficiencies of doping droplets produced at various nozzle temperatures.

The use of the ion source and ion-focusing apparatus is not limited to Na^+. Other alkali cations can be produced as well. K^+ is very easy to produce since potassium has even higher vapor pressure than sodium. Li^+ can also be generated in this source, although the temperatures necessary to produce sufficient vapor pressure of lithium will likely require a more powerful cartridge heater. The apparatus can also be used to transmit negatively charged species by reversing the polarity of the voltages applied to the focusing elements. In fact, the back plate has been modified to accommodate a dispenser cathode, which emits a high flux of low-energy electrons. The ability to

control the energy of a high current of electrons may enable direct ionization of dopant molecules within the droplet at or near the dopant ionization potential. Depending on the resulting internal energy of the ion, and the initial size of the helium droplet, such an ionization process may result in an ion that remains solvated by the droplet.

CHAPTER 7

SUMMARY AND OUTLOOK

The goal of cooling ions was achieved by doping alkali cations into superfluid helium droplets that have an internal temperature of 0.37 K. Initial efforts involved sodium cations with kinetic energies of approximately 200 eV, as defined by the collector electrode potential used to extract the ions toward the droplet beam. The potential on this electrode limited the size of charged droplets able to travel downstream to the detector to roughly 10^6 He atoms or greater. The large droplet sizes were exploited in a scheme to desolvate the ions from the droplet so that the composition of the charged species within the droplet could be identified by mass spectrometry. This experiment revealed that the charged species were indeed sodium cations, with several neutral molecules bound to the ions. Specifically, the ion-neutral clusters observed were $[Na(H_2O)_n]^+$, $[Na(H_2O)_nN_2]^+$, and $[Na(H_2O)_n(HCN)_m]^+$.

The presence of N_2-containing clusters with stoichiometries that correspond to the relative abundances of N_2 and H_2O molecules in the pick-up chamber indicates that the process of picking-up neutral molecules is not altered by the presence of an ion within the droplet. The composition of these clusters, as well as the intensities relative to the H_2O-only clusters, suggest that the clusters do not dissociate during the desolvation process. The N_2 molecule is weakly bound to the ion-neutral cluster, so the desolvation step must

be a low-energy process. Since desolvation imparts little energy to the ion-neutral cluster, the clusters observed in the mass spectra were unlikely to be rearrangement products. This is an important result because it suggests that the observed ion-neutral clusters are formed within the droplet prior to desolvation. For these clusters to form, the neutral molecules must insert into the snowball of solid helium that is known to form around embedded cations. Such an insertion is not unexpected when analyzed in terms of relative binding strengths to Na^+, which are ~5-30 times higher for the neutral molecules studied than for He. It is necessary to note that the picked-up neutral molecules are likely cooled to 0.37 K prior to reaching the snowball, so there is little energy available to rearrange the snowball for molecule insertion. However, ab initio calculations have shown that insertion of H_2O and N_2 into the snowball surrounding Na^+ may proceed barrierlessly. Therefore, the mass spectrometry results illustrate not only the successful capture of externally generated sodium cations, but also the formation of ion-neutral clusters in the helium droplets.

The ability of helium droplets to capture an ion traveling with 200 eV of kinetic energy is impressive, but the study was experimentally limited to droplets on the order of 10^6 He atoms. One of the most powerful abilities of the helium droplet technique is the controlled formation of small clusters, which is not possible when using large droplets at the experimental pressures, ~10^{-7} torr. Therefore, examination of the ion capture process was performed to study the ability to embed ions in smaller droplets. By comparing the distributions of ion-doped droplet sizes to the droplet size distributions before ion capture it was possible to gain insight into the process of ion capture by helium droplets.

Nozzle conditions of p_0 = 50 bar and T_0 = 14.0, 15.0, and 16.0 K were used to produce distributions of neutral droplet sizes that can be described by published scaling laws. The ion-doped droplet size distributions measured for the capture of 15 eV Na^+ at these nozzle conditions exhibit two interesting features: a minimum droplet size necessary for ion capture, N_{thr}, of ~2 × 10^4 He atoms and a droplet size at maximum intensity, N_{max}, greater than 10^5 He atoms. The observed dependence of the measured ion-doped droplet size distributions on nozzle temperature is expected, that is, colder nozzle temperatures result in broader distributions with increased population at larger droplet sizes.

The dependence of the measured ion-doped droplet size distributions on the kinetic energy of the ions was studied. At a fixed nozzle temperature, changing the kinetic energy of the ion resulted in a shift to larger values of N_{thr} and N_{max}, but did not affect the large N tail of the distribution. A similar trend could be observed by maintaining a constant ion kinetic energy, but changing the mass. Decreasing the mass of the ion resulted in a shift to smaller values of N_{thr} and N_{max}. It is expected that increasing the kinetic energy or the mass of the ion would require larger droplets for capture. However, the general shape of the ion-doped droplet size distributions cannot be explained by currently accepted cooling mechanisms.

Applying either the thermal or non-thermal cooling mechanisms that have been discussed in the literature results in a predicted ion-doped distribution that has maximum intensity at N = 0 and exponentially decays with increasing N. That is, the predicted distribution has the appearance of shifting the entire neutral distribution to the left along the x-axis by a given number of He atoms. Similar to the observed nozzle temperature

dependence, the cooling mechanisms predict that lower nozzle temperatures should result in greater intensity at high N. However, the presence of non-zero N_{thr} and N_{max} observed experimentally is not predicted. Similarly, the predictions for kinetic energy dependence state that increasing the ion kinetic energy should result in decreased intensity at all N. That is, increasing kinetic energy is predicted to shift the neutral distribution farther to the left along the x-axis. Interestingly, since both the thermal and non-thermal mechanisms describe cooling in terms of the energy dissipated per helium atom, all ions at the same energy are predicted to require the same number of He atoms for capture. Thus, the accepted cooling mechanisms do not predict a dependence on mass. A mass dependence is, however, predicted by the model of binary hard sphere collisions. In this model, the velocities of lighter objects are expected to be attenuated to a greater extent by collisions. This prediction agrees with the measured ion mass dependence. However, the hard sphere model also predicts that the capture of an ion should shift the neutral droplet distribution to the left, resulting in qualitatively similar distributions as those predicted by the thermal and non-thermal cooling mechanisms.

Several observations can be made from the measured ion-doped droplet size distributions. There is a minimum droplet size threshold for capturing alkali cations at the energies studied, which does not depend on the size distribution of neutral droplets before ion capture. The abundance of ion-doped droplets at $N > N_{thr}$ is directly related to the distribution of neutral droplets before ion capture. N_{thr} and N_{max} depend on kinetic energy and ion mass, however, changing these parameters does not affect the relative intensities at $N > N_{max}$. Since the aforementioned cooling mechanisms cannot describe

these observations, other cooling processes must be considered. This will likely be a rich area for theoretical studies.

Although a mechanistic description of the ion capture process is not possible at this time, the results suggest a number of ways in which to improve the efficiency of ion capture by smaller droplets. Primarily, increasing either the number density of ions in the droplet path or the pathlength of the ion-doping region will result in an increased number of droplets capturing an ion. The number density can be increased by increasing the flux of ions crossing the droplet beam and/or decreasing the kinetic energy of the ions.

An apparatus for generating a high flux of low-energy ions, based on the Q machine, was assembled and characterized. This ion source was able to sustain fluxes of 8 eV ions that were higher than those sustainable for the zeolite-based ion sources. Lower kinetic energies are desirable, and a scheme for improving the transmission of low-energy ions was simulated. This ion source has additional advantages, such as long-term continuous operation and elimination of the emission of multiple ionic species.

Although the key steps of ion capture and ion-neutral cluster formation have been accomplished, improvement in the doping of small droplets must be made for helium droplets to be a viable matrix in which to conduct infrared spectroscopy. The necessity of small droplets arises from the pick-up of background impurities that occurs when using large droplets at the experimental pressures, as mentioned above. Thus, if lower pressures are used, $\sim 10^{-8}$ torr or lower for the instrument described in this dissertation, large droplets can also be used for spectroscopy. Achieving such low pressure is not practical in pick-up chambers in which various atomic and molecular sources are frequently interchanged. Thus, the use of small droplets is desirable. Droplets of the size

typically used in spectroscopy, $N < 5000$ He atoms, have small cross-sections and are able to dissipate a limited amount of energy. Thus, the capture of ions by small droplets will require even higher number densities and lower energies of ions than were attained with the new ion source. The simulated scheme for transmitting low-energy ions with the new ion source should be a step in the right direction.

Alternative ion sources should also be considered. Alkali cations were a good choice for the initial studies because the M^+-He interaction has been modeled extensively, including calculations of M^+ solvated in small helium droplets, where M^+ = Li^+, Na^+, and K^+. Alkali cations are also interesting from a chemical and biological standpoint, making them relevant species for future spectroscopic studies. However, many other species are also of interest and may be easier to embed in a droplet. The study of the ion capture process suggests that the capture of H^+ should be even more efficient than for the alkali cations studied. Furthermore, the use of helium droplets for the cooling of ions is not limited to atomic ions and formation of ion-neutral clusters. IR spectroscopy of polyatomic ions could also be performed using helium droplets, avoiding the complications associated with photodissociation techniques. The capture of externally generated polyatomic ions has yet to be observed and could yield additional information about the ion capture process. Small polyatomic ions could be formed in the chamber via photoionization, or larger ions could be introduced by an electrospray ionization interface. Both of these techniques present unique challenges for coupling to the helium droplet method and ion density may yet be an issue, but exploration in this area could produce fascinating results.

Appendix A

SIMION Modeling of Desolvation Region

A cross-sectional view of the 90° bender and ion optics used for desolvation of ion-neutral clusters from helium droplets and focusing into the mass spectrometer is shown in Figure A.1. The electric fields resulting from the potentials used in Figure 4.1 can be visualized using contours. In Figure A.2, contour lines representing 5 V steps in potential are shown. The contours are plotted on a 2-D "slice" of the assembly that corresponds to the left-most surface displayed in Figure A.1. The electrode potentials are as follows: A, -30 V; B, -40 V; C, -50 V; D, +30 V; E, -10 V; F, -100 V; G, +30 V; and H, 0 V.

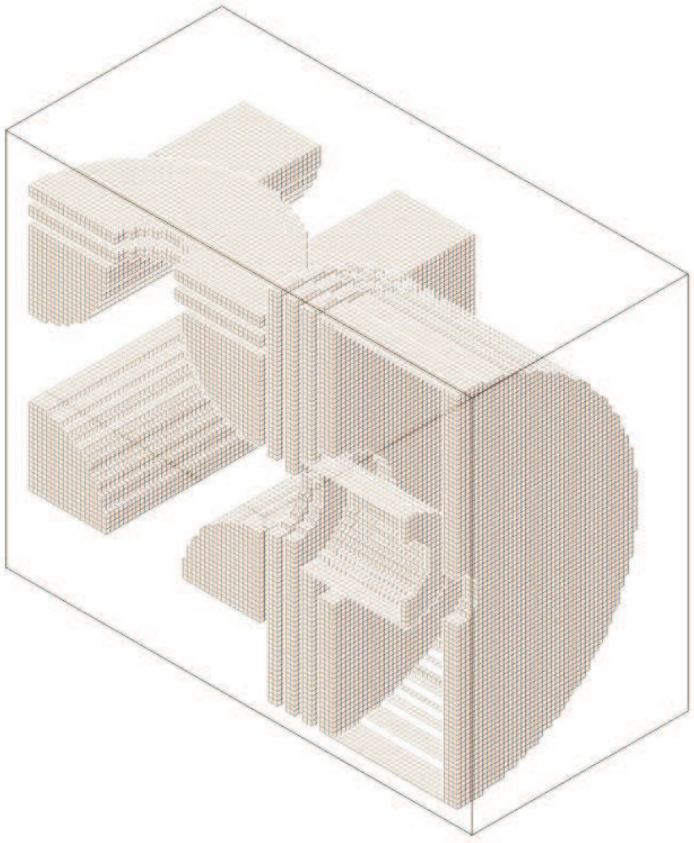

Figure A.1 Cross-sectional view of 90° bender and ion optics.

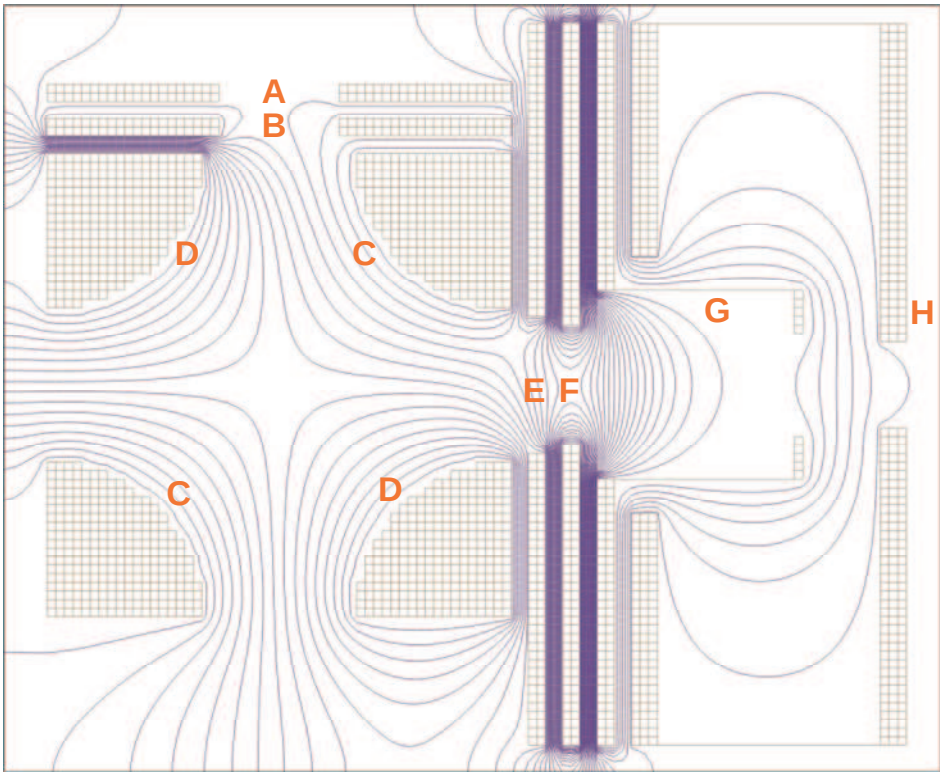

Figure A.2 Electric field in center of desolvation region.
Contour lines represent 5 V increments.

The effect of the electric field on the trajectories of ion-doped droplets is shown in Figure A.3. The simulation uses droplets of the size $N = 10^6$ He atoms (based on the droplet size limitation was discussed in Section 4.1) and assumes a velocity of 350 m/s[69,73] that is either along the beam axis or parallel to it. Beam divergence is not taken into account. It can be seen that the droplet trajectories are perturbed only slightly, with a net downward movement. Including beam divergence would likely result in a small percentage of the droplet trajectories colliding with electrode G (using the labeling convention in Fig. A.2).

Having determined that ion-doped droplets can reach the ion optics region, simulations were conducted to determine the plausibility of desolvated ions reaching the

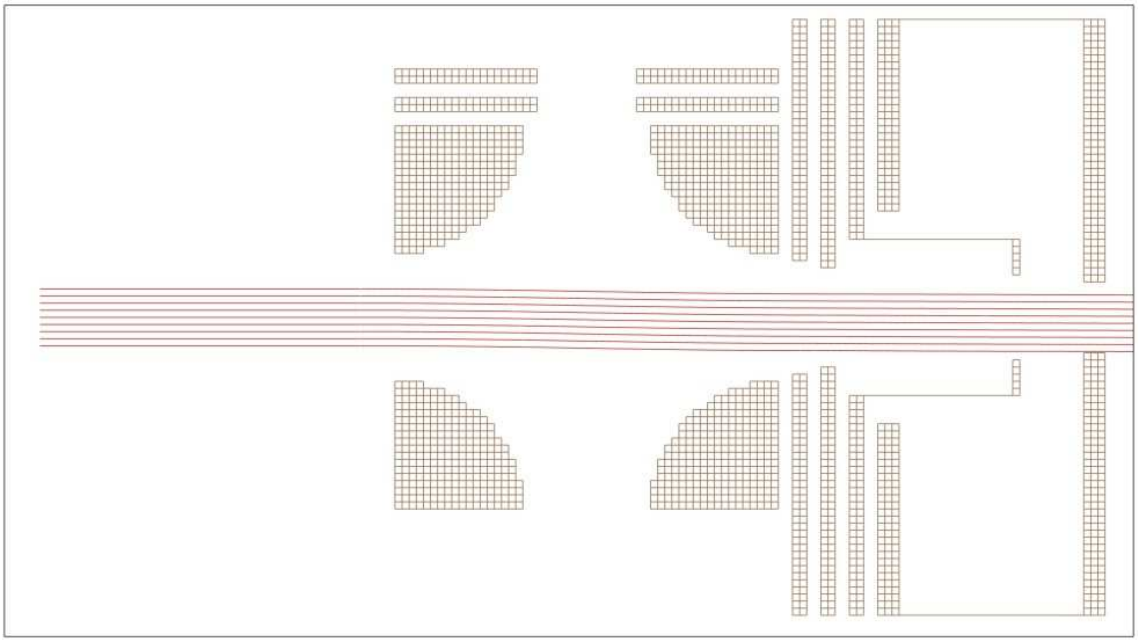

Figure A.3 Trajectories of ion-doped droplets of $N = 10^6$ with $v = 350$ m/s.

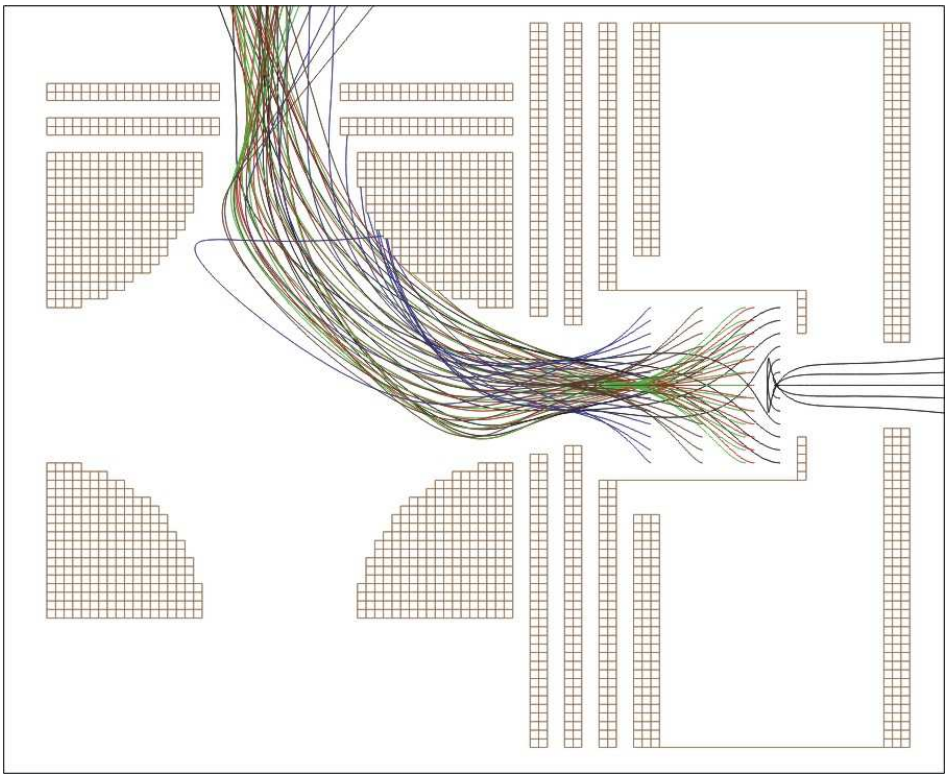

Figure A.4 Possible trajectories of desolvated ion-neutral clusters.

mass spectrometer (Fig. A.4). For ion-neutral clusters to be desolvated and extracted to the mass spectrometer, which would be positioned above the 90° bender in these figures, the ions must go through a turning point. By definition, an object has zero velocity at a turning point. Assuming that the turning point of the ion-neutral clusters occurs upon desolvation, the initial kinetic energy of the model ions should be zero. However, SIMION requires that ions be given an initial kinetic energy. To mimic a turning point, very low initial kinetic energies were used. A range of values were simulated, with little difference in trajectories with initial kinetic energy below 500 meV. The trajectories in shown in Figure A.4 were started with 250 meV of kinetic energy in the –x direction (to the left). Nearly identical results are obtained when staring at this kinetic energy in the +x direction and others in-between. The model ions were assigned a mass of 239 and a charge of +1, corresponding to the most intense peak in the observed mass spectrum (Fig. 4.2). The ions were started at various points in the desolvation region in hopes of gaining insight toward a specific desolvation mechanism.

As can be seen in Figure A.4, most of the simulated trajectories result in successful extraction to the mass spectrometer. Of course, successful extraction from the ion optics region does not imply successful transmission into the mass spectrometer. Starting positions further to the left or right of the range displayed in Figure A.4 resulted in lower transmission. While the results do not lead to support of a particular desolvation mechanism, they do suggest that the individual steps of ion-doped droplets entering the ion optics region and desolvated ion-neutral clusters reaching the mass spectrometer are possible. It is important to note that these simulations confirm that the experiments

discussed in Chapter 4 are possible, but a much more thorough theoretical investigation is required to gain insight into the desolvation mechanism.

Appendix B

Calculation of Occupancy Probability

As described in Section 3.3, the occupancy probability, P_{occ}, is the probability that a droplet of a given size, N, is produced and captures a given number of dopant molecules. In this case the number of dopant molecules is denoted n, corresponding to the number of water molecules in the $[Na(H_2O)_n]^+$ clusters observed in Figure 4.2. From Equation 3.21, it can be seen that the occupancy probability is the product of the droplet size distribution and the Poisson distribution of pick-up probability.

The first step in calculating P_{occ} was the calculation of the distribution of droplet sizes produced at the nozzle. As stated in Section 3.2, the Regime II expansion conditions result in a distribution of droplet sizes that is not well-understood, but are known to be $>10^5$ He atoms. Since the droplet size distribution at these conditions has not been quantitatively described, both the log-normal and linear-exponential functions were modeled. The log-normal function that describes Regime I expansions and the linear exponential function that describes Regime III expansions are shown in Equations 3.8 and 3.14, respectively. The droplet sizes detected by the mass spectrometer were estimated to be $\geq 10^6$ He atoms, with slightly smaller droplets possible due to divergence of the droplet beam. Therefore, when calculating the occupancy probabilities, a minimum droplet size cutoff, N_{min}, was implemented. The contributions to the droplet size distributions by droplets of $N < N_{min}$ were removed. The droplet size distributions resulting from a mean size, $\overline{N}$, of 3.0×10^5 and $N_{min} = 9.0 \times 10^5$, are compared to a log-normal distribution without a minimum droplet size cutoff in Figure B.1. The standard

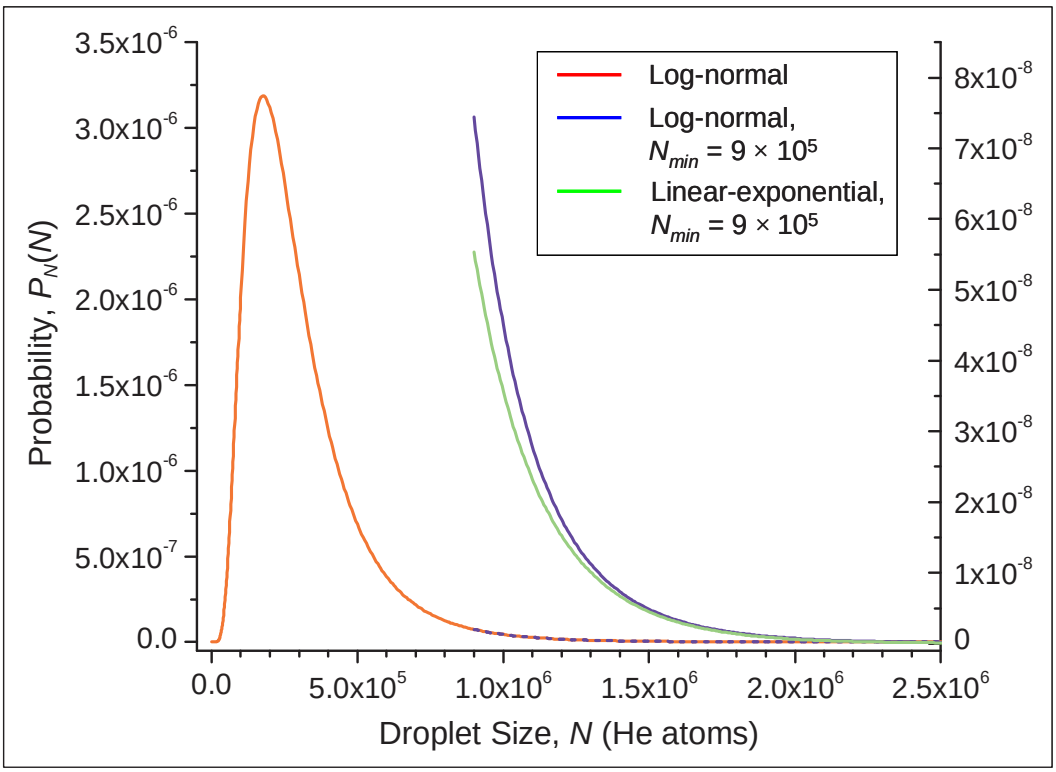

Figure B.1 Probabilities of producing droplets of size N at experimental conditions.

log-normal distribution (red) corresponds to the y-axis on the left. The log-normal (blue) and linear-exponential (green) distributions with droplets smaller than N_{min} removed correspond to the right y-axis. Note the dramatically lower probabilities associated with the production of droplets with $N > N_{min}$.

The next step was the calculation of the Poisson distributions (Eq. 3.20) for the pick-up of various numbers of water molecules. The description of the Poisson distribution can also be found in Section 3.3. As can be seen from that description, the number density of dopant molecules must be known. This was determined from the pressure, p_{H_2O}, and temperature, T_{H_2O}, of water vapor in the chamber:

$$\eta = \frac{p_{H_2O}}{kT_{H_2O}}, \qquad \text{(A.1)}$$

where k is the Boltzmann constant, pressure is in Pascals, and temperature is in Kelvin. This determination of gas density assumes ideal gas behavior, which is valid for the pressure and temperatures studied. The pressure of water was taken as 90% of the background pressure (based on EI mass spectra) in the chamber and the temperature was taken as slightly above room temperature, based on temperature measurements taken in previous experiments. The resulting values were $p_{H_2O} = 3.73 \times 10^{-5}$ Pa, $T_{H_2O} = 300$ K, and $\eta = 9.01 \times 10^{15}$ m^{-3}. The gas density was then used in the calculation of the parameter β, which also depends on droplet size and pathlength. In the experiment, the pathlength over which droplets may encounter water molecules was roughly 0.63 m.

The above determination of β assumes that the dopant molecules are stationary on the timescale of droplet flight. However, this is definitely not the case. In fact, the dopant molecules have a greater average velocity than the droplets. As mentioned in Section 4.1, the velocity of the droplets studied was estimated as 350 m/s. The mean speed, $\langle v \rangle$, of the dopant molecules was determined from the temperature and mass, m, of the dopant molecules:

$$\langle v \rangle = \left(\frac{8kT}{\pi m} \right)^{1/2}. \qquad \text{(A.2)}$$

Water molecules at 300 K were calculated to have a mean speed of ~600 m/s, a factor of 1.7 greater than that of the helium droplets. The correction due to these relative velocities was applied simply by multiplying β by the ratio of the velocities, 1.7.[76] A relative velocity ratio greater than 1, which is the case whenever the dopant molecules

have an average speed greater than the velocity of the droplets, serves to increase pick-up probability. This is a logical outcome because, at a given number density, increased dopant velocity results in a greater number of dopant molecules passing through the droplet path during the time of flight.

The Poisson distributions calculated using the experimental parameters described in Chapter 4 are shown in Figure B.2. As can be seen, the probability of pick-up for low numbers of dopants maximizes at smaller droplet sizes. Larger droplet sizes are more likely to capture multiple dopants. This makes sense when recalling the dependence of pick-up probability on the cross-sectional area of the droplet (Eq. 3.12-14). Shown in the figure are distributions for the capture of 1-10 water molecules. However, distributions were calculated up to $n = 47$ to emulate the size of clusters observed experimentally.

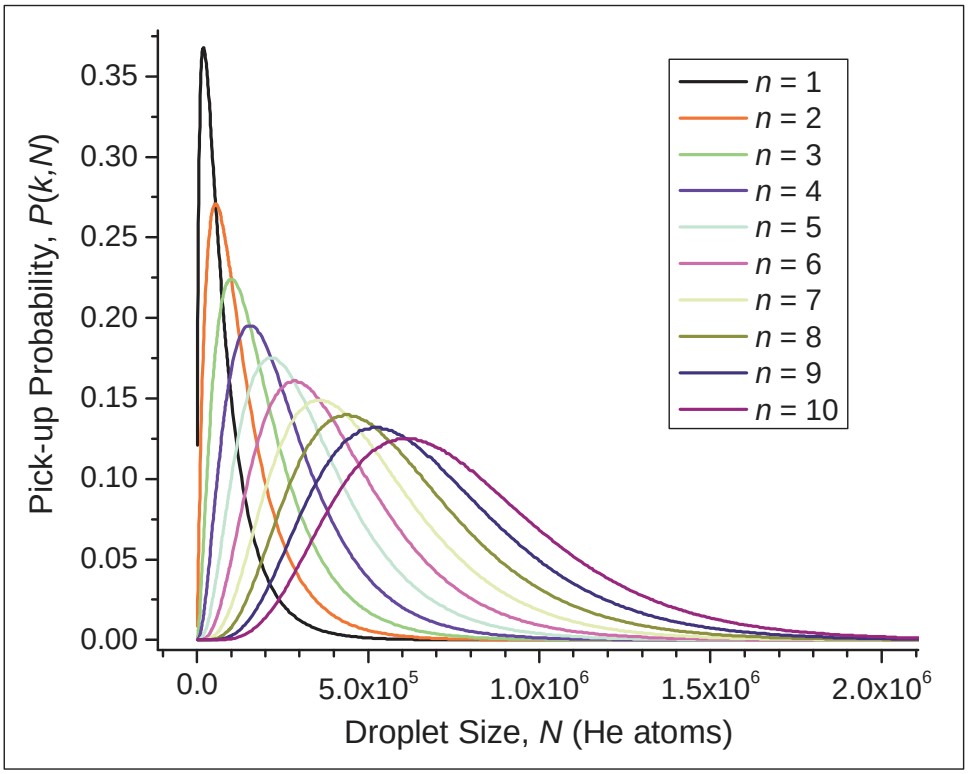

Figure B.2 Poisson distributions for experimental conditions used in Chapter 4.

Having calculated the log-normal and linear-exponential droplet size distributions and the Poisson distributions for n = 1-47 as a function of droplet size, occupancy probability distributions were calculated. Multiplication of the Poisson distributions from Figure B.2 by the droplet size distributions from Figure B.1 resulted in occupancy probability distributions as a function of droplet size. Example P_{occ} distributions for various values of n are shown in Figure B.3. From these curves it can be seen that, at the experimental conditions, the large droplets studied result in the capture of multiple dopant molecules.

The occupancy probabilities in Figure B.3 were not directly comparable to the mass spectrum in Figure 4.2. From those curves, the probability that a droplet of a given size is formed and then picks-up n molecules can be measured. To determine the probability that a cluster of a given size is formed, each of the occupancy probability curves was integrated. The probability is plotted vs the cluster size, n, as shown in Figure B.4 To compare these distributions to the mass spectrum, the probabilities were normalized such that the maxima equal 1 and the cluster size was converted to cluster mass by the formula $m/z = 23 + 18n$. The end result is the plot shown in Figure 4.8. Without the use of a minimum droplet size cutoff, the integration of the curves in Figure B.4 would yield a value of 1, as is the definition of a probability distribution. However, the presence of a minimum droplet size cutoff eliminates the majority of the droplets produced. In fact, integration of the curves in Figure B.4 yields values of 0.016 and 0.013 for the log-normal and linear-exponential distributions, respectively. This means that only ~1% of droplets are sampled. In reality, the amount is even lower than this, due to the low number density of ions in the source.

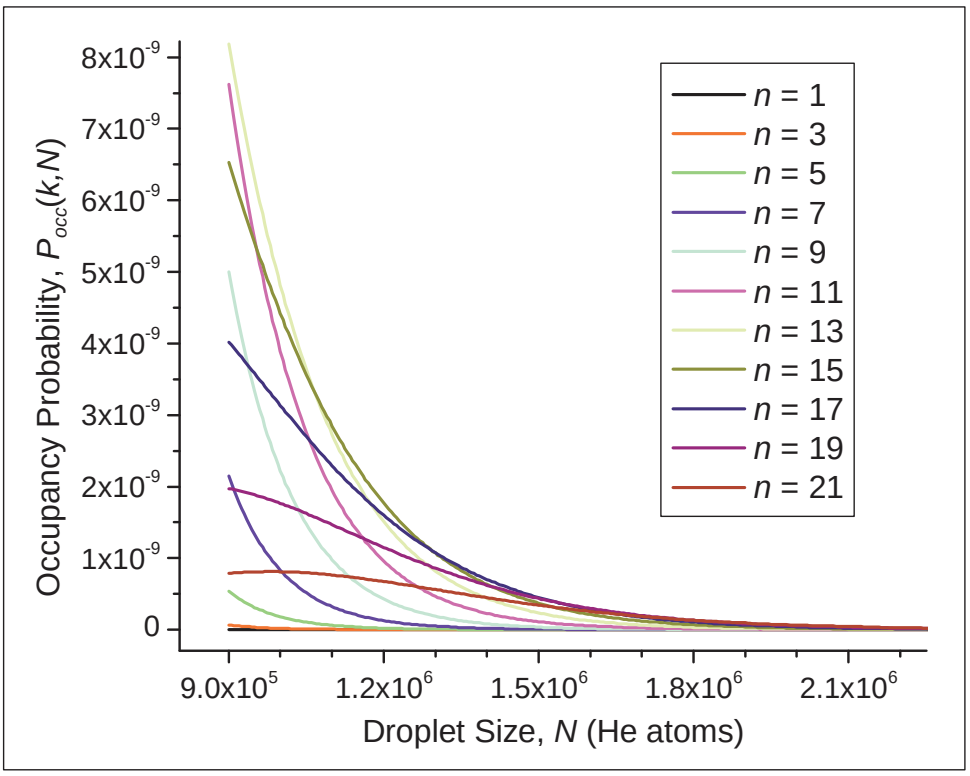

Figure B.3 Occupancy probability distributions as a function of droplet size.

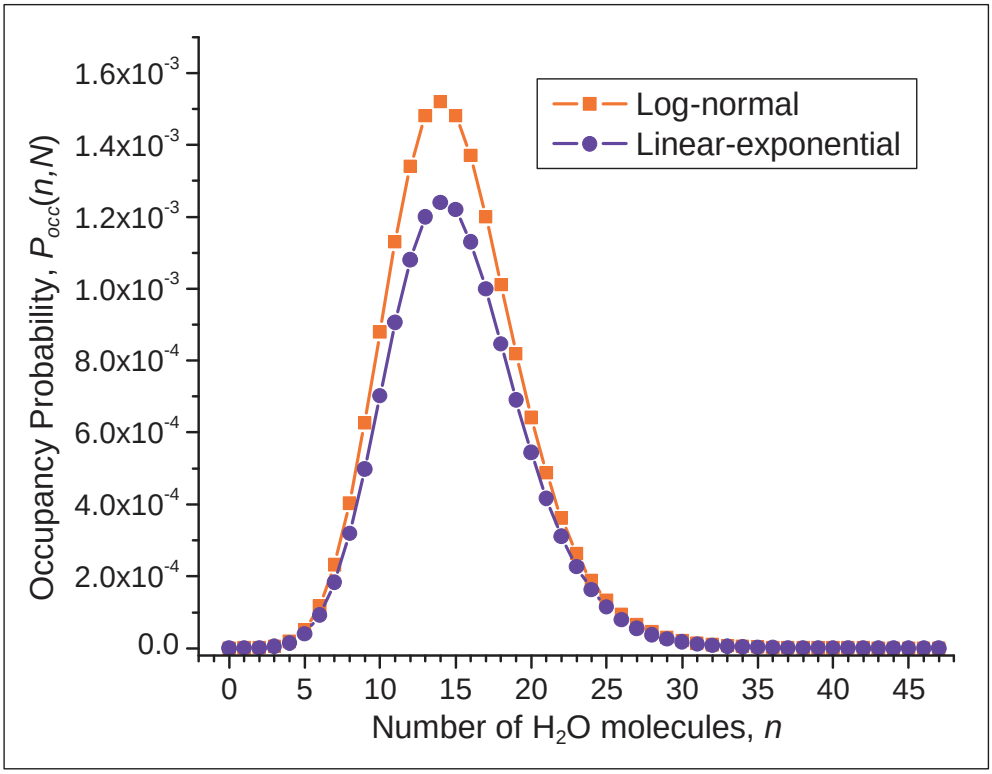

Figure B.4 Occupancy probability as a function of cluster size, *n*.

Appendix C

Determination of Ion-Doped Droplet Size

Chapter 5 describes the use of mass-dependent steering of ions for determination of the size distributions of ion-doped helium droplets. A qualitative picture of this phenomenon is shown in Figure C.1. A more quantitative view is shown in Figure 5.2. Shown in both of these figures are trajectories of ion-doped droplets predicted using SIMION. These calculated trajectories allow for the conversion of experimentally measured signal vs steering electrode potential curves into signal vs droplet size curves, which are droplet size distributions.

As described in Section 5.1.1, the signal of ion-doped droplets reaching an electron multiplier that was positioned either 5 or 10 mm off of the beam axis was recorded as a function of potential applied to the steering electrode. To model these experiments, the trajectories of droplets of varying size and +1 charge were simulated at varying droplet velocities (determined by T_0), collector electrode potentials, and steering electrode potentials. The result of one such simulation is shown in Figs. 5.2 and C.1. Alternatively, the droplet size can be plotted as a function of distance off-axis, as in Figure C.2. For all combinations of parameters, plots of droplet size vs distance off-axis can be fit by the equation $y = ax^{-1}$. Thus, Origin scripts were written to fit this equation to the simulated trajectories produced at all combinations of droplet velocity (or T_0), collector electrode potential, and steering electrode potential.

A different value was obtained for a from the fit to the simulated trajectories at each steering electrode potential. These values were tabulated for a given droplet

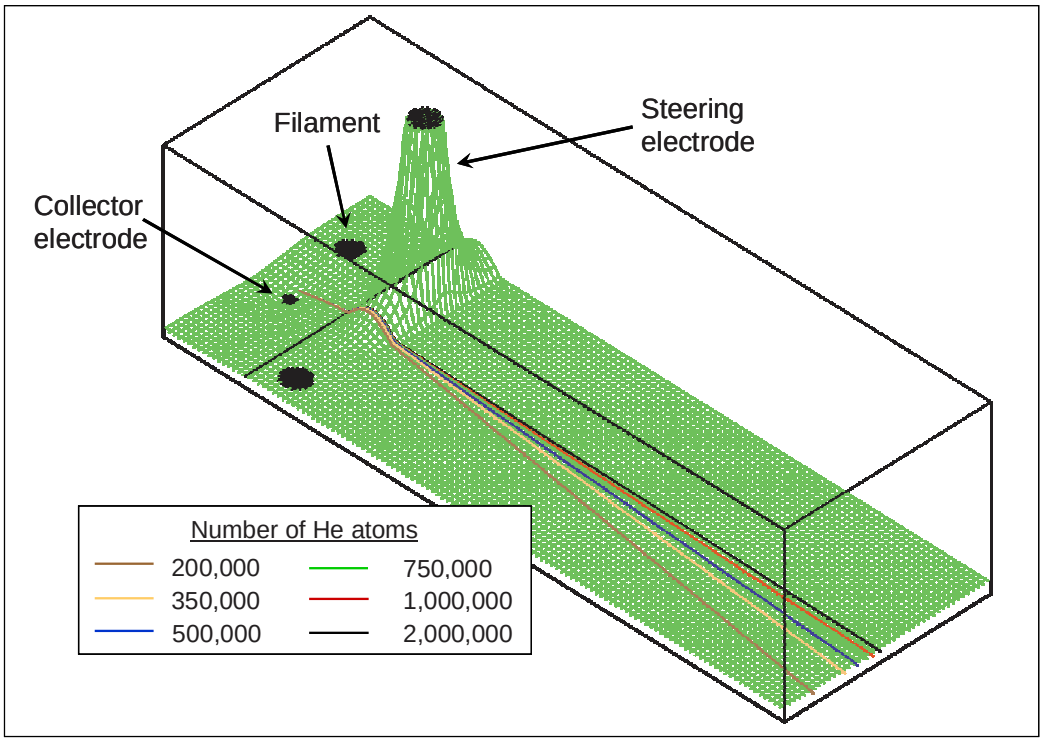

Figure C.1 SIMION model of ion-doped droplet steering.

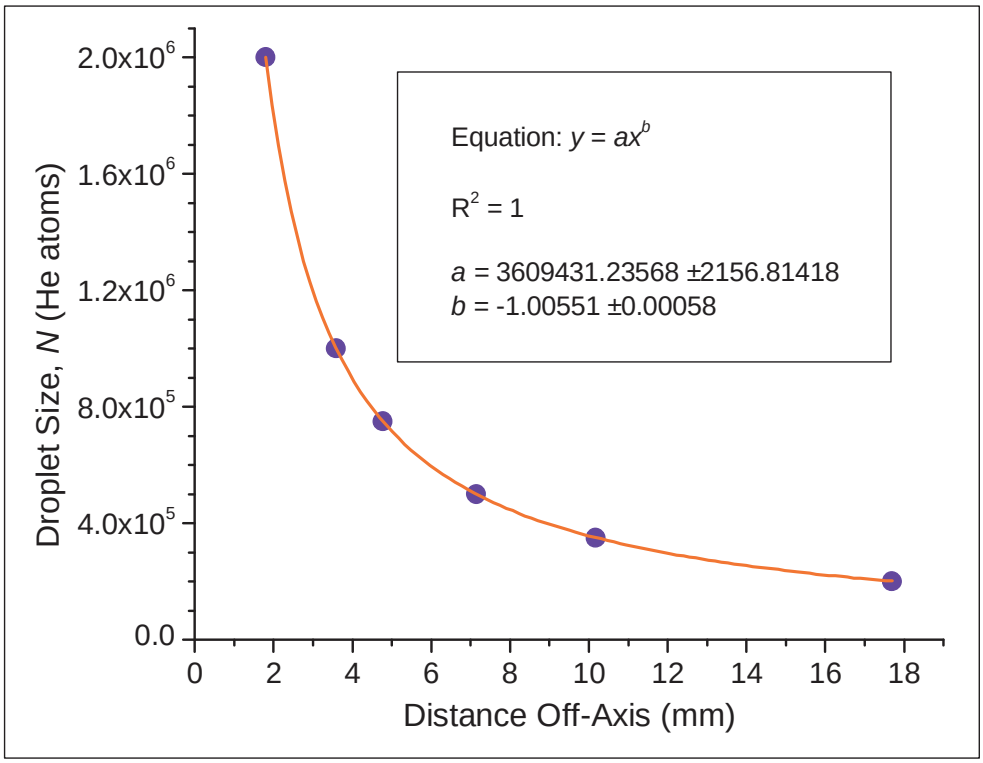

Figure C.2 Simulated trajectory data for droplet velocity corresponding to T_0 = 14.0 K, collector electrode = -20 V, and steering electrode = 2000 V.

velocity and collector electrode potential. The dependence of *a* on steering electrode potential is plotted in Figure C.3. Clearly, *a* exhibits a linear dependence on steering electrode potential, and interpolation at any potential within the range returns an accurate value for *a*.

The *y*-intercept, *B*, and slope, *A*, of the plot in Figure C.3 can be used in a simple equation to determine droplet size from steering electrode potential:

$$\text{Droplet Size} = \frac{A \times \text{Steering Electrode Potential} + B}{\text{Detector Distance Off - Axis}}. \qquad \text{(C.1)}$$

Unit analysis of the plots clarifies the above equation. The parameter *a* determined from Figure C.2 has units of He atoms × mm. Therefore, the *y*-intercept determined from Figure C.3 also has units of He atoms × mm. The slope determined from Figure C.3 then has units of (He atoms × mm)/V. Clearly, multiplying *A* by the potential, in volts, applied to the steering electrode results in units of He atoms × mm. Dividing the numerator of Equation C.1 by the distance, in mm, that the detector is positioned off-axis results in units of He atoms. In this fashion, measurement of ion-doped droplet signal as a function of steering electrode potential can be converted to signal vs droplet size.

The conversion from steering voltage to droplet size is relatively straightforward. However, the above description assumes that the detector entrance has an infinitesimal width. In reality, the slit width of the detector entrance is ~2 mm. The effect of this finite slit width is examined in Figure C.4. If the center of the detector entrance is positioned 5 mm off-axis, the entrance actually spans the region from 4 to 6 mm off-axis, as illustrated by the vertical dashed lines in Figure C.4. Extending these lines from the droplet size vs distance curve for the steering electrode potential of 1000 V to the *y*-axis

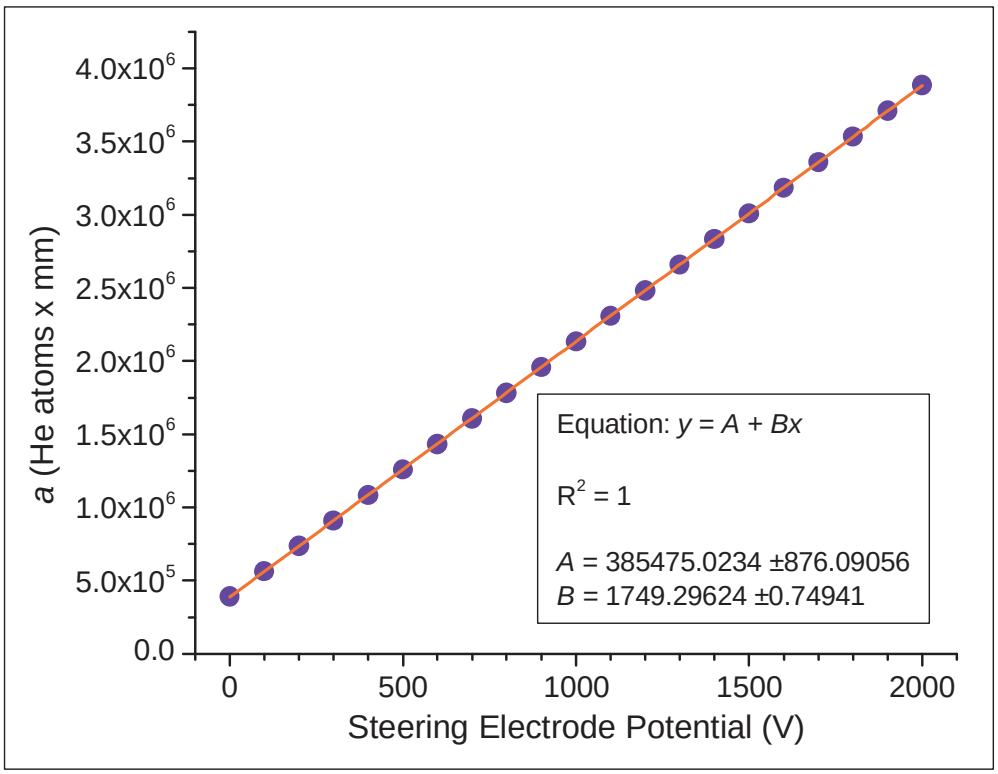

Figure C.3 Dependence of *a* values found in first step on steering electrode potential. Droplet velocity for T_0 = 14.0 K and collector electrode potential = -20 V.

yields the range of ion-doped droplet sizes reaching the detector at that steering electrode potential. As can be seen, at 1000 V, the detector entrance admits $N = 3.63 \times 10^5$ to $N = 5.45 \times 10^5$ when positioned 5 mm off-axis. With an infinitesimally wide detector entrance, only droplets of $N = 4.54 \times 10^5$ He atoms would be admitted. The range of droplet sizes admitted through the 2 mm wide entrance is ±21% of the value predicted for the infinitely narrow detector entrance. Looking at the droplet size vs distance curves for steering voltages of 200 V and 2000 V, it can be seen that larger ranges of droplet sizes pass through the detector entrance at higher steering voltages. As a percentage of the predicted droplet size, the range of droplet sizes reaching the detector at a given position off-axis remains constant over all steering electrode potentials.

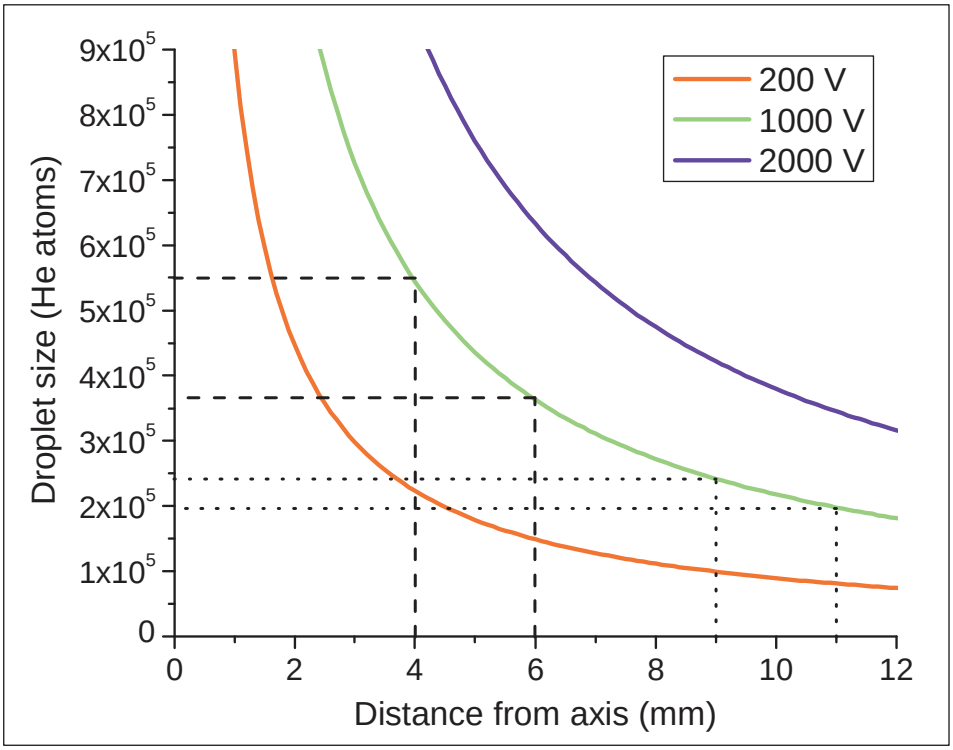

Figure C.4 Droplet size vs distance curves for various steering electrode potentials. T_0 = 14.0 K, collector electrode potential = -30 V.

Going through the same process as in the preceding paragraph, positioning the detector such that the entrance is centered 10 mm off-axis yields a different result. As can be seen by looking at the dotted lines in Figure C.4, when the detector is farther off-axis, a narrower range of droplet sizes is able to pass through the finite width of the detector entrance. When the steering electrode potential is 1000 V, the range of droplet sizes reaching the detector is $N = 1.98 \times 10^5 - 2.42 \times 10^5$ He atoms, which is ±10% of the predicted droplet size of 2.2×10^5 He atoms. The precision of droplet size measurement is not only independent of steering electrode potential, but it is also independent of nozzle temperature and collector electrode potential. Therefore, it can be ascertained that positioning the detector farther off-axis results in improved droplet size resolution at all

experimental conditions. However, as in analogous optical experiments, improved resolution comes at the cost of signal, so the distance of the detector from the beam axis is limited by the number of ion-doped droplets.

REFERENCES

1. Herbst, E. *Chem. Soc. Rev.* **2001**, *30*, 168-176.

2. De Petris, G. *Mass Spectrometry Reviews* **2003**, *22*, 251-271.

3. Headrick, J. M.; Diken, E. G.; Walters, R. S.; Hammer, N. I.; Christie, R. A.; Cui, J.; Myshakin, E. M.; Duncan, M. A.; Johnson, M. A.; and Jordan, K. D. *Science* **2005**, *308*, 1765-1769.

4. Roscioli, J. R.; McCunn, L. R.; and Johnson, M. A. *Science* **2007**, *316*, 249-254.

5. Lisy, J. M. *Int. Rev. Phys. Chem.* **1997**, *16*, 267-289.

6. Cabarcos, O. M.; Weinheimer, C. J.; and Lisy, J. M. *J. Chem. Phys.* **1998**, *108*, 5151-5154.

7. Cabarcos, O. M.; Weinheimer, C. J.; and Lisy, J. M. *J. Chem. Phys.* **1999**, *110*, 8429-8435.

8. Ma, J. C. and Dougherty, D. A. *Chemical Reviews* **1997**, *97*, 1303-1324.

9. Ruan, C. and Rodgers, M. T. *J. Am. Chem. Soc.* **2004**, *126*, 14600-14610.

10. Toney, M. D.; Hohenester, E.; Cowan, S. W.; and Jansonius, J. N. *Science* **1993**, *261*, 756-759.

11. Gallivan, J. P. and Dougherty, D. A. *Proceedings of the National Academy of Sciences of the United States of America* **1999**, *96*, 9459-9464.

12. Dzidic, I. and Kebarle, P. *J. Phys. Chem.* **1970**, *74*, 1466-1474.

13. Nielsen, S. B.; Masella, M.; and Kebarle, P. *J. Phys. Chem. A* **1999**, *103*, 9891-9898.

14. Armentrout, P. B. and Baer, T. *J. Phys. Chem.* **1996**, *100*, 12866-12877.

15. Oomens, J.; Sartakov, B. G.; Meijer, G.; and von Helden, G. *Int. J. Mass. Spec.* **2006**, *254*, 1-19.

16. Polfer, N. C.; Valle, J. J.; Moore, D. T.; Oomens, J.; Eyler, J. R.; and Bendiak, B. *Anal. Chem.* **2006**, *78*, 670-679.

17. Armentrout, P. B.; Rodgers, M. T.; Oomens, J.; and Steill, J. D. *J. Phys. Chem. A* **2008**, *112*, 2248-2257.

18. Dunbar, R. C.; Polfer, N. C.; and Oomens, J. *J. Am. Chem. Soc.* **2007**, *129*, 14562-14563.

19. Polfer, N. C.; Paizs, B.; Snoek, L. C.; Compagnon, I.; Suhai, S.; Meijer, G.; Von Helden, G.; and Oomens, J. *J. Am. Chem. Soc.* **2005**, *127*, 8571-8579.

20. FOM Institute for Plasma Physics Rijnhuizen. FELIX/Felice - FOM Institute for Plasma Physics Rijnhuizen. http://www.rijnh.nl/felix/ (accessed Mar 2008).

21. Watson, C. H.; Zimmerman, J. A.; Bruce, J. E.; and Eyler, J. R. *J. Phys. Chem.* **1991**, *95*, 6081-6086.

22. Wild, D. A.; Weiser, P. S.; and Bieske, E. J. *J. Chem. Phys.* **2001**, *115*, 6394-6400.

23. Vaden, T. D.; Weinheimer, C. J.; and Lisy, J. M. *J. Chem. Phys.* **2004**, *121*, 3102-3107.

24. Okumura, M.; Yeh, L. I.; Myers, J. D.; and Lee, Y. T. *J. Chem. Phys.* **1986**, *85*, 2328-2329.

25. Nielsen, S. B.; Ayotte, P.; Kelley, J. A.; Weddle, G. H.; and Johnson, M. A. *J. Chem. Phys.* **1999**, *111*, 10464-10468.

26. Weber, J. M.; Kelley, J. A.; Nielsen, S. B.; Ayotte, P.; and Johnson, M. A. *Science* **2000**, *287*, 2461-2463.

27. Vaden, T. D.; Lisy, J. M.; Carnegie, P. D.; Pillai, E. D.; and Duncan, M. A. *Phys. Chem. Chem. Phys.* **2006**, *8*, 3078-3082.

28. Douberly, G. E.; Ricks, A. M.; Schleyer, P.; and Duncan, M. A. *J. Chem. Phys.* **2008**, *128*, 021102/1-021102/4.

29. Choi, M. Y.; Douberly, G. E.; Falconer, T. M.; Lewis, W. K.; Lindsay, C. M.; Merritt, J. M.; Stiles, P. L.; and Miller, R. E. *Int. Rev. Phys. Chem.* **2006**, *25*, 15-75.

30. Toennies, J. P. and Vilesov, A. F. *Angew. Chem., Int. Ed. Engl.* **2004**, *43*, 2622-2648.

31. Stienkemeier, F. and Lehmann, K. K. *J. Phys. B: At. Mol. Opt. Phys.* **2006**, *39*, R127-R166.

32. Goyal, S.; Schutt, D. L.; and Scoles, G. *Phys. Rev. Lett.* **1992**, *69*, 933-936.

33. Goyal, S.; Robinson, G. N.; Schutt, D. L.; and Scoles, G. *J. Phys. Chem.* **1991**, *95*, 4186-4189.

34. Goyal, S.; Schutt, D. L.; and Scoles, G. *Acc. Chem. Res.* **1993**, *26*, 123-130.

35. Physical Transformations of Pure Substances. In *Physical Chemistry*, 6th ed.; Atkins, Peter W., Ed.; W. H. Freeman and Company: New York, 2000; 141-162.

36. McGervey, J. D. *Quantum Mechanics: Concepts and Applications*, Academic Press, Inc.: San Diego, 1995.

37. Brink, D. M. and Stringari, S. *Z. Phys. D* **1990**, *15*, 257-263.

38. Hartmann, M.; Miller, R. E.; Toennies, J. P.; and Vilesov, A. F. *Phys. Rev. Lett.* **1995**, *75*, 1566-1569.

39. Hartmann, M.; Miller, R. E.; Toennies, J. P.; and Vilesov, A. F. *Science* **1996**, *272*, 1631-1634.

40. Kwon, Y. and Whaley, K. B. *Phys. Rev. Lett.* **2003**, *89*, 273401/1-273401/4.

41. Cowley, R. A. and Woods, A. D. B. *Can. J. Phys.* **1971**, *49*, 177-200.

42. Dalfovo, F. and Stringari, S. *J. Chem. Phys.* **2001**, *115*, 1078-10089.

43. Lehmann, K. K. *Mol. Phys.* **1999**, *97*, 645-666.

44. Nauta, K. and Miller, R. E. *Science* **2000**, *287*, 293-295.

45. Callicoatt, B. E.; Mar, D. D.; Apkarian, V. A.; and Janda, K. C. *J. Chem. Phys.* **1996**, *105*, 7872-7875.

46. Halberstadt, N. and Janda, K. C. *Chem. Phys. Lett.* **1998**, *282*, 409-412.

47. Callicoatt, B. E.; Forde, K.; Jung, L. F.; Ruchti, T.; and Janda, K. C. *J. Chem. Phys.* **1998**, *109*, 10195-10200.

48. Farnik, M.; Henne, U.; Samelin, B.; and Toennies, J. P. *Z. Phys. D* **1997**, *40*, 93-98.

49. Scheidemann, A.; Schilling, B.; and Toennies, J. P. *J. Phys. Chem.* **1993**, *97*, 2128-2138.

50. Atomic, Molecular, and Optical Physics. In *CRC Handbook of Chemistry and Physics*, 77th ed.; Lide, D. R. and Frederikse, H. P. R., Eds.; CRC Press: New York, 1996; 214.

51. Doppner, T.; Diederich, T.; Tiggesbaumker, J.; and Meiwes-Broer, K. H. *Eur. Phys. J. D.* **2001**, *16*, 13-16.

52. Ruchti, T.; Forde, K.; Callicoatt, B. E.; Ludwigs, H.; and Janda, K. C. *J. Chem. Phys.* **1998**, *109*, 10679-10687.

53. Ruchti, T.; Callicoatt, B. E.; and Janda, K. C. *Phys. Chem. Chem. Phys.* **2000**, *2*, 4075-4080.

54. Vekey, K. *J. Mass. Spectrom.* **1996**, *31*, 445-463.

55. Frochtenicht, R.; Henne, U.; Toennies, J. P.; Ding, A.; Fieber-Erdmann, M.; and Drewello, T. *J. Chem. Phys.* **1995**, *104*, 2548-2556.

56. Lewis, W. K.; Applegate, B. E.; Sztáray, J.; Sztáray, B.; Baer, T.; Bemish, R. J.; and Miller, R. E. *J. Am. Chem. Soc.* **2004**, *126*, 11283-11292.

57. Lewis, W. K.; Bemish, R. J.; and Miller, R. E. *J. Chem. Phys.* **2005**, *123*, 141103/1-141103/4.

58. Bonhommeau, D.; Lewerenz, M.; and Halberstadt, N. *J. Chem. Phys.* **2008**, *128*, 054302/1-054302/17.

59. Claas, P.; Mende, S. O.; and Stienkemeier, F. *Rev. Sci. Instrum.* **2003**, *74*, 4071-4076.

60. Dahm, A. J. and Sanders, T. M., Jr. *Physical Review Letters* **1966**, *17*, 126-130.

61. Johnson, W. W. and Glaberson, W. I. *Phys. Rev. Lett.* **1972**, *29*, 214-217.

62. Atkins, K. R. *Physical Review* **1959**, *116*, 1339-1343.

63. Cole, M. W. and Bachman, R. A. *Phys. Rev. B* **1977**, *15*, 1388-1394.

64. Nakayama, A. and Yamashita, K. *J. Chem. Phys.* **2000**, *112*, 10966-10975.

65. Galli, D. E.; Buzzacchi, M.; and Reatto, L. *J. Chem. Phys.* **2001**, *115*, 10239-10247.

66. Buzzacchi, M.; Galli, D. E.; and Reatto, L. *Physical Review B: Condensed Matter and Materials Physics* **2001**, *64*, 094512/1-094512/10.

67. Coccia, E.; Bodo, E.; Marinetti, F.; Gianturco, F. A.; Yildrim, E.; Yurtsever, M.; and Yurtsever, E. *J. Chem. Phys.* **2007**, *126*, 124319.

68. Becker, E. W.; Klingelhofer, R.; and Lohse, P. *Z. Naturforsch. A* **1961**, *16A*, 1259.

69. Buchenau, H.; Knuth, E. L.; Northby, J. A.; Toennies, J. P.; and Winkler, C. *J. Chem. Phys.* **1990**, *92*, 6875-6889.

70. Knuth, E. L.; Schilling, B.; and Toennies, J. P. On Scaling Parameters for Predicting Cluster Sizes in Free Jets. Proceedings of the 19th International Symposium on Rarefied Gas Dynamics, Oxford, 1994; Oxford University Press: Oxford, UK, 1995; 270-276.

71. Knuth, E. L. and Henne, U. *J. Chem. Phys.* **1999**, *110*, 2664-2668.

72. Toennies, J. P.; Harms, J.; and Knuth, E. L. *J. Chem. Phys.* **1997**, *106*, 3348-3357.

73. Lewerenz, M.; Schilling, B.; and Toennies, J. P. *Chem. Phys. Lett.* **1993**, *206*, 381-387.

74. Harms, J.; Toennies, J. P.; and Dalfovo, F. *Phys. Rev. B* **1998**, *58*, 3341-3350.

75. Jiang, T. and Northby, J. A. *Phys. Rev. Lett.* **1992**, *68*, 2620-2623.

76. Lewerenz, M.; Schilling, B.; and Toennies, J. P. *J. Chem. Phys.* **1995**, *102*, 8191-8207.

77. Douberly, G. E. Infrared Laser Spectroscopy of Dopants In and On Helium Nanodroplets: Rotational and Vibrational Dynamics. Ph. D. Dissertation, University of North Carolina at Chapel Hill, Chapel Hill, NC, 2006.

78. Dresser, M. J. *J. Appl. Phys.* **1968**, *39*, 338-339.

79. Draves, J. A.; Luthey-Schulten, Z.; Liu, W.-L.; and Lisy, J. M. *J. Chem. Phys.* **1990**, *93*, 4589-4602.

80. Dahl, D. A. *SIMION 3D*, Idaho National Engineering and Environmental Laboratory: Idaho Falls, ID, 2000.

81. Buchenau, H.; Toennies, J. P.; and Northby, J. A. *J. Chem. Phys.* **1991**, *95*, 8134-8148.

82. Lewis, W. K. and Lindsay, C. M. University of North Carolina, Chapel Hill, NC. Unpublished work, 2004.

83. Frisch, M. J.; Trucks, G. W.; Schlegel, H. B.; Scuseria, G. E.; Robb, M. A.; Cheeseman, J. R.; Montgomery, J. J. A.; Vreven, T.; Kudin, K. N.; Burant, J. C.; Millam, J. M.; Iyengar, S. S.; Tomasi, J.; Barone, V.; Mennucci, B.; Cossi, M.; Scalmani, G.; Rega, N.; Petersson, G. A.; Nakatsuji, H.; Hada, M.; Ehara, M.; Toyota, K.; Fukuda, R.; Hasegawa, J.; Ishida, M.; Nakajima, T.; Honda, Y.; Kitao, O.; Nakai, H.; Klene, M.; Li, X.; Knox, J. E.; Hratchian, H. P.; Cross, J. B.; Adamo, C.; Jaramillo, J.; Gomperts, R.; Stratmann, R. E.; Yazyev, O.; Austin, A. J.; Cammi, R.; Pomelli, C.; Ochterski, J. W.; Ayala, P. Y.; Morokuma, K.; Voth, G. A.; Salvador, P.; Dannenberg, J. J.; Zakrzewski, V. G.; Dapprich, S.; Daniels, A. D.; Strain, M. C.; Farkas, O.; Malick, D. K.; Rabuck, A. D.; Raghavachari, K.; Foresman, J. B.; Ortiz, J. V.; Cui, Q.; Baboul, A. G.; Clifford, S.; Cioslowski, J.; Stefanov, B. B.; Liu, G.; Liashenko, A.; Piskorz, P.; Komaromi, I.; Martin, R. L.; Fox, D. J.; Keith, T.; Al-Laham, M. A.; Peng, C. Y.; Nanayakkara, A.; Challacombe, M.; Gill, P. M. W.; Johnson, B.; Chen, W.; Wong, M. W.; Gonzalez, C.; and and Pople, J. A. *Gaussian 03*, Gaussian, Inc., Pittsburgh PA: 2003.

84. National Institute of Standards and Technology CCCBDB Computational Chemistry Comparison and Benchmark Database. http://srdata.nist.gov/cccbdb/ (accessed Feb 2008).

85. Castleman, A. W.; Peterson, K. I.; Upschulte, B. L.; and Schelling, F. J. *Int. J. Mass. Spectrom. Ion. Proc.* **1983**, *47*, 203-206.

86. Tulegenov, A. S.; Wheatley, R. J.; Hodges, M. P.; and Harvey, A. H. *J. Chem. Phys.* **2007**, *126*, 094305/1-094305/11.

87. Fujii, T.; Ogura, M.; and Jimba, H. *Anal. Chem.* **1989**, *61*, 1026-1029.

88. Melissas, V. S.; Truhlar, D. G.; and Garrett, B. C. *J. Chem. Phys.* **1992**, *96*, 5758-5772.

89. Kita, S.; Gotoh, S.; Hasegawa, T.; and Shimakura, N. *J. Chem. Phys.* **1998**, *109*, 9713-9718.

90. Lehmann, K. K. and Northby, J. A. *Mol. Phys.* **1999**, *97*, 639-644.

91. Landau, L. D. *J. Phys. Moscow* **1941**, *5*, 71-90.

92. Landau, L. D. *J. Phys. Moscow* **1947**, *11*, 91-92.

93. Takayanagi, T. and Shiga, M. *Chem. Phys. Lett.* **2003**, *372*, 90-96.

94. Braun, A. and Drabbels, M. *Physical Review Letters* **2004**, *93*, 253401.

95. Braun, A. and Drabbels, M. *J. Chem. Phys.* **2007**, *127*, 114303/1-114303/14.

96. Braun, A. and Drabbels, M. *J. Chem. Phys.* **2007**, *127*, 114304/1-114304/9.

97. Buchachenko, A. A.; Tscherbul, T. V.; Klos, J.; Szczesniak, M. M.; Chalasinski, G.; Webb, R.; and Viehland, L. A. *J. Chem. Phys.* **2005**, *122*, 194311/1-194311/9.

98. Andersen, S. A.; Jensen, V. O.; and Michelsen, P. *Rev. Sci. Instrum.* **1972**, *43*, 945-947.

99. Bowley, R. M.; McClintock, P. V. E.; Moss, F. E.; Nancolas, G. G.; and Stamp, P. C. E. *Philosophical Transactions of the Royal Society of London, Series A: Mathematical, Physical and Engineering Sciences* **1982**, *307*, 201-260.

100. Ridgeway, M. E.; Falconer, T. M.; Bemish, R. J.; and Glish, G. L. Ion Source For Doping of Superfluid Helium Nanodroplets With a High Flux of Low Kinetic Energy Alkali Cations. Presented at the 55th ASMS Conference on Mass Spectrometry and Allied Topics, Indianapolis, IN, 2007.

101. Rynn, N. and D'Angelo, N. *Rev. Sci. Instrum.* **1960**, *31*, 1326-1333.

102. Paris, P. J. and Rynn, N. *Rev. Sci. Instrum.* **1990**, *61*, 1095-1100.

103. Kaneko, T.; Ishida, H.; Hatakeyama, R.; and Sato, N. *Rev. Sci. Instrum.* **2001**, *72*, 3854-3858.

104. Veeco Instruments. Veeco - Vapor Pressure Data for Selected Elements. http://www.veeco.com/library/Learning_Center/Growth_Information/Vapor_Pressure_Data_For_Selected_Elements/index.aspx (accessed Jun 2008).

105. Silverstein, R. M. and Webster, F. X. Mass Spectrometry. In *Spectrometric Identification of Organic Compounds*, 6th Ed.; John Wiley & Sons, Inc.: New York, 1997; 2-70.